

Proposal of intravascular  
oxygen saturation estimation method  
for microcirculation  
using sidestream dark-field imaging

January 2017

Tomohiro Kurata

Graduate School of Engineering  
CHIBA UNIVERSITY

(千葉大学審査学位論文)

Proposal of intravascular  
oxygen saturation estimation method  
for microcirculation  
using sidestream dark-field imaging

January 2017

Tomohiro Kurata

Graduate School of Engineering  
CHIBA UNIVERSITY

# Contents

<b>Chapter 1 INTRODUCTION</b>	<b>1</b>
1.1 Backgrounds . . . . .	1
1.1.1 Microcirculation . . . . .	1
1.1.2 Microcirculation imaging . . . . .	1
1.1.3 Usefulness of microcirculation assessments . . . . .	4
1.1.4 Spectral image-based oxygen saturation estimation . . . . .	6
1.2 Objectives of the study . . . . .	7
1.2.1 Proposal of SDF oximetry method . . . . .	7
1.2.2 SO <sub>2</sub> map and visualization of SO <sub>2</sub> transportation . . . . .	8
1.3 Structure of this thesis . . . . .	8
<b>Chapter 2 SIDESTREAM DARK-FIELD (SDF) IMAGING</b>	<b>10</b>
2.1 Principle of SDF imaging . . . . .	10
2.2 Development of SDF probe . . . . .	11
2.2.1 The first generation of our SDF probe . . . . .	11
2.2.2 The second generation . . . . .	14
2.3 Gamma correction . . . . .	17
<b>Chapter 3 SDF OXIMETRY</b>	<b>23</b>
3.1 Model of light behavior near organ's tissue surface . . . . .	23
3.2 Lambert-Beer law for biological tissues . . . . .	25
3.3 SDF oximetry . . . . .	27
3.4 Average extinction coefficient . . . . .	29
3.5 Error sensitivity of SO <sub>2</sub> estimation method . . . . .	32
3.6 Tissue scattering correction method using maximum slopes of SDF image . . .	33

<b>Chapter 4</b>	<b>PHOTON PROPAGATION SIMULATION</b>	<b>37</b>
4.1	Monte Carlo photon propagation simulation . . . . .	37
4.1.1	Algorithm . . . . .	38
4.1.2	Simulating LED light sources . . . . .	42
4.1.3	Test of the simulation . . . . .	44
4.2	Evaluation of the feasibility of SDF oximetry . . . . .	46
4.2.1	Digital tissue model . . . . .	47
4.2.2	Trial SDF device . . . . .	48
4.2.3	Results . . . . .	50
4.3	Evaluation of the scattering by tissue and a scattering correction method . . .	62
4.3.1	Digital phantom model . . . . .	64
4.3.2	Influence of the scattering on AECs . . . . .	65
4.3.3	Correction method for the tissue scattering . . . . .	68
<b>Chapter 5</b>	<b>BIOLOGICAL PHANTOM EXPERIMENTS</b>	<b>76</b>
5.1	Biological tissue-like phantoms . . . . .	76
5.2	Image analysis . . . . .	78
5.3	Results . . . . .	79
5.3.1	Calculation of AECs . . . . .	79
5.3.2	Scattering correction term of AECs and maximum slope of intensity profile . . . . .	80
5.3.3	SO <sub>2</sub> estimation . . . . .	81
<b>Chapter 6</b>	<b><i>IN VIVO</i> ANIMALS EXPERIMENTS</b>	<b>87</b>
6.1	Setups of experiments . . . . .	87
6.2	Image analysis . . . . .	89
6.2.1	Normalization of an SDF image . . . . .	89
6.2.2	Blood vessel extraction . . . . .	89
6.2.3	Optical density map and SO <sub>2</sub> map . . . . .	92
6.3	Results . . . . .	93
6.3.1	Blood vessel extraction from band images . . . . .	93
6.3.2	Optical density distribution map . . . . .	94



6.3.3	SO <sub>2</sub> map . . . . .	100
6.3.4	Analysis of oxygen saturation transportation . . . . .	103
<b>Chapter 7</b>	<b>CONCLUSIONS</b>	<b>109</b>
7.1	Proposal of SDF oximetry method . . . . .	109
7.2	Photon propagation simulation . . . . .	110
7.3	Biological tissue phantom experiments . . . . .	111
7.4	Animal experiments . . . . .	111
7.5	Future issues . . . . .	112
<b>Appendix</b>		<b>115</b>
A	Influence of other components of blood on SDF oximetry . . . . .	115
B	Absorption coefficients of blood with SO <sub>2</sub> = 0.0 ~ 1.0 . . . . .	116
<b>Reference</b>		<b>118</b>
<b>Acknowledgements</b>		<b>125</b>
<b>Publication List</b>		<b>126</b>

# List of Figures

1.1	A schematic illustration of microcirculation. Microcirculation is depicted by a region of a red rectangle. . . . .	2
1.2	OPS imaging reported by Groner <i>et al.</i> [9]. (a) The hand-held probe of OPS imaging. This probe was hand-held. (b) The optics of OPS imaging. . . . .	3
1.3	Spectral distribution of molar extinction coefficients $\varepsilon$ of oxygenated hemoglobin (HbO <sub>2</sub> ) and de-oxygenated hemoglobin (Hb) [10]. HbO <sub>2</sub> and Hb are depicted by a red and blue line, respectively. . . . .	4
2.1	A schematic illustration of the SDF imaging. Light illuminated from sources around the exterior of the probe tip is scattered within a tissue and absorbed by hemoglobin, re-emitted from the tissue surface and then acquired by the image sensor (camera). . . . .	11
2.2	The system of our trial SDF imaging. (a) Main components of the system. (b) A photograph of the system of the first generation probe. . . . .	12
2.3	The trial SDF illumination probe. (a) A schematic diagram of the SDF probe. The outer diameter of this device was 13.5 mm. LED chips were used as illumination. (b) This LED chip could be switched from blue light at the peak wavelength of 470 nm to green light at 527 nm. . . . .	13
2.4	Spectral distribution of molar extinction coefficients $\varepsilon$ of oxygenated hemoglobin (HbO <sub>2</sub> ) and de-oxygenated hemoglobin (Hb) (left axis) [10] and spectral intensity distribution of the three-color LEDs (SMLV56RGB1W) with the relative intensity (right axis). . . . .	14

2.5	The second generation of our trial SDF imaging probe and the system. (a) The system. (b) A photograph of the system. (c) Schematic for the tip of the trial SDF probe. (d) Photographs of the tip with three-color LEDs. The colors are blue with 470 nm peak wavelength, green with 527 nm, and red with 624 nm.	15
2.6	Characteristics of the imaging camera. (a) Spectral distribution of molar extinction coefficients $\varepsilon$ of oxygenated hemoglobin (HbO <sub>2</sub> ) and de-oxygenated hemoglobin (Hb) (left axis) [10] and spectral intensity distribution of the three-color LEDs (SMLVN6RGB1W) with the relative intensity (right axis). (b) The spectral response with reference to data sheet described by the manufacturer [61].	16
2.7	Environment of determining parameters for the gamma correction. (a) A grayscale pattern slide. (b) Environment of determining parameters. . . . .	18
2.8	Images of grayscale pattern slide. Images of no-slide, dark-current (the top rows) and several patterns of the moved slide (two rows of the bottom). . . . .	19
2.9	The location of seven ROIs in the image. . . . .	20
2.10	The relationship between the normalized pixel value and the transmittance of the grayscale pattern slide under illumination of (a) blue, (b) green, and (c) red. The relationship of each ROI and the average of that are depicted by blue solid and red dashed lines, respectively. . . . .	21
3.1	Results of the observation of a pig small intestine using the OCT equipment (a) <i>in vitro</i> and (b) <i>in vivo</i> . These images are the cross section along the red arrow of the inset color photograph on the right. There are blood vessel near the surface. . . . .	24
3.2	Results of the observation of the HE stained specimen. (a) The microscopic image of the HE stained specimen. The inset on the right is an enlarged image that shows blood vessels in the serosa. (b) The layer structure of a small intestine.	25
3.3	Light paths for retinal and SDF imaging. (a) For a retinal fundus camera. Three paths can be considered: incident light is backscattered from a blood vessel (backscattering); reflected or scattered light passes once through a vessel (single pass); the light passes twice through a vessel (double pass). (b) For a SDF imaging system. In contrast with a fundus camera, there is no backscattered light. The dashed line triangles denote the illumination area. . . . .	28

3.4	Schematic illustration of the proposed SDF oximetry method. (a) Incidence of light onto a tissue in the SDF geometry. (b) Back reflection light ( $I_{\text{in}}(\lambda)$ ) that is reflected within the tissue and re-emitted without going through the blood vessel and the transmitted light ( $I_{\text{out}}(\lambda)$ ) through the blood vessel. These light intensities are measured as pixel values: $p_{\text{in}}$ and $p_{\text{out}}$ . (c) Two causes of blur in the SDF image. . . . .	29
3.5	SO <sub>2</sub> estimation error for $\Delta T_1$ and $\Delta T_2$ using (a and b) extinction coefficients at the peak wavelengths with (a) $s = 0\%$ and (b) $s = 100\%$ and (c and d) AECs of each region of 470 nm and 527 nm with (c) $s = 0\%$ and (d) $s = 100\%$ . . . .	34
4.1	Schematic view of the photon propagation in a medium. . . . .	38
4.2	The scattering in the Monte Carlo simulation. (a) The scattering direction is determined with two angles, $\theta$ and $\phi$ . (b) The Henyey-Greenstein function with $g = 0.7, 0.8$ , and $0.9$ . This describes the probability for each scattering angle. The graph is normalized by the value for $g = 0.9$ and $\theta = 0$ . . . . .	40
4.3	Area illumination sources. These sources simulated by collecting point light sources. . . . .	43
4.4	The directivity of the LED chip (SMLVN6RGB1W, ROHM Co., Ltd., Kyoto, Japan) in the data sheet described by the manufacturer [69]. . . . .	43
4.5	The simple model. (a) Overview of the model. The red line represents the cross section. (b) The distribution of the fluence in the cross section represented in (a). . . . .	45
4.6	The top view of the distribution of the fluence. From the upper left hand side, the result shows the distribution of the fluence in a 0.0 mm, 1.0 mm, 2.5 mm, and 25 mm. . . . .	46
4.7	The distribution of the fluence in the cross section in the simple model with $\mu_s = 10 \text{ mm}^{-1}, 20 \text{ mm}^{-1}$ , and $30 \text{ mm}^{-1}$ . . . . .	47
4.8	The top view of the distribution of the fluence in the simple model with $\mu_s = 10 \text{ mm}^{-1}, 20 \text{ mm}^{-1}$ , and $30 \text{ mm}^{-1}$ . From the upper rows, the result shows the distribution of the fluence in a 0.0 mm and 2.5 mm from the left hand side. . .	48

4.9	The tissue model. (a) The cross section of a small intestine of a pig H&E stained. The layers, from the top surface, serosa, muscularis, submucosa, and mucosa. The inset on the right is an enlarged image that shows blood vessels are present in the serosa (blue arrows). (b) (c) The simulated tissue model which has a layered structure and a straight blood vessel at 0.1 mm below the top surface in the serosa. (b) Side view. (c) Overview. (d) A schematic diagram of the tissue model and the geometry of the simulation. . . . .	49
4.10	Optical properties used in this study. (a) Optical properties of blood [10, 73]. Open and closed squares represent the absorption coefficient of oxygenated and de-oxygenated hemoglobin respectively, crosses represent the scattering coefficient, and circles represents the anisotropy factor. (b) Optical properties of the tissue [74]. Squares represent the absorption coefficient and crosses represent the scattering coefficient. . . . .	50
4.11	Results of the photon propagation simulation for a tissue model with the straight vessel. (a) The virtual SDF image (the gray level map of the intensity). (b) The profile of the virtual SDF image (blue line). The single pass, the double pass, and the no pass are depicted by red, magenta, and green, respectively. (c) Absorption coefficients with average extinction coefficients are plotted as a function of bandwidth of the illumination. $\bar{\epsilon}(\lambda_0)$ for $\lambda_0 = 470$ nm and 527 nm are depicted by squares and triangles, respectively. Open and closed symbols represent $SO_2$ $s = 1$ and $s = 0$ , respectively. Diameter $d$ values of 100 $\mu\text{m}$ , 200 $\mu\text{m}$ , and 300 $\mu\text{m}$ are depicted by solid lines, dashed lines, and chain lines, respectively. (d) The histogram of the intensity $I_{\text{in}}$ of light directly entering into the blood vessel and $I_{\text{out}}$ of light passing through it when the model is (a). . . . .	52
4.12	Dispersion of estimated values due to the number of incident photons. (a) Estimated values. (b) Coefficients of variation. (c) Calculation time for performing an $SO_2$ estimation. . . . .	54
4.13	The $SO_2$ estimation of $d = 100$ $\mu\text{m}$ vessel. (a) The monochromatic light with no bandwidth ( $w = 0$ ). (b) $w = 10$ nm. (c) $w = 20$ nm. (d) $w = 30$ nm. (e) $w = 40$ nm. (f) $w = 50$ nm. . . . .	55

4.14	The SO <sub>2</sub> estimation of $d = 200 \mu\text{m}$ vessel. (a) The monochromatic light with no bandwidth ( $w = 0$ ). (b) $w = 10 \text{ nm}$ . (c) $w = 20 \text{ nm}$ . (d) $w = 30 \text{ nm}$ . (e) $w = 40 \text{ nm}$ . (f) $w = 50 \text{ nm}$ . . . . .	56
4.15	The SO <sub>2</sub> estimation of $d = 300 \mu\text{m}$ vessel. (a) The monochromatic light with no bandwidth ( $w = 0$ ). (b) $w = 10 \text{ nm}$ . (c) $w = 20 \text{ nm}$ . (d) $w = 30 \text{ nm}$ . (e) $w = 40 \text{ nm}$ . (f) $w = 50 \text{ nm}$ . . . . .	57
4.16	The mean of SEE $\overline{\Delta s}$ surface with the contour interval color. (a) PLB. (b) EPW. (c) AEC. . . . .	58
4.17	The SO <sub>2</sub> estimation error caused by $\Delta\Psi$ for use of (a) extinction coefficients at the peak wavelength and (b) AECs of a $100 \mu\text{m}$ diameter and a $30 \text{ nm}$ bandwidth. Symbols depict SO <sub>2</sub> estimation errors in the simulation. . . . .	60
4.18	The mean PE evaluated by Smith's procedure [42]. The surface is a fitting curve with a bivariate power series until the second-order of both variables. . .	62
4.19	The SO <sub>2</sub> estimation error for choosing wavelengths. (a) Error map. SO <sub>2</sub> estimation simulation using combination of (b) (474, 510) and (c) (474, 548). . . .	63
4.20	The digital phantom model. (a) Overview, and (b) overview from the top side.	64
4.21	Optical properties of fat emulsion with referring to [76]. . . . .	65
4.22	The virtual SDF images for the $470 \text{ nm}$ peak wavelength illumination. . . . .	66
4.23	Results of the simulation. (a) The AECs normalized by the theoretical values. (b) Results of $\xi$ in the simulation. . . . .	67
4.24	The average absolute maximum slope $ m $ calculated from (a) $470 \text{ nm}$ (b) $527 \text{ nm}$ images. . . . .	69
4.25	The relationships for the tissue-scattering correction method. The relationships between $\mu_s$ and $ m $ calculated from (a) blue- (b) green-band images. (c) The relationship between $ m $ and $\xi$ . . . . .	70
4.26	Results of the SO <sub>2</sub> estimation for the single-wavelength light sources. (a) Results using extinction coefficients at the peak-wavelength. (b) Results using the correction method. . . . .	71
4.27	The average absolute maximum slope $ m $ calculated from (a) blue- (b) green-band images. . . . .	72

4.28	The relationship between $\mu_s$ and $ m $ calculated from (a) blue- (b) green-band images. . . . .	72
4.29	SO <sub>2</sub> estimation results using six types of extinction coefficients for turbid phantoms of (a) 0.0% (b) 0.1% (c) 0.5% (d) 1.0% fat emulsion with the glass tube of 300 $\mu\text{m}$ diameter. (e) Estimation values using the suitable AECs extracted from the results of (a) to (d). . . . .	73
4.30	SO <sub>2</sub> estimation results using our scattering correction method. (a) Results of the estimation of the scattering coefficient from the average maximum absolute slope. (b) Results of SO <sub>2</sub> estimation using our correction method. (c) Comparison of (b) to results using the extinction coefficient at the peak wavelength and AECs without the scattering correction. . . . .	75
5.1	Tissue-like turbid phantom. (a) Schematic cross-sectional diagram of the phantom including glass tubes. (b) A photograph of four phantoms. From the right, the phantoms contain 0.0, 0.1, 0.5 or 1.0% fat emulsion. . . . .	77
5.2	The optical density measurement procedure from an SDF image. The profile $f(x)$ and the edge-connection line $c(x)$ are depicted by the black solid line and the red dashed line, respectively. The location of the minimum pixel value represents $x_{\min}$ . . . . .	79
5.3	The average absolute maximum slope $ m $ calculated from (a) blue- (b) green-band images. . . . .	81
5.4	Cropped SDF images of the turbid phantom with the glass tube of 300 $\mu\text{m}$ inner diameter for (a) SO <sub>2</sub> = 100% and (b) SO <sub>2</sub> = 0% blood-filled glass tube. These images are captured using blue (the second row), green (the third row), and red (the lower row) LED illumination sources and, from the left hand side, for the phantom containing with the only agar powder, and phantoms with 0.1, 0.5, or 1.0% fat emulsion. Color images of the top row are synthetic images using red, green, and blue illumination. . . . .	82

5.5	AECs of oxygenated and de-oxygenated hemoglobin obtained using the turbid phantoms. (a) and (b) The AEC versus the concentration of fat emulsion for bovine blood for LED sources of (a) 470 nm peak wavelength and (b) 527 nm peak wavelength. (c) The influence $\xi$ on the AECs due to the scattering by surrounding tissue for the experiments and the simulation. Solid lines represent the fitting results obtained with a linear function. (d) The relation between the maximum absolute slope and the scattering coefficient of the phantoms with a 300 $\mu\text{m}$ diameter glass tube. . . . .	83
5.6	SO <sub>2</sub> estimation results using six types of extinction coefficients for turbid phantoms of (a) 0.0% (b) 0.1% (c) 0.5% (d) 1.0% fat emulsion with the glass tube of 300 $\mu\text{m}$ diameter. (e) Estimation values using the suitable AECs extracted from the results of (a) to (d). . . . .	85
5.7	SO <sub>2</sub> estimation results using our scattering correction method. (a) Results of the estimation of the scattering coefficient from the average maximum absolute slope. (b) Results of SO <sub>2</sub> estimation using our correction method. (c) Comparison of (b) to results using the extinction coefficient at the peak wavelength and AECs without the scattering correction. . . . .	86
6.1	SDF images of pig's (a) stomach and (b) colon. . . . .	88
6.2	Environment of experiments <i>in vivo</i> . (a) A rats experiment. (b) A pigs experiment. . . . .	88
6.3	A flowchart of the image analysis for producing optical density map. . . . .	89
6.4	The outline of $\mathcal{V}(s)$ . . . . .	91
6.5	Results of the blood vessel extraction for a blue-band image. . . . .	95
6.6	Results of the blood vessel extraction for a green-band image. . . . .	96
6.7	The intensity image of the blue-band image. (a) The Original image. (b) A smoothed image obtained by filtering with the Gaussian filter. (c) The transmittance image with pseudo-color. . . . .	97
6.8	The intensity image of the green-band image. (a) The Original image. (b) A smoothed image obtained by filtering with the Gaussian filter. (c) The transmittance image with pseudo-color. . . . .	98



6.9	Incident light intensity maps and optical density maps obtained from the incident light intensity maps using the average pixel value of $\mathcal{B}$ as the incident light intensity. The incident light intensity map of (a) a blue-band and (b) green-band image. The optical density map of (c) a blue-band and (d) green-band image. . . . .	99
6.10	Incident light intensity maps and optical density maps obtained from the incident light intensity maps using the average pixel value of ROIs as the incident light intensity. The incident light intensity map of (a) a blue-band and (b) green-band image. The optical density map of (c) a blue-band and (d) green-band image. . . . .	101
6.11	The $\text{SO}_2$ -dependence of $\Psi$ . . . . .	102
6.12	The distribution of $\Psi$ from (a) Figs. 6.9(c) and 6.9(d) and (b) Figs. 6.10(c) and 6.10(d). . . . .	102
6.13	The $\text{SO}_2$ distribution map using $\Psi$ shown in Fig. 6.12(a). (a and b) Maps using the extinction coefficients of the peak-wavelengths. (c and d) Maps using AECs. (a and c) A range of $[0, 1]$ of $\text{SO}_2$ . (b and d) The relative $\text{SO}_2$ maps. .	104
6.14	The $\text{SO}_2$ distribution map using $\Psi$ shown in Fig. 6.12(b). (a and b) Maps using the extinction coefficients of the peak-wavelengths. (c and d) Maps using AECs. (a and c) A range of $[0, 1]$ of $\text{SO}_2$ . (b and d) The relative $\text{SO}_2$ maps. .	105
6.15	The variation of $\text{SO}_2$ along the blood vessel. (a) The positions to be measured $\text{SO}_2$ is depicted by a black dashed line. (b) The $\text{SO}_2$ along the blood vessel. Blue points represent the data and a red line represents the fitting result. . . .	106
6.16	The variation of $\text{SO}_2$ along a cross section of the blood vessel. (a) The positions to be measured $\text{SO}_2$ is depicted by a black solid line. (b) The $\text{SO}_2$ along the blood vessel. Blue points represent the data. . . . .	106
6.17	Oxygen transportation at a branch of the vessel. (a) Relative $\text{SO}_2$ map of the pig small intestine. (b and d) Locations of $\text{SO}_2$ estimation. (c and e) The variation of $\text{SO}_2$ along the black line shown in (b) and (d), respectively. . . .	108

# List of Tables

1.1	The indexes for evaluating microcirculation [19,20,24]. . . . .	5
2.1	Specification of our SDF probes. . . . .	17
2.2	Results of $\tilde{\alpha}$ and $\tilde{\gamma}$ using three-color LEDs. . . . .	22
2.3	Results of $\Delta\tilde{p}$ . . . . .	22
4.1	The distribution of the total incident photon. . . . .	44
4.2	Optical properties of the tissue model. . . . .	51
4.3	The mean SEE $\overline{\Delta s} \pm \text{SD}$ . . . . .	59
4.4	Optical properties ( $\mu_s$ and $g$ ) under the blue illumination. . . . .	66
4.5	Optical properties ( $\mu_s$ and $g$ ) under the green illumination. . . . .	67
4.6	The AAE [%] of estimated values. . . . .	69
4.7	The AAE [%] of estimated values. . . . .	74
5.1	The AAE [%] of estimated values. . . . .	84
B.1	Optical properties of blood with $\text{SO}_2$ with reference to [10,73]. The upper rows show the wavelength region of the blue illumination and the lower rows show one of the green illumination. . . . .	117

# Chapter 1 INTRODUCTION

In this chapter, backgrounds and objectives of the study are described. In § 1.1, as the backgrounds, first, microcirculation that is the subject of the study, microcirculation imaging techniques using a hand-held probe, and the usefulness of the observation of this subject are introduced. Next, previous studies of oxygen saturation estimation methods are explained. Finally, the objectives of the study are stated in § 1.2. Finally, the structure of this thesis is shown in § 1.3.

## 1.1 Backgrounds

### 1.1.1 Microcirculation

Microcirculation refers to the circulation in blood vessels as those of a less than 100  $\mu\text{m}$  inner diameter. Microcirculation can be found in organ tissues and exists throughout the body. Microcirculation consists of arterioles, capillaries, and venules as shown in Fig. 1.1. Its functions are to exchange nutrients and oxygen delivered by red blood cells (RBCs) for wastes (carbon dioxide, *etc.*) and ensures adequate immunological functioning. In other words, microcirculation occurs in the region where arteries turn into veins. Oxygen molecules are transported to tissues of organs throughout the body by binding to hemoglobin in RBCs.

### 1.1.2 Microcirculation imaging

Many studies have proposed to observe the microcirculation using various imaging apparatus [1]. Imaging techniques using visible or near infrared light are laser speckle contrast analysis (LSCA) [2, 3], optical coherence tomography (OCT) [4], and multimodal optical imaging [5]. In addition to the above, for photoacoustic tomography (PT) which is combined with light and

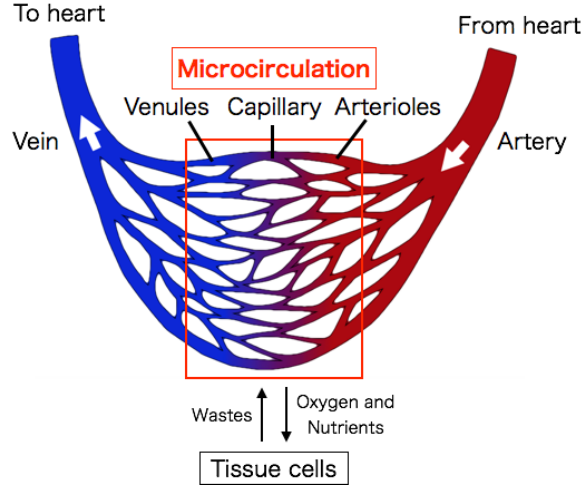


Fig 1.1: A schematic illustration of microcirculation. Microcirculation is depicted by a region of a red rectangle.

ultrasound has been used [6]. In other modalities, studies of ultrasound [7], micro computed tomography (CT) with a contrast agent [8], or magnetic resonance imaging (MRI) have been reported. The imaging techniques using visible light and a hand-held probe are introduced in this section. These techniques are more suitable for clinical applications because large-scale apparatus are not necessary for the imaging techniques.

### Orthogonal polarization spectral (OPS) imaging

To visualize microcirculation, orthogonal polarization spectral (OPS) imaging was reported by Groner *et al.* [9] as the first hand-held microcirculation imaging technique. Figure 1.2 shows the probe and optics as referred to Groner's study. This technique uses polarized light of a wavelength region of a 548 nm peak-wavelength as incident light and an imaging camera with an orthogonal polarizer to light polarization of the incident light. The imaging camera can obtain only depolarized light reflected from within the tissue. By using the wavelength region centered at 548 nm that is an isosbestic point as shown in Fig. 1.3, an OPS image with the same contrast of between arterioles (oxygenated) and venules (de-oxygenated hemoglobin) can be obtained. Image contamination by reflected light on the surface is avoided by using light polarization. Groner *et al.* reported that quality of OPS images was equivalent to one of fluorescence microscopic images for microcirculation. Therefore, the imaging of the

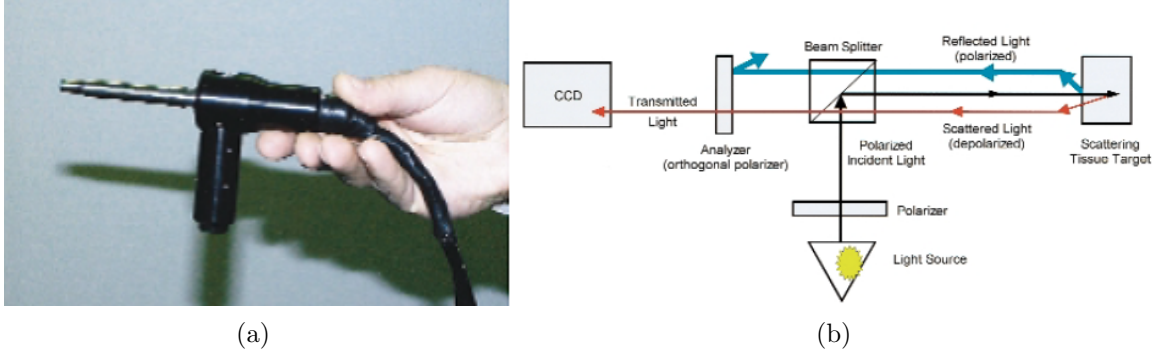


Fig 1.2: OPS imaging reported by Groner *et al.* [9]. (a) The hand-held probe of OPS imaging. This probe was hand-held. (b) The optics of OPS imaging.

microcirculation has been possible with a high-contrast and label-free image. Moreover, this study reported that since the relationship between optical response of a target and signals of an camera was linear, the OPS imaging had the possibility of measuring optical densities as reflection spectroscopy. The probe for medical use, named as Cytoscan video microscope, was invented and manufactured by Cytometrics [11].

### Sidestream dark-field (SDF) imaging

As an improved microcirculation imaging technique, sidestream dark-field (SDF) imaging was reported by Ince [12,13]. The SDF imaging technique is also a noninvasive optical imaging technique allowing direct visualization of microcirculation. This technique is based on dark-field imaging and contrivance of the optical path of the probe to prevent the surface reflection light of tissue from contaminating an image. Since OPS imaging has some restrictions that are sensitive to blurring caused by the movement of RBCs and the necessity of a high-power light source owing to some filters used, SDF imaging prevents the surface reflection light without polarizers and uses compact and low-power light sources such as light emitting diodes (LEDs). The SDF imaging is superior in that it provides sufficiently high image quality, better granularity of the observed RBCs, and less motion blurring of the probe by the use of stroboscopic LEDs in a ring-based SDF illumination [14, 15] as compared to the OPS imaging. The probe and a software for medical use, named as Microscan, was invented and manufactured by MicroVision Medical [16].

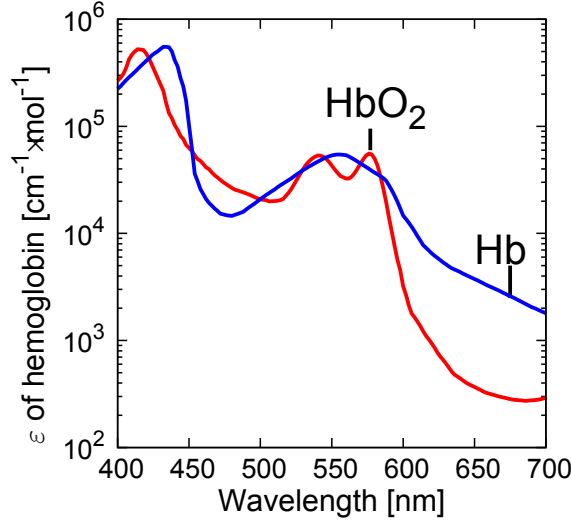


Fig 1.3: Spectral distribution of molar extinction coefficients  $\varepsilon$  of oxygenated hemoglobin ( $\text{HbO}_2$ ) and de-oxygenated hemoglobin (Hb) [10].  $\text{HbO}_2$  and Hb are depicted by a red and blue line, respectively.

### 1.1.3 Usefulness of microcirculation assessments

As clinical application of microcirculation imaging, the imaging has been applied to diagnose perfusion disturbances in an area of the peripheral vascular for sepsis or septic shock, and the state of specific organs which is normal or ischemia for transplants or ablative operations for non-occlusive mesenteric ischemia (NOMI) [17] or the Crohn's disease [18].

By using OPS or SDF imaging, diagnosis for perfusion disturbances in the peripheral vascular during the disease such as sepsis or septic shock have been reported in many studies [19–23]. Some indexes have been proposed for quantification in [19, 20, 24]: total vascular density (TVD), small vessel density (SVD), proportion of perfused vessels (PPV), perfused vessel density (PVD), microvascular flow index (MFI), and functional capillary density (FCD). The definition of these indexes are shown in Table 1.1. These indexes, however, depend on the target of organs or individual differences. As quantification of the microcirculation by the SDF imaging technique that overcomes these dependences, some physical quantities such as vessel length, vessel diameter, and velocity of red blood cells (RBCs) have been estimated by analyzing the SDF images of individual vessels [25].

In digestive surgery and emergency medicine, surgeons typically diagnose the state of an

Table 1.1: The indexes for evaluating microcirculation [19, 20, 24].

Index	Definition
TVD	The number of vessels crossing unit length of a line
SVD	TVD for small vessels ( $\leq 20 \mu\text{m}$ )
PPV	The proportion of perfused vessels
PVD	The product of TVD and PPV
	Semiquantitative score
MFI	(0=no flow, 1=sludging, 2=moderate flow, 3=normal flow)

organ that is normal or ischemia on the basis of its visual color in order to decide whether to remove a part of it. The diagnosis relies on the surgeons' visual impression and previous experiences. Therefore, a quantitative technique for evaluating the state of an organ is desirable. A macro technique with a hyperspectral camera has been suggested [26]. However, it is difficult for any macro techniques to specifically distinguish the boundary of the ischemia part. For a digestive organ, videoscope techniques such as laparoscopic and endoscopic surgery are commonly used recently. In this case, inaccurate color reproduction disturbs the diagnosis of surgeons. In contrast, a micro technique such as an observation of the microcirculation is more accurate to distinguish the boundary of the ischemia part, although it is a local observation. Therefore, the OPS or SDF imaging is useful to help in diagnosing the state of organs. Moreover, these imaging can be applied to videoscope surgery because these probe can be fabricated with a small diameter. However, for accurate diagnosis, monitoring not only the flow of RBCs but also some other physical quantities are required. In particular, the most important item among the physical quantities of blood to evaluate the level of the state of an organ is the amount of oxygen in the blood.

In addition to use for diagnosis of diseases, monitoring the oxygen level in microcirculation is useful in the study of the mechanism of the oxygen transportation in microcirculation. In recent years, elucidating the oxygen transportation in microcirculation has been carried out in many studies to understand not only the mechanism of the oxygen transportation in microcirculation but causes of diseases from physiology function [27, 28]. The oxygen transportation during wound healing has been reported in the cases of use of SDF imaging in oral cavity [29] and a dorsal skinfold window chamber and the fluorescence imaging [30].

As well as the elucidation of the oxygen transportation in microcirculation, visualization of the oxygen transportation in microcirculation can also be used to elucidate the mechanisms of both vascularization and oxygen metabolism in around newborn blood vessels associated with the development of cancer. The change of blood vessel network due to vascularization for mammary tumours was reported by Damiani *et al.* [31].

#### 1.1.4 Spectral image-based oxygen saturation estimation

Oxygen transportation to tissues is an important role for microcirculation and essential to maintain human or animals life. The index of oxygen included in blood is defined by the ratio of oxygen bound to hemoglobin. This quantity is called oxygen saturation ( $SO_2$ ) and defined by:

$$SO_2 := \frac{\text{Concentration of oxygenated hemoglobin}}{\text{Concentration of total hemoglobin}}, \quad (1.1)$$

oxygenated hemoglobin is one binding to oxygen. It is noted that well-known  $SaO_2$  and  $SpO_2$  are oxygen saturation of arterial blood measured by blood sampling and pulse oximetry, respectively. Though  $SaO_2$  and  $SpO_2$  are useful for monitoring vital signs, these values do not represent the local sign. Knowing oxygen saturation of each blood vessel is valuable for understand of the oxygen transportation and diagnose diseased parts locally such as in digestive surgery and emergency medicine as the aforementioned in §1.1.3.

Spectral image-based intravascular oxygen saturation estimation methods have been reported in spectromicroscopy and ophthalmology. These methods use the difference in the spectral absorption of between oxygenated and de-oxygenated hemoglobin as shown in Fig. 1.3.

Styp-Rekowska *et al.* reported an intravascular  $SO_2$  and hematocrit estimation method using intravital microscopy [33]. They used spectral images from 500 nm to 598 nm wavelengths. They also estimated  $SO_2$  and hematocrit of both rats and mice and produced the  $SO_2$  and hematocrit distribution maps.

In ophthalmology, the first  $SO_2$  estimation was attempted by Hickam *et al.* [34]. Cohen and Laing reported use of a fundus camera [35]. They used the multi-scattering theory established by Twersky [36–38] to correct the scattering by RBCs. Delori reported the results of  $SO_2$  estimation experiments using three-band images [39]. By using light of three wavelength regions,



they corrected the influence of other than the absorption by hemoglobin in the Lambert-Beer law. Beach *et al.* reported retinal oximetry using dual-wavelength digital images [40]. Hardarson *et al.* showed retinal intravascular  $\text{SO}_2$  distribution [41]. As a method of improving the accuracy of  $\text{SO}_2$  estimation, the selection of wavelengths of illumination sources has proposed by Smith [42].

In recent years, the  $\text{SO}_2$  visualization of capillaries has been reported for biological applications of photoacoustic imaging [43–45] and optical coherence tomography (OCT) with visible light sources [46]. Although these techniques are capable of high-resolution imaging, apparatus used in the imaging system are a higher cost.

## 1.2 Objectives of the study

Since the microcirculation imaging allows visualizing the flow of RBCs and the structure of the network of blood vessels, it can be applied to diagnose the state of body's organs. Among desirable biological quantities to be measured, this study has been focused on intravascular  $\text{SO}_2$  of individual blood vessels. The  $\text{SO}_2$  measurement or visualization of individual vessels would permit evaluation of oxygen transportation into organs.

### 1.2.1 Proposal of SDF oximetry method

The objective of this thesis is to establish an image-based estimation method of oxygen levels of the individual vessels from spectral images acquired by SDF imaging, which is called SDF oximetry [47]. We develop an  $\text{SO}_2$  estimation method that has the same or same degree of accuracy as methods using existing complicated measurement or observation techniques such as two-photon imaging with oxygen-sensitive fluorescent dye [48], photoacoustic imaging [43–45, 49] and visible-light optical OCT [46, 50, 51]. Since the system of the SDF imaging is simpler than existing complicated and large-scale imaging techniques, the SDF oximetry may be widely use for clinical applications. Our oximetry method is based on the Lambert-Beer law for band images. The method also assumes the use of an SDF probe with light emitting diodes (LEDs) as illumination sources and, therefore, uses average extinction coefficients (AECs) of hemoglobin. These coefficients are modified version of light absorption coefficients shown in

Fig. 1.3 which have been suggested to correct the influence of non-monochromatic light and imaging camera characteristics in a retinal oximetry study [35].

To realize the method, we developed a trial SDF probe and verified the feasibility in experiments of the numerical simulation and phantom experiments. As the first approach, we performed the Monte Carlo photon propagation simulation. In this approach, we evaluated the validity and accuracy of the method. Moreover, dependence of accuracy on vessel diameters and wavelength-bandwidths of the illumination sources was investigated [47]. As the second step, we performed phantom experiments using bovine blood with already-known  $\text{SO}_2$  [52]. Biological tissue-like phantoms were made using agar, blood-filled glass tubes, and fat emulsion. In this experiments, the validity of the method using the trial probe and influences on accuracy of the scattering by peripheral tissues around a target blood vessel were investigated. Furthermore, the correction method of the tissue scattering was proposed. The correction method is based on the use of feature values that indicate the scattering by tissue around target blood vessel and are calculated from an SDF image. We investigate the validity of the correction method in the simulation and the phantoms experiment.

### 1.2.2 $\text{SO}_2$ map and visualization of $\text{SO}_2$ transportation

In animal experiments *in vivo*, using the trial probe and the proposed SDF oximetry method, intravascular  $\text{SO}_2$  distribution maps are produced to visualize the transportation of oxygen bound to hemoglobin. To produce the  $\text{SO}_2$  maps, we proposed the blood vessel extraction method from an SDF image. Moreover, we show the procedure to produce  $\text{SO}_2$  maps. Finally, the transportation of oxygen is investigated using the maps. We show the distribution of  $\text{SO}_2$  along a blood vessel and a cross section of a vessel.

## 1.3 Structure of this thesis

The thesis is structured with the contents as follows:

- our developed SDF probes for obtaining spectral band images and a procedure of the gamma correction for the imaging camera are described in Chapter 2,

- our proposed SDF oximetry method using the SDF probe is explained in Chapter 3,
- as the first approach for evaluating the validity of the SDF oximetry method, the Monte Carlo photon propagation simulation experiments for a digital tissue model or biological tissue phantoms models are described in Chapter 4,
- an experiment using biological tissue-like phantoms is shown in Chapter 5,
- for visualizing oxygen transportation in microcirculation obtained from SDF images, the image processing such as a blood vessel extraction technique from SDF images and a procedure of producing  $\text{SO}_2$  maps are described in Chapter 6.
- finally, concluding remarks and future issues are given in Chapter 7.

# Chapter 2   SIDESTREAM DARK-FIELD (SDF) IMAGING

As shown in Chapter 1, the sidestream dark-field (SDF) imaging technique is a noninvasive optical imaging technique. This technique allows direct visualization of microcirculation and the analysis of RBCs' flow. To use this imaging technique, a trial SDF probe was developed using LEDs. Moreover, to obtain spectral band images of microcirculation, multicolor LEDs were used as illumination sources. In this chapter, the principle of the SDF imaging and trial SDF probes development are described in § 2.1 and § 2.2, respectively. The gamma correction of an imaging camera used in the probe is explained in § 2.3.

## 2.1 Principle of SDF imaging

The SDF imaging is a technique for assessing microcirculation near the surface of tissues [12, 13]. This technique uses a probe with attached illumination sources that are optically isolated from the path of light detection. Figure 2.1 schematically illustrates the concept of the SDF imaging. In this technique, the probe is pressed against an organ tissue of interest and epi-illumination occurs from illumination sources placed concentrically around the exterior tip of the probe. A portion of light emitted from the light sources, after being scattered within the tissue, is partly absorbed by hemoglobin molecules of RBCs in microvessels near the surface. Part of the light that re-emits from the surface and goes through the path in the core is imaged onto the image sensor of a camera. This technique prevents tissue surface reflections from contaminating microcirculatory images. Thus, by using the SDF imaging technique, we can obtain clear images of the microcirculatory network structure and RBC's flow.

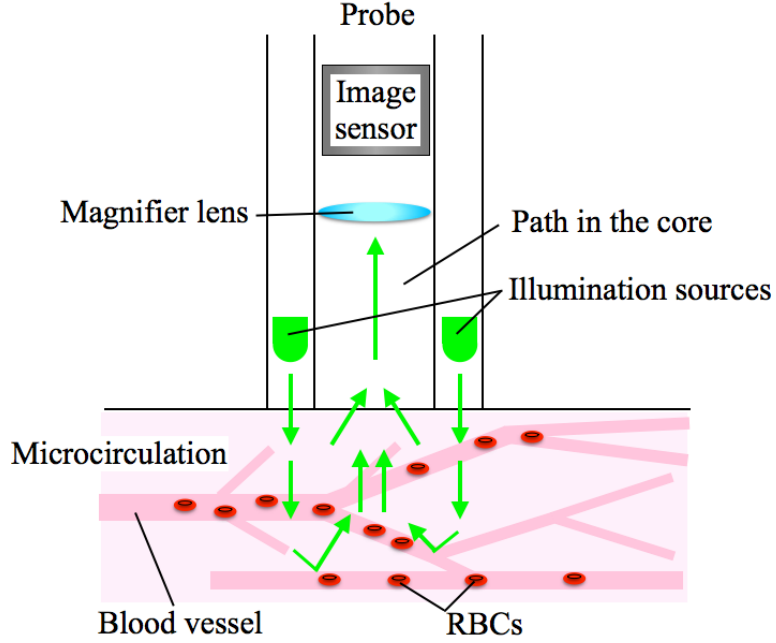


Fig 2.1: A schematic illustration of the SDF imaging. Light illuminated from sources around the exterior of the probe tip is scattered within a tissue and absorbed by hemoglobin, re-emitted from the tissue surface and then acquired by the image sensor (camera).

## 2.2 Development of SDF probe

### 2.2.1 The first generation of our SDF probe

Li and Kaneko *et. al* developed an SDF probe with multicolor LEDs as the first generation of the probe [53, 54]. Figure 2.2 shows the configuration of our SDF imaging system; Fig. 2.3 shows a probe with multicolor LED chips and an imaging camera. The system is exceedingly simple. Spectral band images can be obtained by changing the color of multicolor LEDs. The SDF probe is equipped with six LED chips placed around the exterior tip of the probe. The configuration of LED chips provides uniform illumination. The probe diameter is 13.5 mm and the detecting aperture is 2 mm. The incident angle of the direction of LED chips was  $16^\circ$  toward the path of light detection. The collecting location of light is about 15.1 mm from the surface of the silicon plate. As LED chips, multicolor LEDs (SMLV56RGB1W, ROHM Co., Ltd., Kyoto, Japan) was used. The size of the LED chip is 3.1 mm (height)  $\times$  2.8 mm (width). These LED chips could be switched from blue to green and red light. The peak

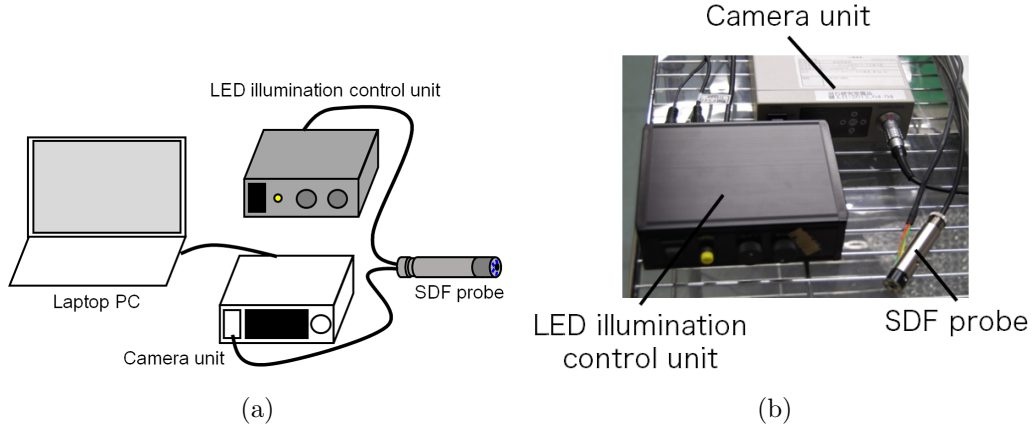


Fig 2.2: The system of our trial SDF imaging. (a) Main components of the system. (b) A photograph of the system of the first generation probe.

wavelengths of each color were 470 nm, 527 nm, and 624 nm and the bandwidths (FWHM) of each intensity distribution were 57.32 nm, 39.03 nm, and 16.27 nm, respectively. The reasons why we chose these wavelengths were, as shown in Fig. 2.4, a greater difference range between light absorption of  $\text{HbO}_2$  and Hb (470 nm), an isosbestic point (527 nm), a range of the light scattering domination (624 nm). The light with range of 400 ~ 600 nm wavelengths is well absorbed by hemoglobin and their penetration distance in a tissue is shorter than that of infrared light [55], so these wavelengths are suitable for observation of vessels near the surface. As an imaging camera, we used a charge-coupled device (CCD) camera (AS807SP, ARS CO., LTD, Yamanashi, Japan). The camera has a 1/6 inch sensor (Sony Corporation, Tokyo, Japan) and the signal format is NTSC/PAL. The diameter of the tip of the camera is 7 mm. The captured images have dimensions of  $640 \times 480$  pixels. The focus length of the lens is 4.0 mm.

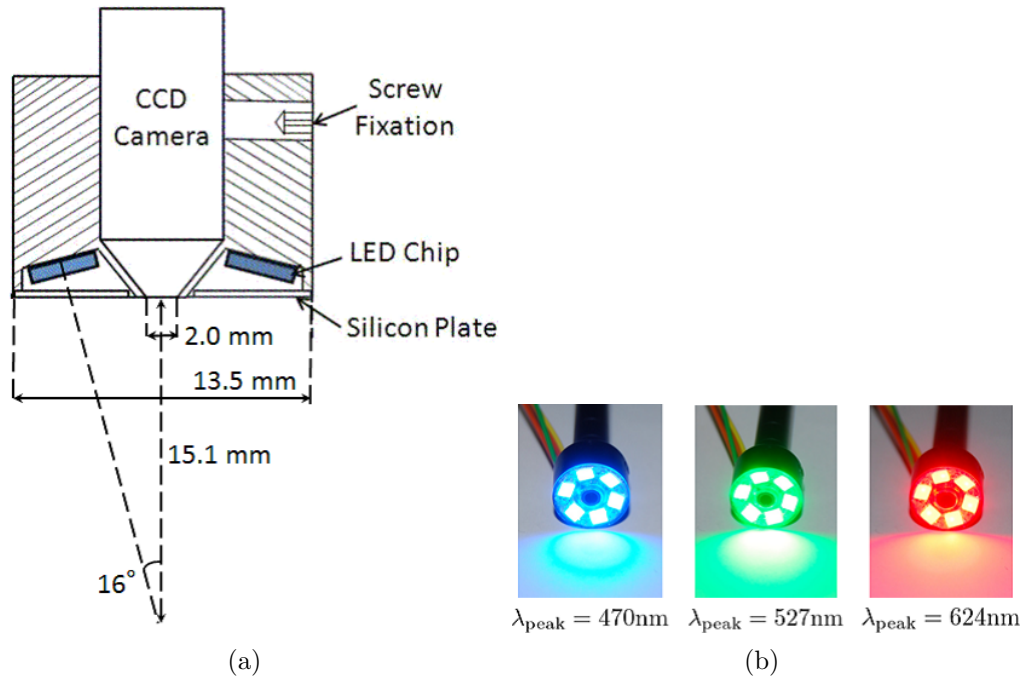


Fig 2.3: The trial SDF illumination probe. (a) A schematic diagram of the SDF probe. The outer diameter of this device was 13.5 mm. LED chips were used as illumination. (b) This LED chip could be switched from blue light at the peak wavelength of 470 nm to green light at 527 nm.

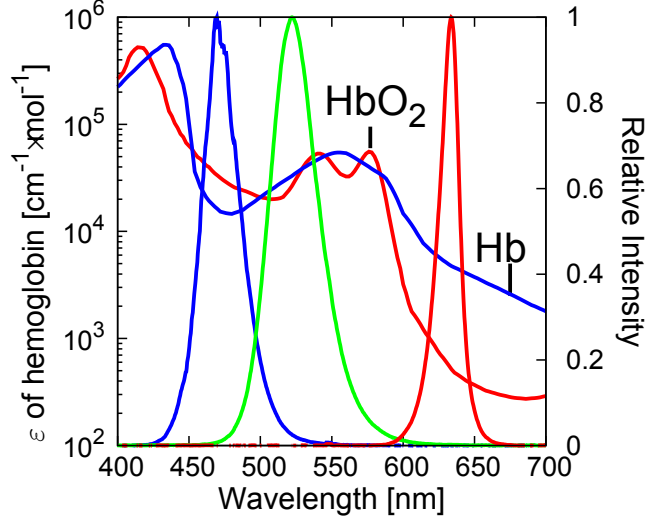


Fig 2.4: Spectral distribution of molar extinction coefficients  $\varepsilon$  of oxygenated hemoglobin ( $\text{HbO}_2$ ) and de-oxygenated hemoglobin (Hb) (left axis) [10] and spectral intensity distribution of the three-color LEDs (SMLV56RGB1W) with the relative intensity (right axis).

### 2.2.2 The second generation

We improved the first generation SDF probe by changing both an incident angle of the direction of the light sources and an imaging camera. As well as the first generation, we developed a trial SDF probe to implement spectral band image acquisition by changing the color of the multicolor LEDs used. Figures 2.5(a) and 2.5(b) show the configuration of our SDF imaging system; Fig. 2.5(c) is a schematic diagram of our trial SDF probe; and Fig. 2.5(d) shows photographs of three-color LEDs.

This generation SDF probe is also exceedingly simple. It is equipped with six LED chips placed around the exterior tip of the probe to provide uniform illumination. The size is the same as the previous probe, diameter is 13.5 mm and the detecting aperture is 2 mm. Since the LED illuminations have directional light characteristics, they are installed at a tilted angle of  $53^\circ$  toward the path of light detection to strengthen the intensity of light irradiated to the target region. The collecting location of light is about 4.4 mm from the surface of the silicon plate. This location is shorter than the probe of the first generation. As a LED, we used multicolor LED (SMLVN6RGB1W, ROHM Co., Ltd., Kyoto, Japan). The size of each LED



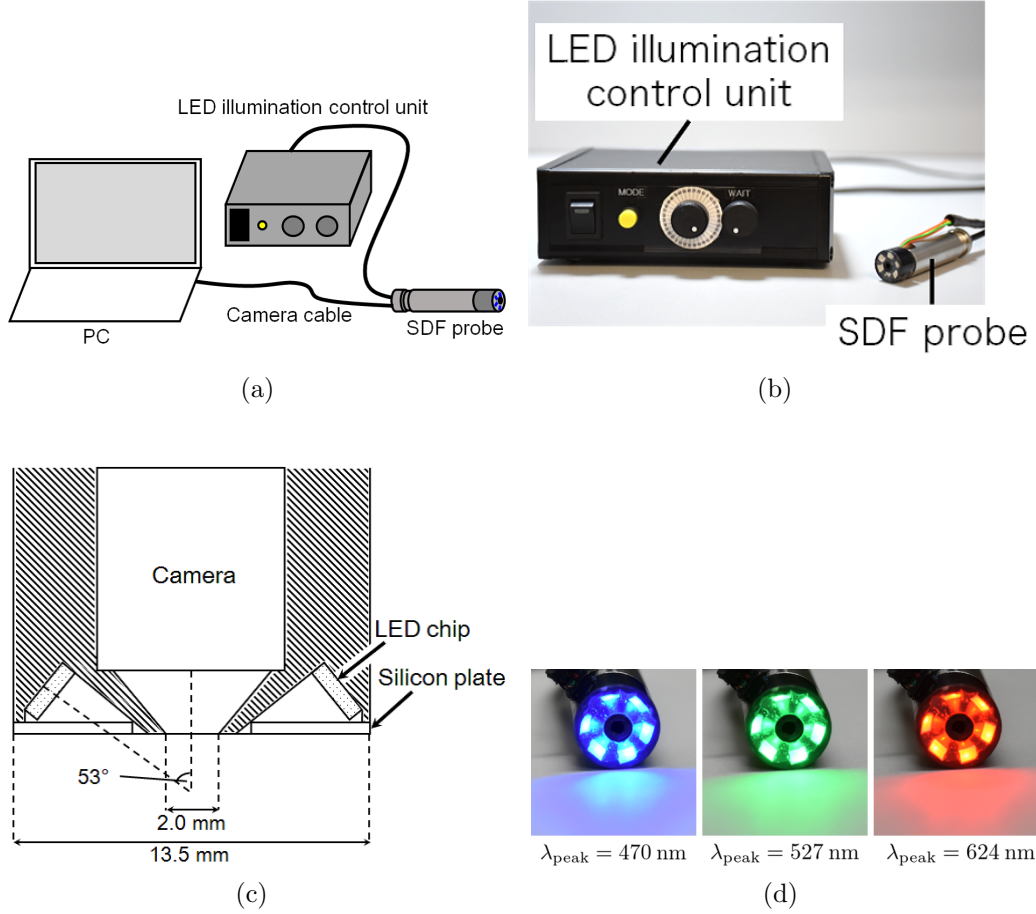


Fig 2.5: The second generation of our trial SDF imaging probe and the system. (a) The system. (b) A photograph of the system. (c) Schematic for the tip of the trial SDF probe. (d) Photographs of the tip with three-color LEDs. The colors are blue with 470 nm peak wavelength, green with 527 nm, and red with 624 nm.

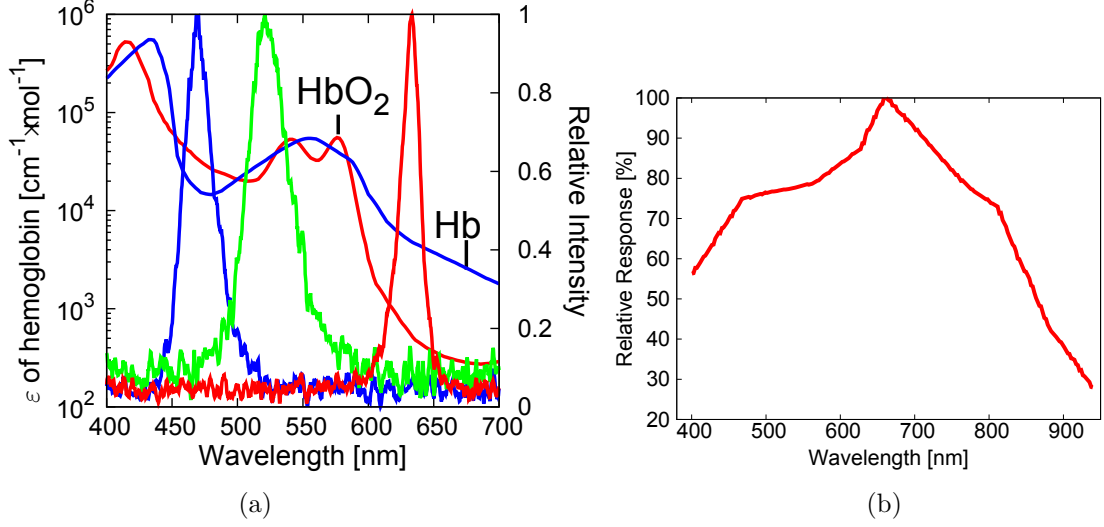


Fig 2.6: Characteristics of the imaging camera. (a) Spectral distribution of molar extinction coefficients  $\epsilon$  of oxygenated hemoglobin (HbO<sub>2</sub>) and de-oxygenated hemoglobin (Hb) (left axis) [10] and spectral intensity distribution of the three-color LEDs (SMLVN6RGB1W) with the relative intensity (right axis). (b) The spectral response with reference to data sheet described by the manufacturer [61].

is 3.1 mm (height)  $\times$  2.8 mm (width).

The spectral intensity of the LED chip is shown in Fig. 2.6(a) together with molar extinction coefficients  $\epsilon$  for hemoglobin from the literature [10]. Molar extinction coefficients are also known as molar attenuation coefficients. The peak wavelengths of the LED chips are 470 nm (blue), 527 nm (green), and 624 nm (red). The bandwidths (FWHM) of each intensity distribution were 28.09 nm, 40.40 nm, and 17.94 nm, respectively. As described later, for the SO<sub>2</sub> estimation, 470 nm and 527 nm peak wavelength images are employed. We assembled a LED illumination control unit for switching the color and adjusting the duty ratio of the LED chip and blinking period.

As an imaging device, we use a CMOS miniature video camera (ID04MB-IP-U, iDule Corporation, Chiba, Japan). The imaging sensor is a diagonal length 3.258 mm CMOS. The spectral response is shown in Fig 2.6(b). The output interface is USB3.0. The diameter of the tip is 6 mm. The captured images have dimensions of 640  $\times$  640 pixels. The focus length of the lens is 5.6 mm. Since the minimum time interval of the changing the color is about

Table 2.1: Specification of our SDF probes.

		First generation	Second generation
Probe	Size	13.5 mm diameter	
	Light incident angle	16°	53°
LED	product	SMLV56RGB1W (ROHM Co., Ltd., Kyoto, Japan)	SMLVN6RGB1W (ROHM Co., Ltd., Kyoto, Japan)
	Color	Blue, Green, Red	
	Peak wavelength	470, 527, 624 nm	
	FWHM [nm]	57.3, 39.0, 16.3	29.1, 40.4, 17.9
Imaging camera	product	AS807SP (ARS CO., LTD, Yamanashi, Japan)	ID04MB-IP-U ( iDule Corporation, Chiba, Japan)
	Sensor	CCD	CMOS
	Signal	Analog (NTSC/PAL)	Digital

100 ms, the number of one-band images obtained per one color is three for a 30 fps.

The summary for specification of both first and second generation of our SDF probe is shown in Table 2.1.

## 2.3 Gamma correction

To use pixel values for measuring light intensity, the relationship between a response of an imaging camera and light intensity detected with the camera is needed to be known. The gamma correction of the imaging camera makes this relationship linear. As a calibration object, a grayscale pattern slide (EIA GrayScale Pattern Slide, Edmund Optics Inc., Barrington, New Jersey, USA) was used as shown in Fig. 2.7(a). This slide has nine patterns with transmittance of 3.000%, 10.125%, 17.250%, 24.375%, 31.500%, 38.625%, 45.750%, 52.875% and 60.000%. Environment of determining parameters of the gamma correction is shown in Fig. 2.7(b). LEDs of the second generation probe were used as illumination sources, and the diffusion film was configured in between the illumination sources and the pattern slide to make

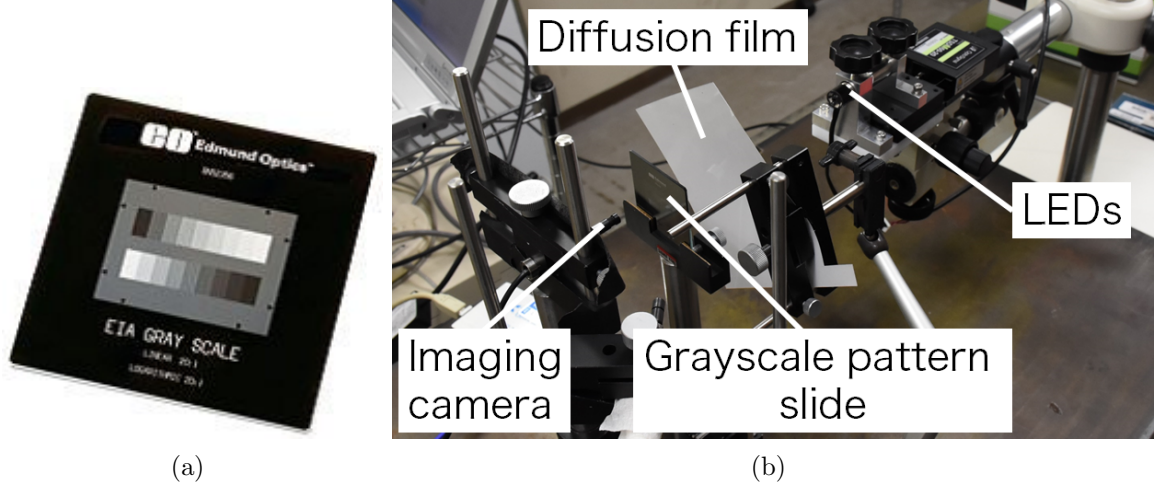


Fig 2.7: Environment of determining parameters for the gamma correction. (a) A grayscale pattern slide. (b) Environment of determining parameters.

the illumination spatially uniform. Figure 2.8 also shows a image of this slide obtained by the camera (ID04MB-IP-U, iDule Corporation, Chiba, Japan) with a 33 ms exposure time.

A pixel value  $p_T(x, y)$  at  $(x, y)$  of an image of the pattern with transmittance  $T$  obtained by the imaging camera is normalized using one of a no-slide image (i.e.  $T = 100\%$ ) and a dark-current image (i.e.  $T = 0\%$ ):

$$\bar{p}_T(x, y) = \frac{p_T(x, y) - p_{\text{dark}}(x, y)}{p_{T=100\%}(x, y) - p_{\text{dark}}(x, y)}, \quad (2.1)$$

where  $p_{T=100\%}(x, y)$  and  $p_{\text{dark}}(x, y)$  are a pixel value at  $(x, y)$  of the no-slide and the dark-current image, respectively. The relationship at  $(x, y)$  between  $\bar{p}_T(x, y)$  and  $T$  is given by:

$$\bar{p}_T(x, y) = \alpha(x, y) \cdot T^{\gamma(x, y)}, \quad (2.2)$$

where  $\alpha(x, y)$  and  $\gamma(x, y)$  are coefficients at  $(x, y)$ . Thus, when a camera image is converted to a light intensity (transmittance) image, the transmittance image  $T(x, y)$  is obtained by:

$$T(x, y) = \left( \frac{\bar{p}(x, y)}{\alpha(x, y)} \right)^{1/\gamma(x, y)}. \quad (2.3)$$

When  $\alpha(x, y)$  and  $\gamma(x, y)$  are constant throughout the image, Eq. (2.3) is rewritten as:

$$T(x, y) = \left( \frac{\bar{p}(x, y)}{\alpha} \right)^{1/\gamma}. \quad (2.4)$$

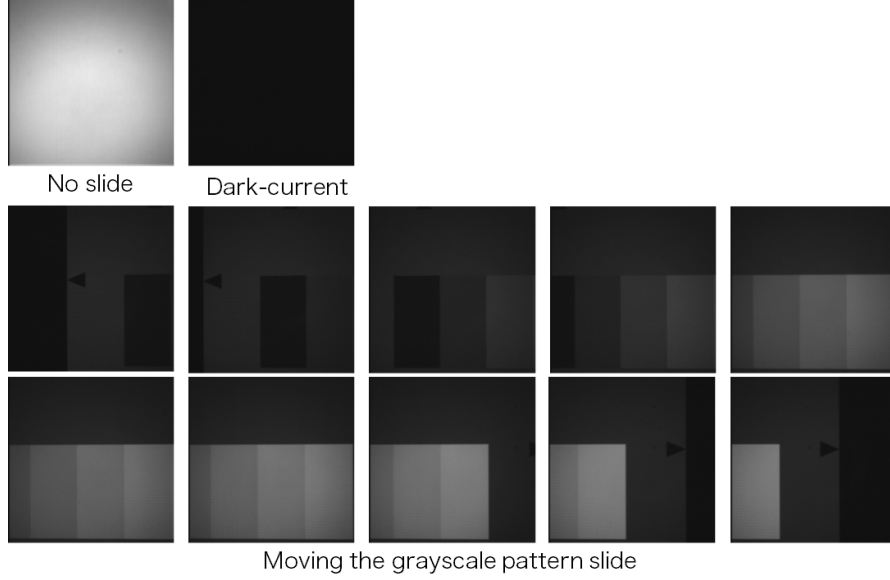


Fig 2.8: Images of grayscale pattern slide. Images of no-slide, dark-current (the top rows) and several patterns of the moved slide (two rows of the bottom).

In this study,  $\alpha$  and  $\gamma$  are calculated in each region of interest (ROI) while the grayscale pattern slide was moved. First, we set seven ROIs in an image as shown in Fig. 2.9. To calculate  $\alpha$  and  $\gamma$  in a  $i$ -th ROI with a  $n \times n$  size, the average pixel values  $\tilde{p}$  in the ROI is used:

$$\tilde{p}_i = \frac{1}{n^2} \sum_{(x,y) \in \text{ROI}} p(x,y). \quad (2.5)$$

The average of  $\alpha$  and  $\gamma$  are determined by using Eq. (2.2) with  $\tilde{p}_i$  instead of  $\bar{p}(x,y)$ :

$$\tilde{p}_{T,i} = \tilde{\alpha}_i \cdot T^{\tilde{\gamma}_i}. \quad (2.6)$$

Results of  $\tilde{\alpha}$  and  $\tilde{\gamma}$  of seven ROIs are shown in Table 2.2 and Fig. 2.10. In Fig. 2.10, the relationship between  $\tilde{p}$  and  $T$  (blue solid lines) of seven ROIs and the average (red dashed lines) for blue, green, and red illumination are represented. From the results, we could not find the differences in the relationships between ROIs and between illuminations. The variation of  $\tilde{p}$  over  $\Delta T$  is calculated by differentiating Eq. (2.6):

$$\Delta \tilde{p} = \tilde{\alpha} \tilde{\gamma} \cdot T^{\tilde{\gamma}-1} \Delta T, \quad (2.7)$$

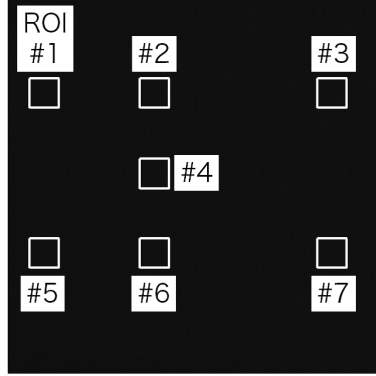


Fig 2.9: The location of seven ROIs in the image.

where  $\Delta\tilde{p}$  represents the variation of  $\tilde{p}$  over  $\Delta T$ . We calculated  $\Delta\tilde{p}$  over  $\Delta T = 1\%$ . In Table 2.3, the average of  $\Delta\tilde{p}$  over  $T$  and results of conversion of the range of  $[0, 1]$  to  $[0, 255]$  by multiplying  $\Delta\tilde{p}$  by 255. From these values, we approximately determined the change of a pixel values with respect to the change of the transmittance.

From the results of  $\Delta\tilde{p}$  in Table 2.3, the difference between the maximum and the minimum value was less than 1. This means that there was no difference of the increment of pixel values at each location for 1% increase in the transmittance. Thus, we found that the relationship between camera response and the light intensity was uniform in the sensor. In this study, we used the average value of  $\tilde{\alpha}$  and  $\tilde{\gamma}$  for each color to obtain the transmittance image:

$$\begin{aligned}
T_{\text{Blue}}(x, y) &= \left( \frac{p_{\text{Blue}}(x, y)}{5.060 \times 10^{-3}} \right)^{1/1.145}, \\
T_{\text{Green}}(x, y) &= \left( \frac{p_{\text{Green}}(x, y)}{4.744 \times 10^{-3}} \right)^{1/1.159}, \\
T_{\text{Red}}(x, y) &= \left( \frac{p_{\text{Red}}(x, y)}{4.620 \times 10^{-3}} \right)^{1/1.165},
\end{aligned} \tag{2.8}$$

where  $T_{\text{Blue}}$ ,  $T_{\text{Green}}$ , and  $T_{\text{Red}}$  are the transmittance image of blue, green, and red illumination, respectively.  $p_{\text{Blue}}$ ,  $p_{\text{Green}}$ , and  $p_{\text{Red}}$  are a pixel value of an SDF image of blue, green, and red illumination.

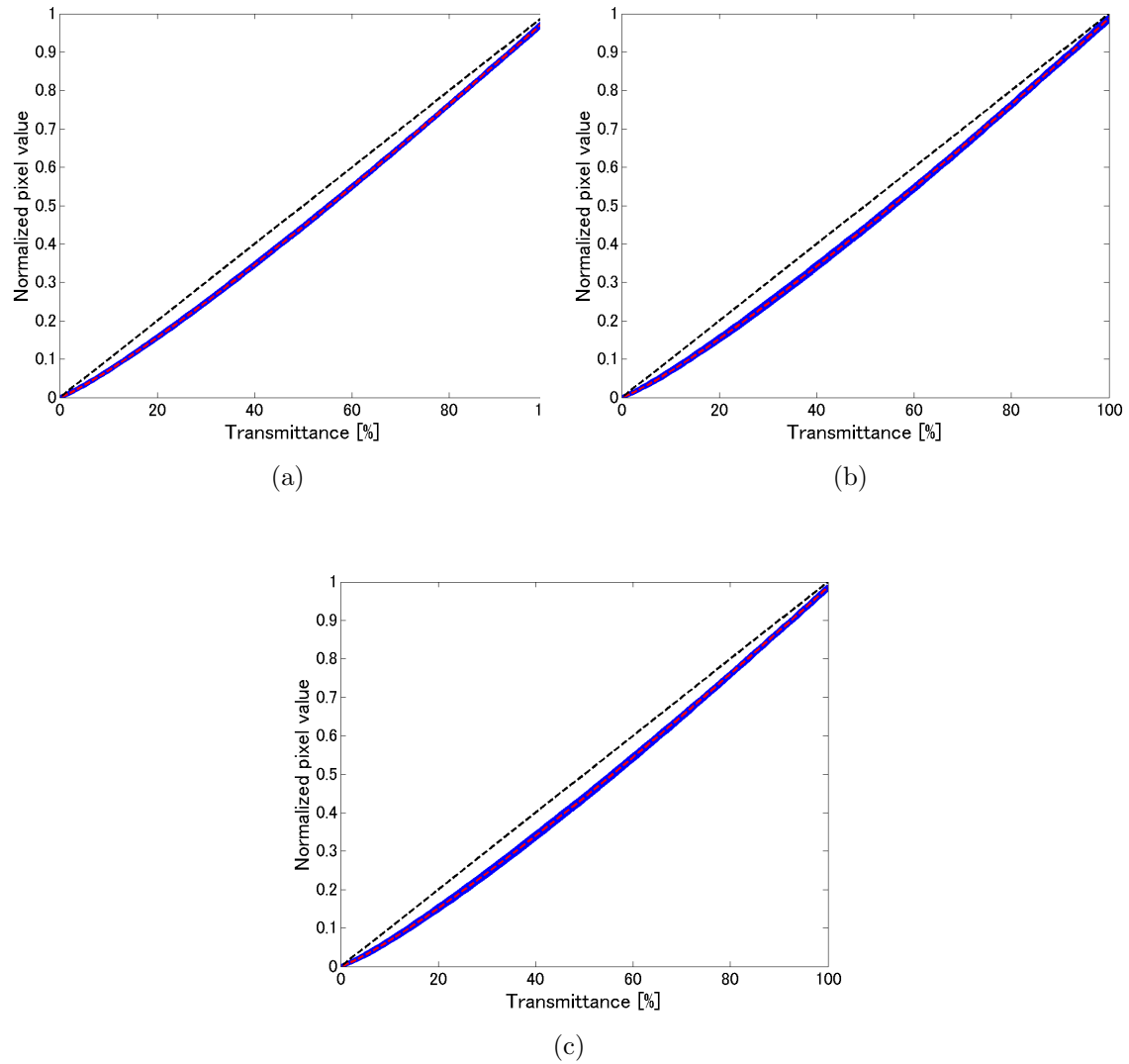


Fig 2.10: The relationship between the normalized pixel value and the transmittance of the grayscale pattern slide under illumination of (a) blue, (b) green, and (c) red. The relationship of each ROI and the average of that are depicted by blue solid and red dashed lines, respectively.

Table 2.2: Results of  $\tilde{\alpha}$  and  $\tilde{\gamma}$  using three-color LEDs.

ROI	Color of illumination sources					
	Blue		Green		Red	
	$\tilde{\alpha} [\times 10^{-3}]$	$\tilde{\gamma}$	$\tilde{\alpha} [\times 10^{-3}]$	$\tilde{\gamma}$	$\tilde{\alpha} [\times 10^{-3}]$	$\tilde{\gamma}$
#1	4.886	1.153	4.794	1.158	4.633	1.165
#2	4.963	1.149	4.643	1.164	4.645	1.163
#3	5.343	1.133	5.282	1.135	5.131	1.141
#4	4.860	1.153	4.359	1.177	4.216	1.184
#5	4.964	1.149	4.668	1.163	4.632	1.164
#6	5.176	1.140	4.542	1.168	4.426	1.174
#7	5.228	1.137	4.918	1.150	4.659	1.162
Avg. (S.D.)	5.060 (0.173)	1.145 (0.008)	4.744 (0.274)	1.159 (0.013)	4.620 (0.258)	1.165 (0.012)

Table 2.3: Results of  $\Delta\tilde{p}$ .

ROI	Average of $\Delta\tilde{p}$ over $T [\times 10^{-3}]$			$\Delta\tilde{p} \times 255$		
	Blue	Green	Red	Blue	Green	Red
#1	9.722	9.734	9.720	2.479	2.482	2.479
#2	9.756	9.800	9.761	2.488	2.499	2.489
#3	9.726	9.753	9.730	2.480	2.487	2.481
#4	9.710	9.706	9.703	2.476	2.475	2.474
#5	9.732	9.758	9.743	2.482	2.488	2.484
#6	9.725	9.729	9.720	2.480	2.481	2.479
#7	9.687	9.688	9.689	2.470	2.471	2.471
Avg.	9.723	9.738	9.724	2.479	2.483	2.480
Max.-Min.				0.018	0.028	0.018

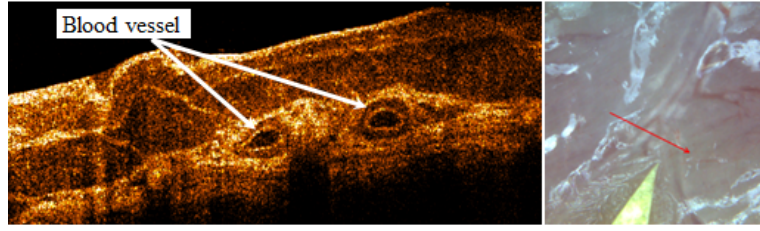


## Chapter 3 SDF OXIMETRY

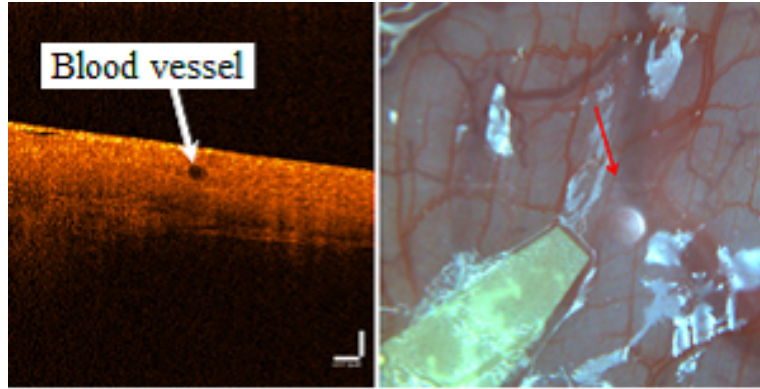
An intravascular oxygen saturation estimation method from spectral band images obtained by SDF imaging, that is called SDF oximetry, is introduced in this chapter. To establish the method, as the first step, the structure of within a target tissue was investigated using other modalities such as optical coherence tomography or stained specimen shown in § 3.1. To formulate the light attenuation, we used the Lambert-Beer law as a basic principle. The Lambert-Beer law for biological tissues is explained in § 3.2. Then, the SDF oximetry method has been established using the Lambert-Beer law in § 3.3. As shown in Chapter 2, since we assume to use both the LEDs and a typical imaging camera in the SDF oximetry, hemoglobin extinction coefficients are modified with reference to the previous study of the retinal oximetry for spectroscopy in § 3.4. Moreover, by considering the light paths in SDF imaging, the correction method for light scattering was proposed in § 3.6.

### 3.1 Model of light behavior near organ's tissue surface

As the first approach, the structure under the surface of target tissues was investigated and constructed a model of light propagation in tissues for SDF imaging. To understand the positions of blood vessels and surrounding structures observed by the SDF imaging, we closely examined the surface of a pig's small intestine which is similar to that of a human's. In the experiment, the surface of the small intestine was observed with an optical coherence tomography (OCT) equipment (Ganymede, Thorlabs, Inc., Newton, New Jersey, USA) *in vitro* and *in vivo*. In the observation *in vitro*, we used a blood-drained small intestine of a pig that had been slaughtered for food. In the observation *in vivo*, a pulled out small intestine was used after having made an incision in the pig abdomen. Moreover, the small intestine was resected and stained with a hematoxylin and eosin (HE). Figures 3.1(a) and 3.1(b) show OCT images *in vitro* and *in vivo* respectively and color photographs captured by a color camera



(a)



(b)

Fig 3.1: Results of the observation of a pig small intestine using the OCT equipment (a) *in vitro* and (b) *in vivo*. These images are the cross section along the red arrow of the inset color photograph on the right. There are blood vessel near the surface.

built into the OCT equipment. Figure 3.2(a) shows images of the HE stained specimen of the small intestine prepared in the *in vivo* experiment. From the observation *in vitro*, the tissue structure and blood vessels were confirmed because the blood had been drained. Moreover, in the observation *in vivo*, there exist some blood vessels with blood near the surface. The blood vessels were about  $100\ \mu\text{m}$  from the surface. Next, from the observation of the HE stained specimen images, the blood vessels observed by SDF imaging were clearly confirmed in the outermost thin layer. The thin layer that covers the small intestine is known as the serosa. The structures behind the serosa such as the muscularis and submucosa with the stained specimen were also observed as shown in Fig. 3.2(b).

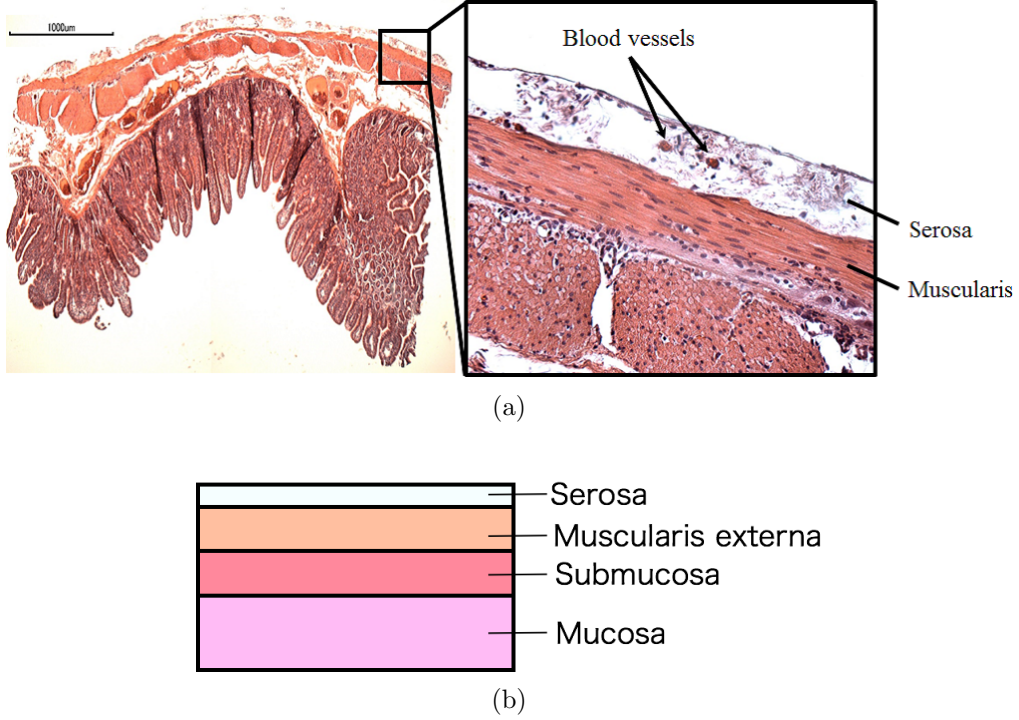


Fig 3.2: Results of the observation of the HE stained specimen. (a) The microscopic image of the HE stained specimen. The inset on the right is an enlarged image that shows blood vessels in the serosa. (b) The layer structure of a small intestine.

### 3.2 Lambert-Beer law for biological tissues

An oximetry method based on the Lambert-Beer law for biological tissues is shown in this section. Let us consider incident light of intensity  $I_{\text{in}} = I_{\text{in}}(\lambda)$  at wavelength  $\lambda$ . When the incident light enters into a medium with a thickness  $d$ , the Lambert-Beer law gives the intensity  $I_{\text{out}} = I_{\text{out}}(\lambda)$  of the transmitted light through the medium as:

$$I_{\text{out}} = I_{\text{in}} \cdot 10^{-\mu_a(\lambda)d}, \quad (3.1)$$

where  $\mu_a(\lambda)$  represents an *absorption coefficient* that can be written by  $\mu_a(\lambda) = \varepsilon(\lambda)c$ , in which  $\varepsilon(\lambda)$  is an *extinction coefficient* and  $c$  is the concentration of the absorber in the medium. Using this expression, we define *optical density*  $D = D(\lambda)$  as:

$$D = -\log \left( \frac{I_{\text{out}}}{I_{\text{in}}} \right) = \mu_a(\lambda)d. \quad (3.2)$$

We consider that the medium is blood and assume that the incident light is absorbed by only hemoglobin<sup>1</sup>, then  $\mu_a(\lambda)$  is written as:

$$\mu_a(\lambda) = [s\varepsilon_{\text{HbO}_2}(\lambda) + (1 - s)\varepsilon_{\text{Hb}}(\lambda)] c, \quad (3.3)$$

where  $\varepsilon_{\text{HbO}_2}(\lambda)$  and  $\varepsilon_{\text{Hb}}(\lambda)$  represent the extinction coefficients of the oxygenated and the de-oxygenated hemoglobin respectively,  $c$  represents the hemoglobin total concentration, and  $s$  is the oxygen saturation ( $\text{SO}_2$ ). To be exact, the optical density  $D(\lambda)$  for real blood needs to be corrected with an additional term [56]. However, we will use the above simple form here and modify it in the next section. To estimate the saturation  $s$  in the case that  $\varepsilon_{\text{HbO}_2}(\lambda)$  and  $\varepsilon_{\text{Hb}}(\lambda)$  are known, we solve the follow equations for  $s$  using different wavelengths  $\lambda_1$  and  $\lambda_2$ :

$$\begin{aligned} D(\lambda_1) &= [s\varepsilon_{\text{HbO}_2}(\lambda_1) + (1 - s)\varepsilon_{\text{Hb}}(\lambda_1)] cd, \\ D(\lambda_2) &= [s\varepsilon_{\text{HbO}_2}(\lambda_2) + (1 - s)\varepsilon_{\text{Hb}}(\lambda_2)] cd. \end{aligned} \quad (3.4)$$

Next, we define the ratio of  $D(\lambda_1)$  and  $D(\lambda_2)$  as  $\Phi = \Phi(\lambda_1, \lambda_2)$ , which is called *the saturation parameter* in reference [35] by:

$$\Phi(\lambda_1, \lambda_2) = \frac{D(\lambda_2)}{D(\lambda_1)}. \quad (3.5)$$

From Eqs. (3.4) and (3.5), we obtain the saturation  $s$  as:

$$s = \frac{\Phi\varepsilon_{\text{Hb}}(\lambda_1) - \varepsilon_{\text{Hb}}(\lambda_2)}{\Delta\lambda_2 - \Phi\Delta\lambda_1}, \quad (3.6)$$

where  $\Delta\lambda_n := \varepsilon_{\text{HbO}_2}(\lambda_n) - \varepsilon_{\text{Hb}}(\lambda_n)$  for  $n = 1, 2$ . It should be noted that we do not have to know  $c$  and  $d$  to solve for  $s$ .

In the discussion above, the oximetry method does not include the reflected light from the medium. In reality, however, there is a portion of light that returns from the surface of the medium in which light enters into. When a medium is highly scattering, the ratio of the reflected light is larger than the transmitted light. Therefore, the Lambert-Beer law can be applied to the reflected intensity of light in the case of a highly scattering medium [56]. A biological tissue is a highly scattering medium, hence the saturation  $s$  of a tissue can be estimated from Eq. (3.6) based on the Lambert-Beer law in principle, but there are some

---

<sup>1</sup>Both influence of other components of blood for light absorption and cases where this assumption holds are shown in Appendix A.

uncertainties such as light path length and the effect of scattering. Thus, many studies, as reviewed in [56], have suggested an appropriate way to correct them for each modality. In the case of reflected light, the optical density  $D = D(\lambda)$  of Eq. (3.2) can be written by using the reflectance  $R = R(\lambda)$ :

$$D = -\log R. \quad (3.7)$$

As with the transmitted light, Eq. (3.6) can be applied to estimating  $s$  by measuring the reflectance.

### 3.3 SDF oximetry

An SDF oximetry method that estimates the  $\text{SO}_2$  from SDF images of a vessel is proposed here. The proposed method is constructed in an analogy to retinal oximetry methods. The SDF oximetry method uses two band SDF images. When applying retinal oximetry methods to SDF imaging, differences between the retinal oximetry [35] and the SDF oximetry must be considered. As presented in Fig. 3.3, there is a difference in the light paths. In retinal oximetry (Fig. 3.3(a)), photons backscattered from the vessel mainly contribute to the detected intensity at the vessel part in a retinal fundus image [57]. In contrast, photons that pass once the vessel (single pass) mainly contribute to that in a SDF image (Fig. 3.3(b)). In the SDF technique, light enters a tissue from illumination sources configured around the camera and then the camera captures the light scattered by the tissue. Consequently, we apply retinal oximetry methods to the SDF oximetry keeping in mind the above consideration.

Let us consider the proposed SDF oximetry method. Figures 3.4(a) and (b) show a concept of the proposed method. As shown in Figs. 3.4(a) and (b), Consider the light that enters the body of a medium with intensity  $I_0(\lambda)$  and returns outside without passing through any vessels as back reflection light near a target blood vessel and its intensity as  $I_{\text{in}}(\lambda) = R(\lambda)I_0(\lambda)$  where  $R(\lambda)$  denotes the total reflectance of layers behind the vessel near a surface, e.g. muscularis, submucosa, and mucosa. Next, the same amount of reflecting light illuminates the vessels is assumed. Therefore, the intensity of the transmitted light can be expressed in terms of  $I_0$  as in Eq. (3.1):

$$I_{\text{out}} = I_{\text{in}}(\lambda) \cdot 10^{-\mu_a(\lambda)d} = R(\lambda)I_0(\lambda) \cdot 10^{-\mu_a(\lambda)d}, \quad (3.8)$$

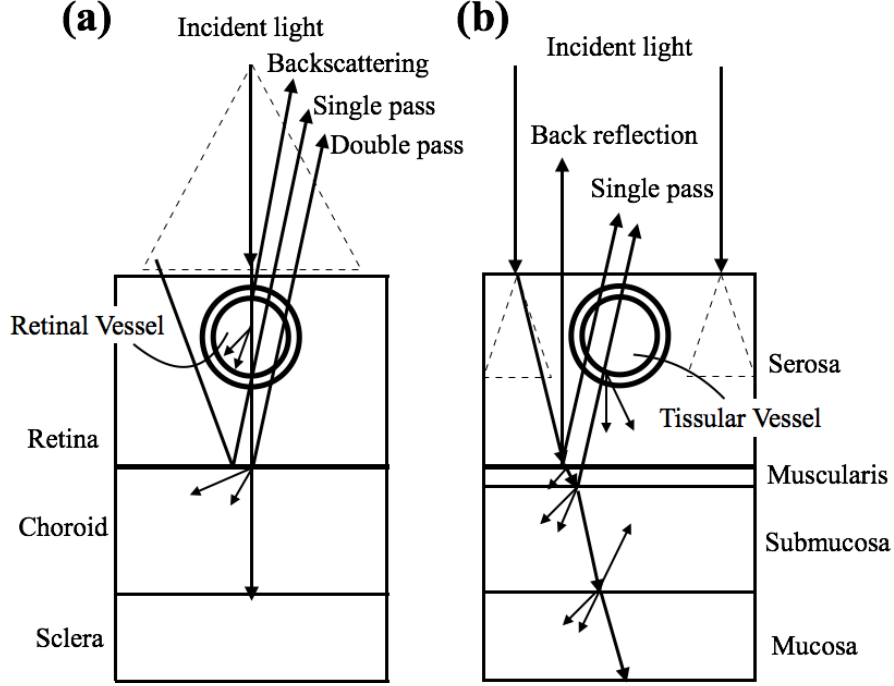


Fig 3.3: Light paths for retinal and SDF imaging. (a) For a retinal fundus camera. Three paths can be considered: incident light is backscattered from a blood vessel (backscattering); reflected or scattered light passes once through a vessel (single pass); the light passes twice through a vessel (double pass). (b) For a SDF imaging system. In contrast with a fundus camera, there is no backscattered light. The dashed line triangles denote the illumination area.

where  $\mu_a(\lambda)$  is the absorption coefficient defined in Eq. (3.3). Here we ignore the effect of photons that pass more than twice through the vessel (double pass) because all photons enter the peripheral region of the target vessel and most of them pass through the vessel once at most. In this case, the optical density  $D(\lambda)$  of blood can be written as:

$$D(\lambda) = \mu_a(\lambda)d = [s\varepsilon_{\text{HbO}_2}(\lambda) + (1-s)\varepsilon_{\text{Hb}}(\lambda)]cd. \quad (3.9)$$

As in the previous section, we define *the saturation parameter* by:  $\Psi(\lambda_1, \lambda_2) = D(\lambda_2)/D(\lambda_1)$ . To determine  $s$ , we solve Eq. (3.9) for  $s$  with two wavelengths  $\lambda = \lambda_1, \lambda_2$  and we obtain:

$$s = \frac{\Psi\varepsilon_{\text{Hb}}(\lambda_1) - \varepsilon_{\text{Hb}}(\lambda_2)}{\Delta\lambda_2 - \Psi\Delta\lambda_1}, \quad (3.10)$$

where  $\Psi = \Psi(\lambda_1, \lambda_2)$  and  $\Delta\lambda_n := \varepsilon_{\text{HbO}_2}(\lambda_n) - \varepsilon_{\text{Hb}}(\lambda_n)$  for  $n = 1, 2$ .

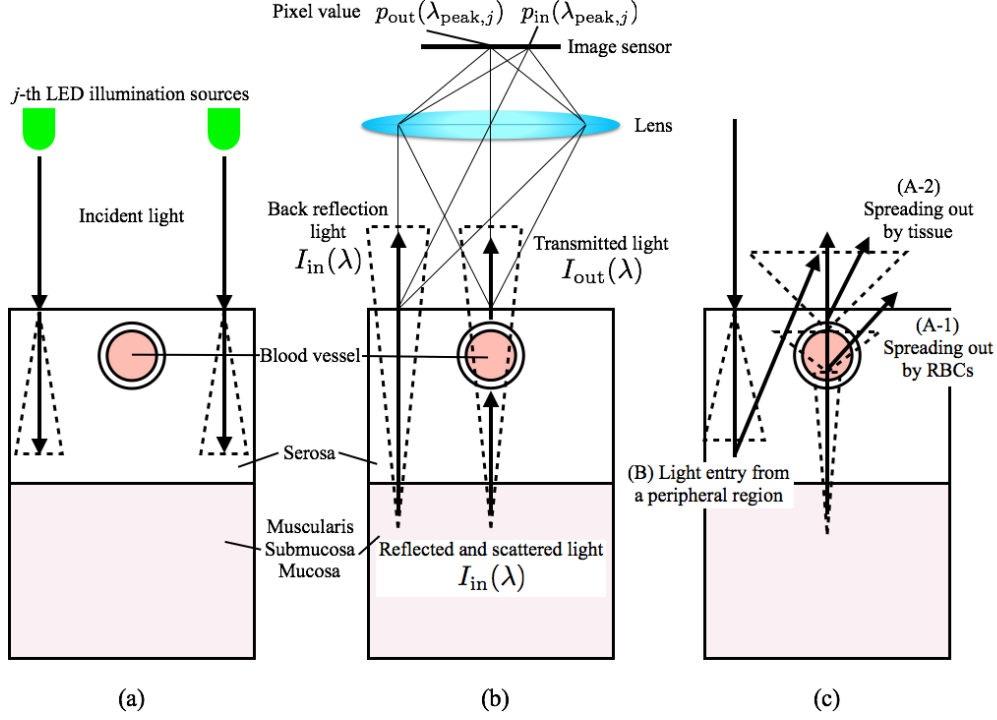


Fig 3.4: Schematic illustration of the proposed SDF oximetry method. (a) Incidence of light onto a tissue in the SDF geometry. (b) Back reflection light ( $I_{in}(\lambda)$ ) that is reflected within the tissue and re-emitted without going through the blood vessel and the transmitted light ( $I_{out}(\lambda)$ ) through the blood vessel. These light intensities are measured as pixel values:  $p_{in}$  and  $p_{out}$ . (c) Two causes of blur in the SDF image.

In use of our SDF probe for the SDF oximetry, band images are obtained by switching color of LEDs. Since the speed of RBCs in microcirculation is about  $1000 \mu\text{m/s}$  [25], a travel distance of RBCs is  $\sim 100 \mu\text{m}$  for 100 ms that is color-switching time. Thus, in this study, we assumed that  $\text{SO}_2$  of flowing blood at a certain location does not change significantly during the color-switching time.

### 3.4 Average extinction coefficient

Light-emitting diodes (LEDs) are commonly used as illumination sources in SDF imaging [13, 14]. As discussed in the previous section, monochromatic light is required for the  $\text{SO}_2$  estimation. Thus, the effect of bandwidth of the LEDs must be considered since the bandwidth

cannot be ignored. Moreover, a typical camera detects intensity of light by integrating over all wavelengths. Hence, the effect of this integration must be also considered on the  $\text{SO}_2$  estimation. In order to address these issues, the extinction coefficients of hemoglobin are modified by averaging over the wavelength in the  $\text{SO}_2$  estimation by referring to [35].

First, the general case is discussed. As mentioned earlier, the optical density of real blood is written with an additional term [56] by:

$$D(\lambda) = \mu_a(\lambda)d + B(\lambda), \quad (3.11)$$

where  $d$  is the inner diameter of a vessel,  $\mu_a(\lambda)$  represents the absorption coefficient of hemoglobin. The additional term  $B(\lambda)$  represents a correction for the RBC geometry and the detector geometry, and all phenomena other than the absorption of hemoglobin such as scattering and the sieve effect [58]. The sieve effect is a discrepancy between spectral absorption of RBCs and that of hemoglobin itself. Its dominant wavelength range is approximately from 370 to 430 nm. Fortunately, since this wavelength range is far from that of LED used in this study as shown in Chapter 2, this effect is negligible.

Let us consider the incident light with the intensity  $I_{p,j} = I(\lambda_{\text{peak},j})$  at the peak wavelength  $\lambda_{\text{peak},j}$  from  $j$ -th color of LEDs used and the relative spectral distribution  $F_j(\lambda)$  of the light  $I_{p,j}$  which has a value of unity at the peak, i.e. the intensity of light represents  $I_{p,j}F_j(\lambda)$ . A camera detects the intensity of the light transmitting through the vessel as:

$$\bar{I}_{\text{out}}(\lambda_{\text{peak},j}) = \int_{\Omega} d\lambda R(\lambda)S(\lambda)I_{p,j}F_j(\lambda) \cdot 10^{-[\mu_a(\lambda)d+B(\lambda)]}, \quad (3.12)$$

where  $S(\lambda)$  represents the sensitivity of the imaging camera,  $R(\lambda)$  represents the total reflectance of layers behind the vessel, and  $\Omega$  represents the spectral sensitivity region of the camera. The intensity of light outside a vessel is written by:

$$\bar{I}_{\text{in}}(\lambda_{\text{peak},j}) = \int_{\Omega} d\lambda R(\lambda)S(\lambda)I_{p,j}F_j(\lambda). \quad (3.13)$$

Similarly to Eq. (3.2), the optical density is defined as:

$$\bar{D}(\lambda_{\text{peak},j}) = -\log \left[ \frac{\bar{I}_{\text{out}}(\lambda_{\text{peak},j})}{\bar{I}_{\text{in}}(\lambda_{\text{peak},j})} \right], \quad (3.14)$$

in consideration of the influence of the integral detection by the camera and the bandwidth



of an illumination by:

$$\begin{aligned}\bar{D}(\lambda_{\text{peak},j}) &= -\log \left[ \frac{\int_{\Omega} d\lambda R(\lambda) S(\lambda) F_j(\lambda) \cdot 10^{-[\mu_a(\lambda)d+B(\lambda)]}}{\int_{\Omega} d\lambda R(\lambda) S(\lambda) F_j(\lambda)} \right] \\ &=: [s\bar{\varepsilon}_{\text{HbO}_2}(\lambda_{\text{peak},j}, d) + (1-s)\bar{\varepsilon}_{\text{Hb}}(\lambda_{\text{peak},j}, d)]cd + B(\lambda_{\text{peak},j}),\end{aligned}\tag{3.15}$$

where  $\bar{\varepsilon}_{\text{HbO}_2}$  and  $\bar{\varepsilon}_{\text{Hb}}$  represent *average extinction coefficients*. The average extinction coefficients are defined so that the optical density has the same form as Eq. (3.2). It should be noted that the average extinction coefficients are a function of not only the peak wavelength, but also the diameter of the vessel. Solving Eq. (3.15) with  $s = 1$  and  $s = 0$ , we obtain:

$$\begin{aligned}\bar{\varepsilon}_{\text{HbO}_2}(\lambda_{\text{peak},j}, d) &= -\frac{1}{cd} \left( \log \left[ \frac{\int_{\Omega} d\lambda R(\lambda) S(\lambda) F_j(\lambda) \cdot 10^{-[\varepsilon_{\text{HbO}_2}(\lambda)cd+B(\lambda)]}}{\int_{\Omega} d\lambda R(\lambda) S(\lambda) F_j(\lambda)} \right] + B(\lambda_{\text{peak},j}) \right), \\ \bar{\varepsilon}_{\text{Hb}}(\lambda_{\text{peak},j}, d) &= -\frac{1}{cd} \left( \log \left[ \frac{\int_{\Omega} d\lambda R(\lambda) S(\lambda) F_j(\lambda) \cdot 10^{-[\varepsilon_{\text{Hb}}(\lambda)cd+B(\lambda)]}}{\int_{\Omega} d\lambda R(\lambda) S(\lambda) F_j(\lambda)} \right] + B(\lambda_{\text{peak},j}) \right),\end{aligned}\tag{3.16}$$

respectively. Here  $\mu_a(\lambda)$  is explicitly expressed as  $\mu_a(\lambda) = \varepsilon_{\text{HbO}_2}(\lambda)c$  and  $\mu_a(\lambda) = \varepsilon_{\text{Hb}}(\lambda)c$  for  $s = 1$  and  $s = 0$ , respectively. If light is monochromatic, i.e.  $F_j(\lambda) = \delta(\lambda - \lambda_{\text{peak},j})$  which is a Dirac delta function:

$$\begin{aligned}\bar{\varepsilon}_{\text{HbO}_2}(\lambda_{\text{peak},j}, d) &= -\frac{1}{cd} \\ &\times \left( \log \left[ \frac{\int_{\Omega} d\lambda R(\lambda) S(\lambda) \delta(\lambda - \lambda_{\text{peak},j}) \cdot 10^{-[\varepsilon_{\text{HbO}_2}(\lambda)cd+B(\lambda)]}}{\int_{\Omega} d\lambda R(\lambda) S(\lambda) \delta(\lambda - \lambda_{\text{peak},j})} \right] + B(\lambda_{\text{peak},j}) \right) \\ &= -\frac{1}{cd} \\ &\times \left( \log \left[ \frac{R(\lambda_{\text{peak},j}) S(\lambda_{\text{peak},j}) \cdot 10^{-[\varepsilon_{\text{HbO}_2}(\lambda_{\text{peak},j})cd+B(\lambda_{\text{peak},j})]}}{R(\lambda_{\text{peak},j}) S(\lambda_{\text{peak},j})} \right] + B(\lambda_{\text{peak},j}) \right) \\ &= -\frac{1}{cd} (-[\varepsilon_{\text{HbO}_2}(\lambda_{\text{peak},j})cd + B(\lambda_{\text{peak},j})] + B(\lambda_{\text{peak},j})) \\ &= \varepsilon_{\text{HbO}_2}(\lambda_{\text{peak},j})\end{aligned}\tag{3.17}$$

then Eq. (3.16) becomes  $\bar{\varepsilon}_{\text{HbO}_2}(\lambda_{\text{peak},j}) = \varepsilon_{\text{HbO}_2}(\lambda_{\text{peak},j})$  and  $\bar{\varepsilon}_{\text{Hb}}(\lambda_{\text{peak},j}) = \varepsilon_{\text{Hb}}(\lambda_{\text{peak},j})$ .

Finally, the approximation made in the above is discussed. Cohen and Laing [35] assumed that the dependences of the RBCs' scattering part of  $B(\lambda)$  and the reflectance  $R(\lambda)$  on wavelength are much smaller than variations of  $S(\lambda)$ ,  $F(\lambda)$ , and  $\mu_a(\lambda)$ , then they do not contribute at all to the integral. In addition to Cohen's approximation, variation of  $B(\lambda)$  other than RBCs' scattering is also assumed to be smaller than that of  $S(\lambda)$ ,  $F(\lambda)$ , and  $\mu_a(\lambda)$ , i.e.  $B(\lambda) \simeq B(\lambda_{\text{peak},j})$  in the wavelength range of LED used. Therefore, Eq. (3.16) can be rewritten to:

$$\begin{aligned}\bar{\varepsilon}_{\text{HbO}_2}(\lambda_{\text{peak},j}, d) &= -\frac{1}{cd} \left( \log \left[ \frac{\int_{\Omega} d\lambda S(\lambda) F_j(\lambda) 10^{-\varepsilon_{\text{HbO}_2}(\lambda)cd}}{\int_{\Omega} d\lambda S(\lambda) F_j(\lambda)} \right] \right), \\ \bar{\varepsilon}_{\text{Hb}}(\lambda_{\text{peak},j}, d) &= -\frac{1}{cd} \left( \log \left[ \frac{\int_{\Omega} d\lambda S(\lambda) F_j(\lambda) 10^{-\varepsilon_{\text{Hb}}(\lambda)cd}}{\int_{\Omega} d\lambda S(\lambda) F_j(\lambda)} \right] \right).\end{aligned}\quad (3.18)$$

In this study,  $S(\lambda)$  is assumed to set to unity and  $F(\lambda)$  is set to a Gaussian function (see Chapter 4) in order to simplify the calculation. The diameter  $d$  of a blood vessel is assumed to be consistent with the FWHM of the profile of a vessel image [59, 60]. Before estimating  $\text{SO}_2$ ,  $d$  from images is measured, and then  $\bar{\varepsilon}_{\text{HbO}_2}(\lambda_{\text{peak}}, d)$  and  $\bar{\varepsilon}_{\text{Hb}}(\lambda_{\text{peak}}, d)$  are calculated using Eq. (3.18) with known  $\varepsilon_{\text{HbO}_2}c$  and  $\varepsilon_{\text{Hb}}c$ .

### 3.5 Error sensitivity of $\text{SO}_2$ estimation method

The error sensitivity of  $\text{SO}_2$  estimation was investigated in this section. In Eq. (3.10), since  $\text{SO}_2$ ,  $s$ , is a function of transmittances  $T_1 = T(\lambda_1)$  and  $T_2 = T(\lambda_2)$ , the error of  $s$ -estimation caused by the error  $\Delta T$  of transmittances of two-wavelengths is defined by:

$$\Delta s := s(T_1 + \Delta T_1, T_2 + \Delta T_2) - s(T_1, T_2). \quad (3.19)$$

Here, estimated  $\Psi(T_1, T_2)$  in Eq. (3.10) is represented using  $\Delta T$  by:

$$\begin{aligned}\Psi_{\text{estimated}}(T_1 + \Delta T_1, T_2 + \Delta T_2) &= \frac{D(\lambda_2)}{D(\lambda_1)} = \frac{-\log(T_2 + \Delta T_2)}{-\log(T_1 + \Delta T_1)} \\ &= \frac{\log T_2 + \log(1 + \Delta T_2/T_2)}{\log T_1 + \log(1 + \Delta T_1/T_1)} \\ &= \frac{-\mu_a(\lambda_2)d + \log(1 + \Delta T_2/T_2)}{-\mu_a(\lambda_1)d + \log(1 + \Delta T_1/T_1)},\end{aligned}\quad (3.20)$$

where Lambert-Beer law is used for calculation of transmittance:  $T = 10^{-\mu_a d}$ . Figure 3.5 shows  $\Delta s$  caused by  $\Delta T_1/T_1$  and  $\Delta T_2/T_2$  for  $\lambda_1 = 470$  nm and  $\lambda_2 = 527$  nm, and  $d = 0.1$  mm using extinction coefficients at the peak wavelengths and AECs. In the case of  $\Delta T/T = 10\%$ ,  $\Delta s$  is  $\sim 2\%$  ( $s = 1$ ) and  $< 1\%$  ( $s = 0$ ) for use of extinction coefficients at the peak wavelengths and  $\sim 2\%$  ( $s = 1$ ) and  $< 1\%$  ( $s = 0$ ) for use of AECs.

### 3.6 Tissue scattering correction method using maximum slopes of SDF image

When the system has only hemoglobin absorption and scattering by RBCs, the AECs can be determined and then  $SO_2$  can be exactly estimated. In such a case, AECs are assumed to be estimated from an obtained SDF image. These estimated AECs are defined by:

$$\begin{aligned}\bar{\varepsilon}_{\text{HbO}_2}^{\text{measure}}(\lambda_{\text{peak},j}) &:= -\frac{1}{cd} \log \left[ \frac{p_{\text{out},s=1}(\lambda_{\text{peak},j})}{p_{\text{in}}(\lambda_{\text{peak},j})} \right], \\ \bar{\varepsilon}_{\text{Hb}}^{\text{measure}}(\lambda_{\text{peak},j}) &:= -\frac{1}{cd} \log \left[ \frac{p_{\text{out},s=0}(\lambda_{\text{peak},j})}{p_{\text{in}}(\lambda_{\text{peak},j})} \right],\end{aligned}\tag{3.21}$$

where  $p_{\text{in}}$  and  $p_{\text{out},s}$  represent the pixel values of a part of the background and a blood vessel with  $s$  in an SDF image, respectively.

In reality, the system includes the tissue scattering and thus it brings the estimation error. In this study, we investigated the influence of the tissue scattering. In the ideal condition that there is no influence of tissue scattering, measured extinction coefficients determined from Eq. (3.21) agrees with Eq. (3.16):  $\bar{\varepsilon}^{\text{measure}} = \bar{\varepsilon}$ . However, in Eq. (3.21), the pixel value  $p_{\text{out}}$  includes influence of the scattered light of the peripheral region around a blood vessel. Blur of a blood vessel image was observed experimentally due to the scattering by a tissue. Two causes of the blur as shown in Fig. 3.4(c) were considered. The first cause is the scattering by RBCs and tissue. Light that enters into a blood vessel spreads out due to the scattering by RBCs (A-1 in Fig. 3.4(c)). After that, the light goes through the vessel and then spreads out because of the scattering by tissue above the vessel (A-2). The second cause is the light entry from a peripheral region around a blood vessel to a detection area due to the multiple scattering by tissue (B). The influence (A-1) is included in  $B(\lambda)$ . However, our SDF oximetry concept does not include the influence of both (A-2) and (B). Thus, the model of the measured

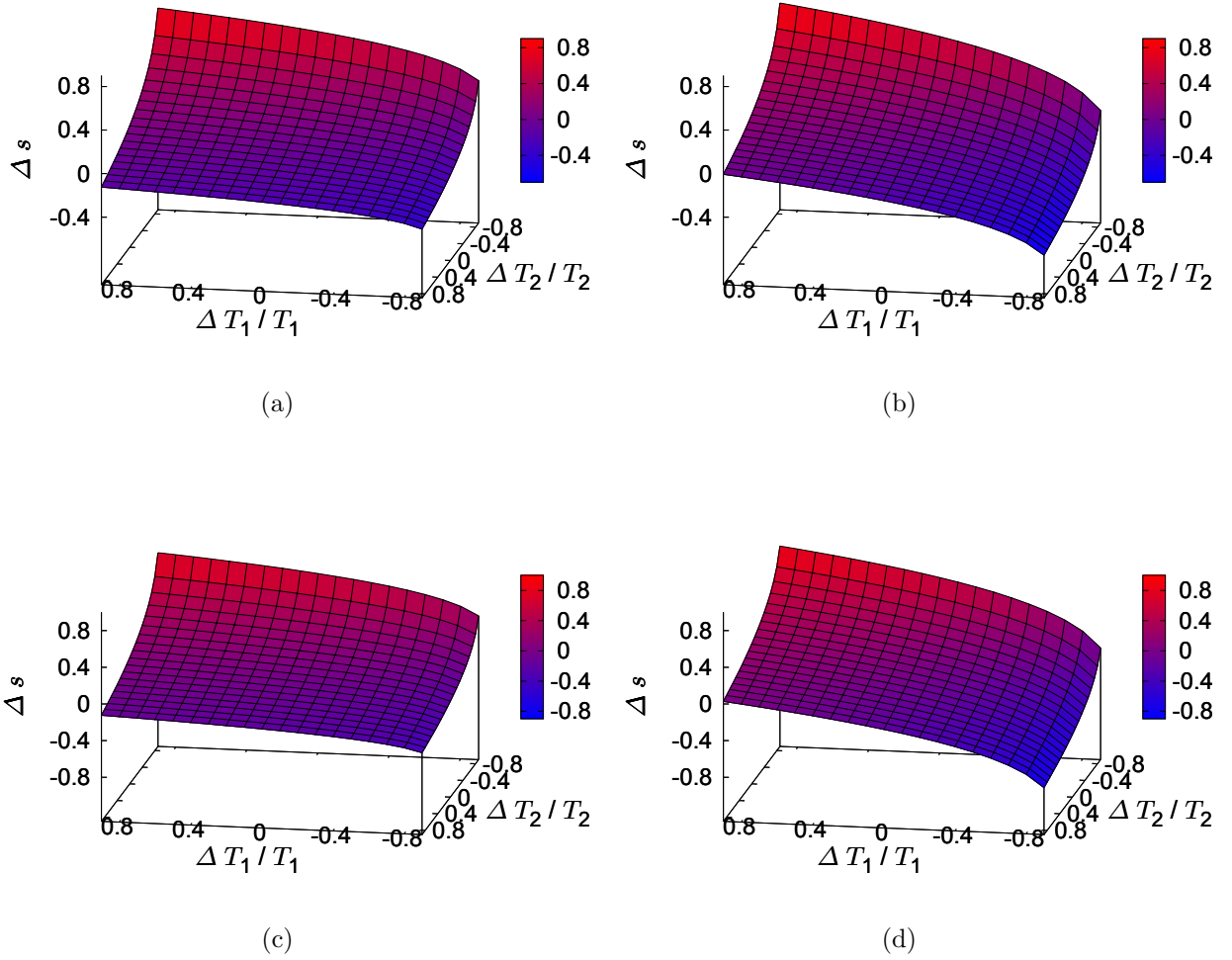


Fig 3.5:  $\text{SO}_2$  estimation error for  $\Delta T_1$  and  $\Delta T_2$  using (a and b) extinction coefficients at the peak wavelengths with (a)  $s = 0\%$  and (b)  $s = 100\%$  and (c and d) AECs of each region of 470 nm and 527 nm with (c)  $s = 0\%$  and (d)  $s = 100\%$ .

AECs was modified as a sum of theoretical value without tissue scattering and an additional term corresponding to the tissue scattering as follows:

$$\begin{aligned}\bar{\varepsilon}_{\text{HbO}_2}^{\text{measure}}(\lambda_{\text{peak},j}) &= -\frac{1}{cd} \log \left[ \frac{\bar{I}_{\text{out},s=1}(\lambda_{\text{peak},j})}{\bar{I}_{\text{in}}(\lambda_{\text{peak},j})} \right] + \xi \left( \int_{\Omega} f(\mu_s^{\text{tissue}}(\lambda), t) d\lambda \right), \\ \bar{\varepsilon}_{\text{Hb}}^{\text{measure}}(\lambda_{\text{peak},j}) &= -\frac{1}{cd} \log \left[ \frac{\bar{I}_{\text{out},s=0}(\lambda_{\text{peak},j})}{\bar{I}_{\text{in}}(\lambda_{\text{peak},j})} \right] + \xi \left( \int_{\Omega} f(\mu_s^{\text{tissue}}(\lambda), t) d\lambda \right).\end{aligned}\tag{3.22}$$

Here,  $\xi$  is an additional terms and assumed to be depends on the sum of a certain quantity  $f$  of both the tissue scattering coefficient  $\mu_s^{\text{tissue}}(\lambda)$  and blood vessel depth  $t$ . It is noted that  $\xi$  increases when  $\mu_s^{\text{tissue}}$  and  $t$  increase. The intensity of the detected light and the incident light are respectively defined by:

$$\begin{aligned}\bar{I}_{\text{out},s}(\lambda_{\text{peak},j}) &= \int_{\Omega} d\lambda S(\lambda) R(\lambda) I_{\text{p},j} F_j(\lambda) \cdot 10^{-[s\varepsilon_{\text{HbO}_2}(\lambda) + (1-s)\varepsilon_{\text{Hb}}(\lambda)]cd + B(\lambda_{\text{peak},j}) - B(\lambda)}, \\ \bar{I}_{\text{in}}(\lambda_{\text{peak},j}) &= \int_{\Omega} d\lambda S(\lambda) R(\lambda) I_{\text{p},j} F_j(\lambda).\end{aligned}\tag{3.23}$$

It is noted that  $\xi$  depends on both  $\mu_s^{\text{tissue}}(\lambda_{\text{peak},j})$  and  $t$  if  $\mu_s^{\text{tissue}}(\lambda)$  has an approximately constant value around the peak wavelength.

The modified AECs that include the influence of the tissue scattering were defined in Eq. (3.22). Here a correction method for the tissue scattering for SDF oximetry is proposed. In our method,  $\xi$  is estimated using a feature value measured from an SDF image. As a feature value, we were focus on the maximum slope of an intensity profile in the direction perpendicular to the running direction of a blood vessel. That is because blur of a blood vessel image is caused by the scattering by a tissue surrounding the blood vessel as mentioned before. An average maximum slope of both sides of an SDF image under green LED illumination is used. The peak wavelength of green LED illumination is 527 nm that is near an isosbestic point of hemoglobin. Therefore, maximum slopes are not so much dependent on the difference of the pixel value caused by the different oxygen level of blood. To estimate  $\text{SO}_2$  using the modified AECs that include the influence of the tissue scattering, the relationship between the maximum absolute slope and  $\xi$  in Eq. (3.22) must be known beforehand. In this study, using phantoms that mimic a biological tissue, the relationship between the maximum

absolute slope and the scattering coefficient of the concentration of fat emulsion used is investigated and then  $\xi$  as a function of the scattering coefficient of the phantoms was determined. Procedure of the method is as follows:

1. as preparation, determine the two relationships between the average of the maximum absolute slopes in both sides of a profile and a scattering coefficient and between the scattering coefficient and  $\xi$ , using phantoms that include scatterers of different concentration and blood-filled glass tubes,
2. when estimating the  $\text{SO}_2$ , calculate an average maximum slope from an SDF image with green illumination,
3. calculate the scattering coefficient from the average maximum absolute slope,
4. determine  $\xi$  from the scattering coefficient,
5. estimate  $\text{SO}_2$  using the AECs that include  $\xi$ .

In this study,  $\text{SO}_2$  estimation using the above method with the phantoms was performed to confirm the validity for the proposed correction method.

# Chapter 4 PHOTON PROPAGATION SIMULATION

Photon propagation simulation is useful for understanding behavior of light within tissues. As a simulation technique, there are the radiative transfer equation (RTE) and the Monte Carlo technique [62]. The Monte Carlo technique has advantages compared to RTE. The advantages are that both boundary conditions for a differential equation and assumption of an infinite thickness of a medium are unnecessary. However, the Monte Carlo technique requires a long time to calculate behavior of many photons. Though a calculation time is long, in order to simulate the behavior of photons in biological tissues, this technique has been used often. In this chapter, the Monte Carlo technique for photon propagation simulation is introduced, and results of the investigation to validate the SDF oximetry are shown. In § 4.1, the algorithm of the Monte Carlo photon propagation simulation, the simulation of LED sources and results of the test are shown. In § 4.2 and § 4.3, we investigated the validity of SDF oximetry and the tissue scattering correction method.

## 4.1 Monte Carlo photon propagation simulation

Algorithms of the Monte Carlo photon propagation simulation have been suggested in many studies [63–65]. This technique simulates interactions with a medium. The interactions are absorption, scattering, and reflection. They are simulated using pseudo-random numbers and many photons. In this study, *mesh-based Monte Carlo* (MMC) [66, 67] was used as a code. This is a three-dimensional Monte Carlo code using a three-dimensional mesh model. The mesh model is produced by dividing a medium with tetrahedrons. The algorithm of the code

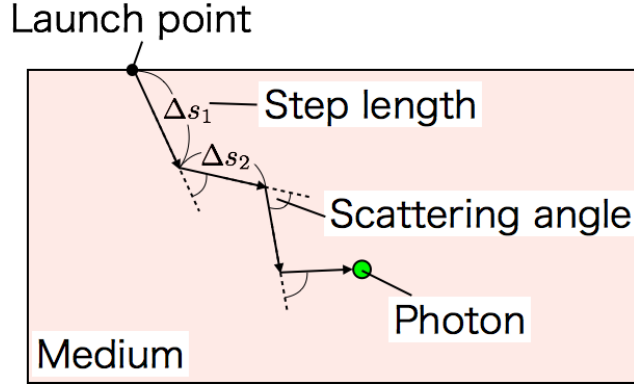


Fig 4.1: Schematic view of the photon propagation in a medium.

is introduced in this section.

#### 4.1.1 Algorithm

In the Monte Carlo simulation, as parameters prepared, the structure of optically distinct regions included in a medium and the information of incident photons such as the total number, launch points, and initial incident direction. As optical parameters of these regions, an absorption coefficient  $\mu_a$ , a scattering coefficient  $\mu_s$ , an anisotropy factor  $g$ , and a refractive index  $n$  of each region composing the medium are given.

##### Step length

In the simulation, the calculations of phenomena are performed every step as shown in Fig. 4.1. The step length of a photon is calculated using a pseudo random number  $\eta$  ranging from 0 to 1:

$$\Delta s = -\frac{\ln \eta}{\mu_a + \mu_s}. \quad (4.1)$$

$1/(\mu_a + \mu_s)$  is a mean free path that means the length until the next event (absorption or scattering) occurs.



## Absorption

Absorption of photons is calculated using the Lambert-Beer law with  $\mu_s$ . In the technique, concept of a packet of photons is considered rather than a photon. Absorption of photons is approximately calculated regarded as the attenuation of packets of photons in a medium.

To calculate the absorption, a weight function is defined as intensity of light. Let us consider a medium containing a uniform absorber with  $\mu_a$ . The weight function  $W$  after a step with the step length  $\Delta s$  from the launch point with the initial weight  $W_0$  is given by:

$$W_1 = W_0 \exp[-\mu_a \Delta s]. \quad (4.2)$$

After  $i$ -th steps with  $\Delta s_i$ , its weight is determined using  $(i-1)$ -th weight  $W_{i-1}$ :

$$W_i = W_{i-1} \exp[-\mu_a \Delta s_i]. \quad (4.3)$$

Thus,  $W_i$  can be calculated sequentially from  $W_0$ :

$$\begin{aligned} W_i &= W_{i-1} \exp(-\mu_a \Delta s_i) \\ &= \{W_{i-2} \exp(-\mu_a \Delta s_{i-1})\} \cdot \exp(-\mu_a \Delta s_i) \\ &\vdots \\ &= W_0 \prod_{k=1}^i \exp(-\mu_a \Delta s_k). \end{aligned} \quad (4.4)$$

A medium comprising  $n$  regions includes the respective absorbers with  $\mu_a^{(1)}, \mu_a^{(2)}, \dots, \mu_a^{(n)}$ . In the case of passing through each region in a step  $\Delta s = \Delta s^{(1)} = \Delta s^{(2)} = \dots = \Delta s^{(n)}$ , the weight after  $n$  steps is determined by:

$$W_n = W_0 \exp[-\mu_a^{(1)} \Delta s] \cdot \exp[-\mu_a^{(2)} \Delta s] \cdots \exp[-\mu_a^{(n)} \Delta s]. \quad (4.5)$$

## Scattering

In the scattering event in a three-dimensional medium, a scattering direction determined with two scattering angles to the traveling direction are calculated as shown in Fig. 4.2(a).

The polar angle  $\theta$  to the traveling direction is determined using the Henyey-Greenstein function [68] as the probability distribution function:

$$\langle \cos \theta \rangle = 2\pi \int_{-1}^1 d \cos \theta \cos \theta p(\cos \theta), \quad (4.6)$$

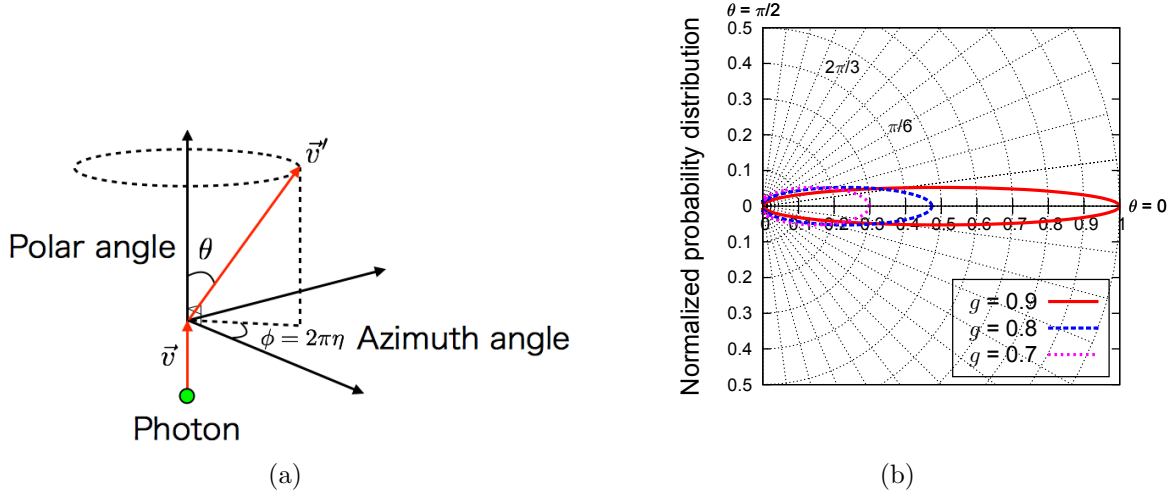


Fig 4.2: The scattering in the Monte Carlo simulation. (a) The scattering direction is determined with two angles,  $\theta$  and  $\phi$ . (b) The Henyey-Greenstein function with  $g = 0.7, 0.8$ , and  $0.9$ . This describes the probability for each scattering angle. The graph is normalized by the value for  $g = 0.9$  and  $\theta = 0$ .

where the Henyey-Greenstein function as the probability distribution is used:

$$p(\cos \theta) = \frac{1 - g^2}{2(1 + g^2 - 2g \cos \theta)^{3/2}}. \quad (4.7)$$

The Henyey-Greenstein function describes the forward or back scattering with the only parameter  $g$  as the probability density of the cosine of scattering angles. Figure 4.2(b) shows the probability for each scattering angle with  $g = 0.7, 0.8$ , and  $0.9$ . In this simulation,  $\theta$  is determined using an isotropy factor  $g$  ( $-1 \leq g \leq 1$ ) and a random number  $\eta$  by:

$$\cos \theta = \begin{cases} \frac{1}{2g} \left\{ 1 + g^2 - \left[ \frac{1-g^2}{1-g+2g\eta} \right]^2 \right\} & , \text{for } g > 0, \\ \pi\eta & , \text{for } g = 0. \end{cases} \quad (4.8)$$

An azimuth angle  $\phi$  is calculated using a random number  $\eta$  ranging from 0 to 1:

$$\phi = 2\pi\eta. \quad (4.9)$$

Using the angles of the above-mentioned, the scattering direction  $\vec{v}' = (v'_x, v'_y, v'_z)$  from the position of the scattering occurs is given by:

$$v'_x = \frac{\sin \theta}{\sqrt{1 - v_z^2}} (v_x v_z \cos \phi - v_y \sin \phi) + v_x \cos \theta,$$

$$\begin{aligned}
v'_y &= \frac{\sin \theta}{\sqrt{1 - v_z^2}} (v_y v_z \cos \phi + v_x \sin \phi) + v_y \cos \theta, \\
v'_z &= -\sqrt{1 - v_z^2} \sin \theta \cos \phi + v_z \cos \theta.
\end{aligned} \tag{4.10}$$

Thus, the new direction of photon propagation is given by:

$$\vec{v} + \Delta s \vec{v}'. \tag{4.11}$$

## Reflection

Reflection occurs at a boundary of both regions and both the inside and outside of a medium. In the reflection event, the code determines whether a photon is reflected at the boundary and its reflectance when the photon is reflected. Reflectance on a boundary of two regions with a refractive index  $n_1$  and  $n_2$  is calculated using equations of Fresnel's formulas:

$$\begin{aligned}
R_s &= \left| \frac{n_1 \cos \theta_1 - n_2 \cos \theta_2}{n_1 \cos \theta_1 + n_2 \cos \theta_2} \right|^2, \\
R_p &= \left| \frac{n_2 \cos \theta_1 - n_1 \cos \theta_2}{n_1 \cos \theta_1 + n_2 \cos \theta_2} \right|^2,
\end{aligned} \tag{4.12}$$

where  $n_i$  is a refractive index of  $i$ -th region,  $\theta_i$  is an incident or a refractive angle. Reflectance is determined by:

$$R = \frac{R_s + R_p}{2}. \tag{4.13}$$

Reflection occurs at the boundary when the following condition is satisfied:

- if  $\eta \leq R$ , then photons are reflected at the boundary,
- if  $\eta > R$ , then photons are transmitted through the boundary,

where  $\eta$  is a pseudo-random number ranging from 0 to 1.

## Convergence condition of tracing a photon

If a photon is absorbed by a medium or exits outside the medium, tracing a photon is terminated in the code. In the case of the absorption, the threshold value  $W_{\text{th}}$  of the weight

function is set. If a weight falls below  $W_{\text{th}}$ , photon tracing is determined at the end of it as the absorption by the medium. This determination is called Russian roulette [63]. This is expressed by:

$$W = \begin{cases} mW, & \text{if } \eta \leq 1/m \\ 0, & \text{if } \eta > 1/m \end{cases} \quad (4.14)$$

where  $m$  is a fixed constant and  $\eta$  is a uniform pseudo-random number. In this study,  $m$  was set to 5.

#### 4.1.2 Simulating LED light sources

As an illumination source, LED chips were used in our SDF probe. The LED chip has the radiating area and the distribution of the directivity. The original code, however, assumes the use of a point source and emits a photon in a given incident direction. We simulated the radiating area, directivity, and spectral characteristics of an LED chip. These are non-negligible factors because the target is very small compared to the illumination source.

The area illumination source is assumed as a set of point sources. Figure 4.3 shows the geometry of area illumination sources (launch points) in the case of our SDF probe. In the area of the illumination source,  $N$  points are set as photon launch points. A photon is emitted from the point determined at random from among  $N$  points with the uniform probability distribution,  $1/N$ .

An LED chip does not radiate light straightly as compared such as the laser. Figure 4.4 shows the directivity of the LED used in our SDF probe. We assumed the light spreads widely from the LED chip. To simulate the directivity of an LED chip, we determine the direction of an incident photon using a random number. The polar angle is determined with the normal distribution and the azimuth angle is calculated using Eq. (4.9).

We assumed that the spectral intensity distribution of a LED with a peak wavelength  $\lambda_{\text{peak}}$  has a Gaussian function given by:

$$F(\lambda) = C \exp \left[ -\frac{(\lambda - \lambda_{\text{peak}})^2}{2\sigma^2} \right], \quad (4.15)$$

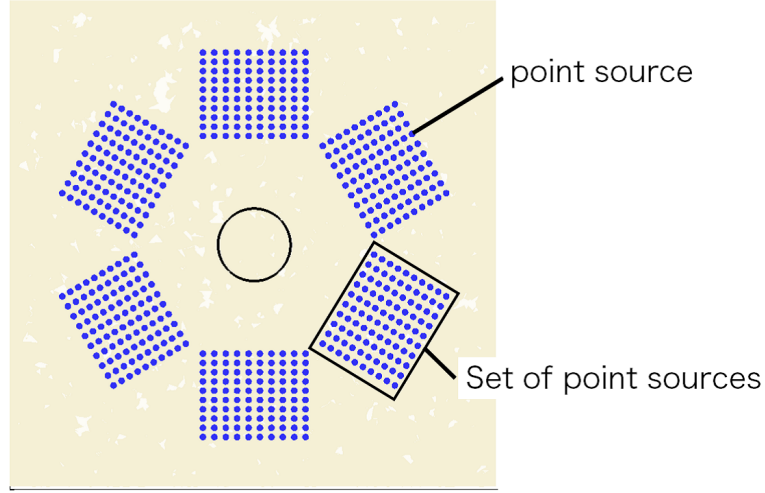


Fig 4.3: Area illumination sources. These sources simulated by collecting point light sources.

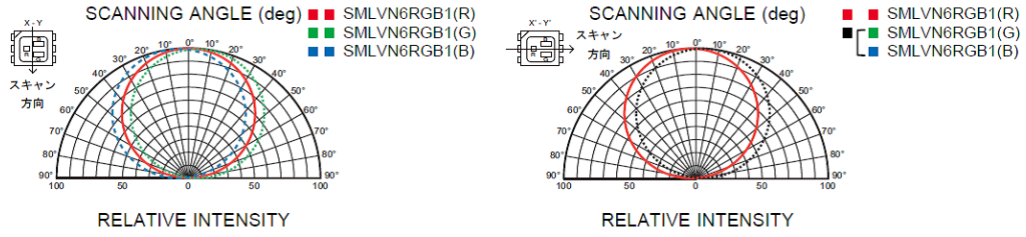


Fig 4.4: The directivity of the LED chip (SMLVN6RGB1W, ROHM Co., Ltd., Kyoto, Japan) in the data sheet described by the manufacturer [69].

where  $C$  is the normalization coefficient and  $\sigma$  is the coefficient to control the bandwidth. The distribution of an incident photon is determined by:

$$N(\lambda) = N_{\text{total}} \cdot F(\lambda), \quad (4.16)$$

where  $N_{\text{total}}$  is the total number of photons. Table 4.1 shows the distribution of the number of photons used in this study. We set bandwidth  $w$  as the FWHM of the Gaussian function, namely:

$$\sigma = \sqrt{\frac{w^2}{8 \ln 2}}. \quad (4.17)$$

For  $w = 30$  nm,  $\sigma$  is 12.74 nm.

Table 4.1: The distribution of the total incident photon.

			Number of photons $N(\lambda)$		
$\lambda$ [nm]			Total number $N_{\text{total}}$		
Blue	Green	Ratio of the peak	$1.0 \times 10^6$	$2.0 \times 10^7$	$1.0 \times 10^8$
420	477	0.00045209	141	2831	14157
430	487	0.00723340	2265	45302	226512
440	497	0.06250000	19571	391436	1957180
450	507	0.29163226	91324	1826485	9132429
460	517	0.73486725	230122	4602456	23012280
470	527 (peak)	1.00000000	313148	6262976	31314880
480	537	0.73486725	230122	4602456	23012280
490	547	0.29163226	91324	1826485	9132429
500	557	0.06250000	19571	391436	1957180
510	567	0.00723340	2265	45302	226512
520	577	0.00045209	141	2831	14157

### 4.1.3 Test of the simulation

Tests of the Monte Carlo simulation were performed using a simple model with uniform optical properties. To visualize the propagation of photons, we focus on the distribution of the fluence of photons. In this code, fluence is defined by the weight accumulated in an element that constitute a mesh model of a medium.

First of all, we confirmed that area illumination sources could be reproduced using a transparent media. The size of the model was  $13.5 \times 13.5 \times 50.0 \text{ mm}^3$ . The total number of photons was  $1.0 \times 10^6$  and optical properties were set to  $\mu_a = 0.01 \text{ mm}^{-1}$ ,  $\mu_s = 0.01 \text{ mm}^{-1}$ , and  $g = 0.9$ . Figure 4.5 shows the model with area illuminations and the distribution of the fluence in the cross section. The fluence was normalized by the maximum value in this cross section. As shown in Fig. 4.5(b), photons were linearly propagated since  $\mu_s$  was very small. The location of the maximum value was at depth of about 4.5 mm. This was near the light collecting location as mentioned in Chapter 2. Figure 4.6 show the top view of the distribution of the fluence at 0.0 mm, 1.0 mm, 2.5 mm, and 25 mm of depth from the top surface. From the

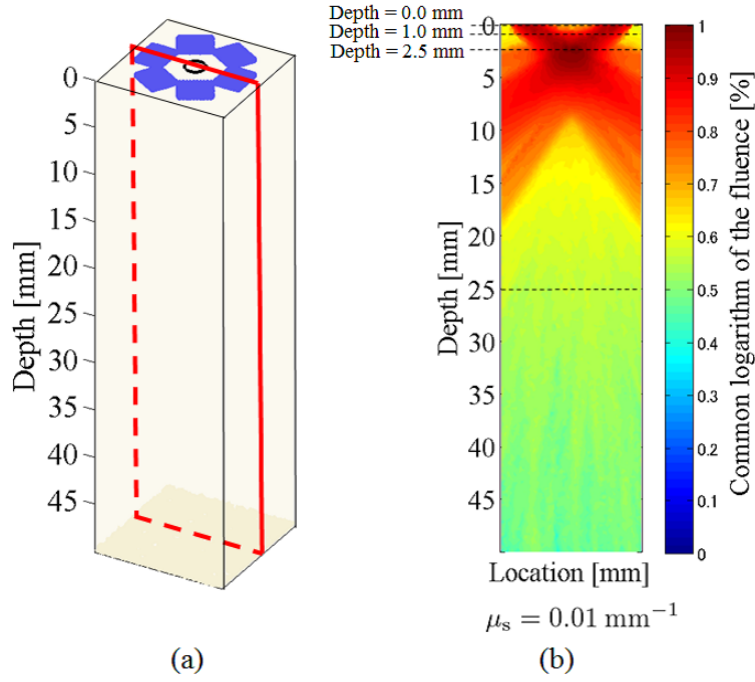


Fig 4.5: The simple model. (a) Overview of the model. The red line represents the cross section. (b) The distribution of the fluence in the cross section represented in (a).

result of a 0.0 mm depth, we could confirm that area illumination sources were created and have a distribution of irradiation direction like a cone beam as with actual light illumination sources. We found that photons converged on the center with increment of the depth until the light collecting location.

Next, results of the influence of the scattering on the simple model are shown in Figs. 4.7 and 4.8. The simulation was performed with  $\mu_a = 0.01 \text{ mm}^{-1}$  and  $g = 0.9$ . The scattering coefficient was set to  $\mu_s = 10 \text{ mm}^{-1}$ ,  $20 \text{ mm}^{-1}$ , and  $30 \text{ mm}^{-1}$ . Figure 4.7 shows the distribution of the fluence in the cross section of the side. We found that photons did not penetrate the deeper region with increment of  $\mu_s$ . Figure 4.8 shows the top view of the distribution of the fluence. In the case of the high-scattering medium, we found that the spread of photons was spherical (diffuse approximation [70]).

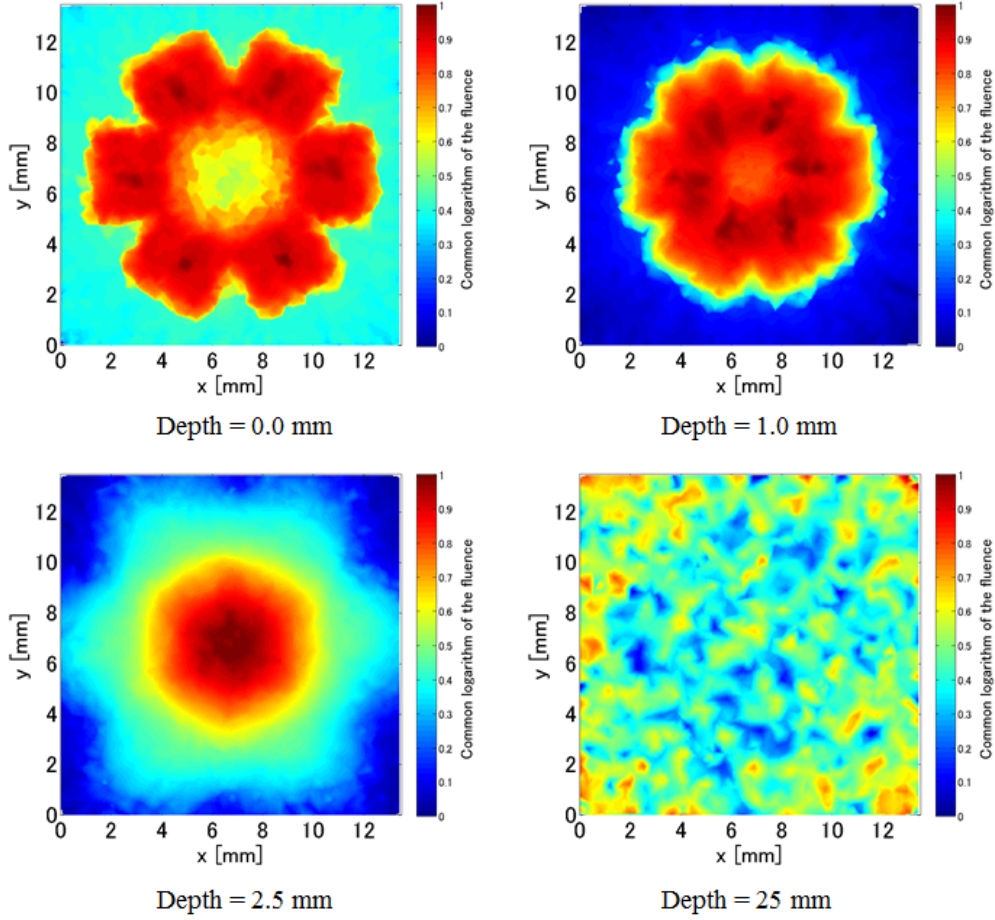


Fig 4.6: The top view of the distribution of the fluence. From the upper left hand side, the result shows the distribution of the fluence in a 0.0 mm, 1.0 mm, 2.5 mm, and 25 mm.

## 4.2 Evaluation of the feasibility of SDF oximetry

We performed the Monte Carlo photon propagation simulation to evaluate the  $\text{SO}_2$  estimation method. As a basic study, we investigated the trend of the estimated  $\text{SO}_2$  by changing values of  $\text{SO}_2$ , vessel diameter, and bandwidth of illumination sources. Our procedure was as follows: first, we made a tissue model with a blood vessel and set blood with known  $\text{SO}_2$  into the vessel. Next, we simulated the photon propagation in the tissue and acquired virtual SDF images. Finally, we estimated  $\text{SO}_2$  from the virtual SDF images.



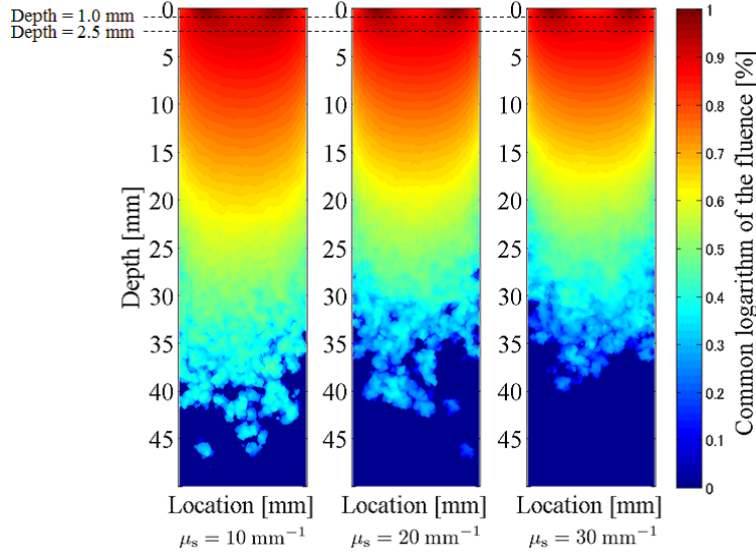


Fig 4.7: The distribution of the fluence in the cross section in the simple model with  $\mu_s = 10 \text{ mm}^{-1}$ ,  $20 \text{ mm}^{-1}$ , and  $30 \text{ mm}^{-1}$ .

#### 4.2.1 Digital tissue model

To construct a three-dimensional tissue model with a vessel, we used an open-source software *iso2mesh* [71, 72] which is coded with Matlab (MathWorks, Natick, USA). The tissue model is constructed by referring to the result of hematoxylin and eosin (H&E) staining of a pig small intestine shown in Fig. 4.9(a). The simulated tissue model is shown in Figs. 4.9(b) and 4.9(c). As shown in Fig. 4.9(d), each of the layers simulate serosa, muscularis, submucosa, and mucosa from the top surface respectively. The size of the model was 11.5 mm (width)  $\times$  11.5 mm (depth)  $\times$  2 mm (height). Here the model has a blood vessel whose uppermost surface is located at 100  $\mu\text{m}$  below the top surface in the serosa. We set the blood vessel diameter as 100, 200, and 300  $\mu\text{m}$ .

In this study, the optical properties of the blood vessel and blood were approximated by those of hemoglobin. The oxygen saturation was varied by the amount of the oxygenated hemoglobin. We used these optical properties in the case of the hematocrit value  $H = 0.4$  reported in the literature [10, 73]. The optical properties of blood are shown in Fig. 4.10(a) and in detail in Appendix B. In the optical properties of tissue, we assumed that absorption and scattering of each layer were homogeneous. The absorption coefficient of each layer other than the serosa was equal and the oxygen saturation of tissue was fixed. We used the value

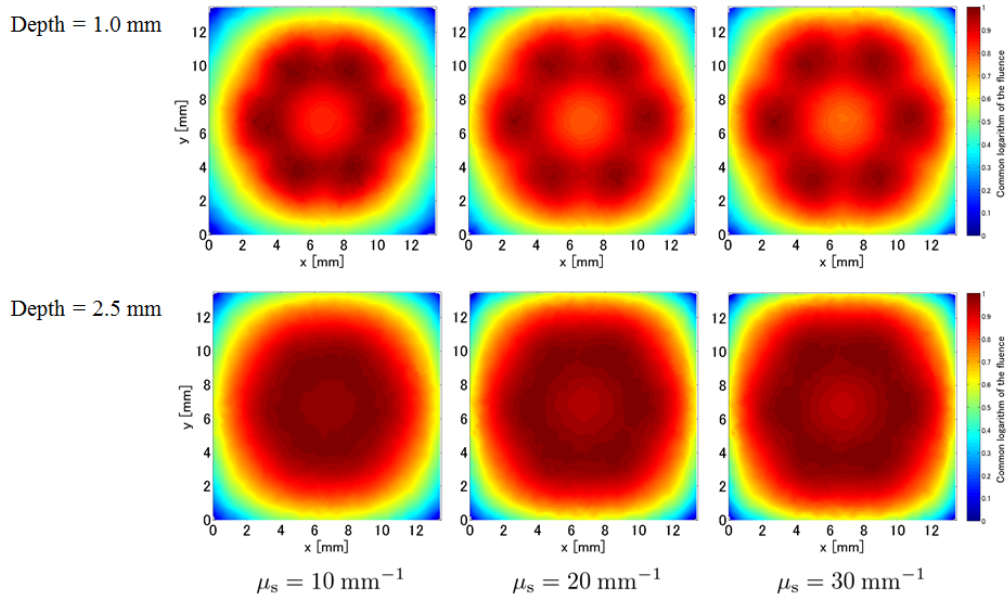


Fig 4.8: The top view of the distribution of the fluence in the simple model with  $\mu_s = 10 \text{ mm}^{-1}$ ,  $20 \text{ mm}^{-1}$ , and  $30 \text{ mm}^{-1}$ . From the upper rows, the result shows the distribution of the fluence in a 0.0 mm and 2.5 mm from the left hand side.

of mucosa in the study by Bashkatov *et al.* [74] as the absorption coefficient of tissue. The scattering coefficient is in proportion to the volume fraction of scatterer in a medium [75]. Accordingly, we assume that the size of scatterer in each layer was equal. Since the submucosa includes an abundant number of blood vessels and tends to scatter the light, the ratio of the volume fraction of scatterer to that of the submucosa was set as 0.7 in the mucosa and 0.3 in the muscularis. The scattering coefficient of the submucosa was set to the value shown in the literature by Bashkatov *et al.* [74]. Absorption coefficient and scattering coefficient of the submucosa are shown in Fig. 4.10(b). Table 4.2 shows the values of optical properties of the tissue model used in this simulation. For the serosa, we set this layer as transparent, i.e.  $\mu_a = 0 \text{ mm}^{-1}$  and  $\mu_s = 0 \text{ mm}^{-1}$ . The anisotropy factor of tissue was set as 0.9. This is because this value is approximately equal for any tissue.

#### 4.2.2 Trial SDF device

The illumination geometry was similar to that in the SDF imaging device that we have developed as shown in Chapter 2. Figure 4.9(d) shows the geometry of the simulation. A

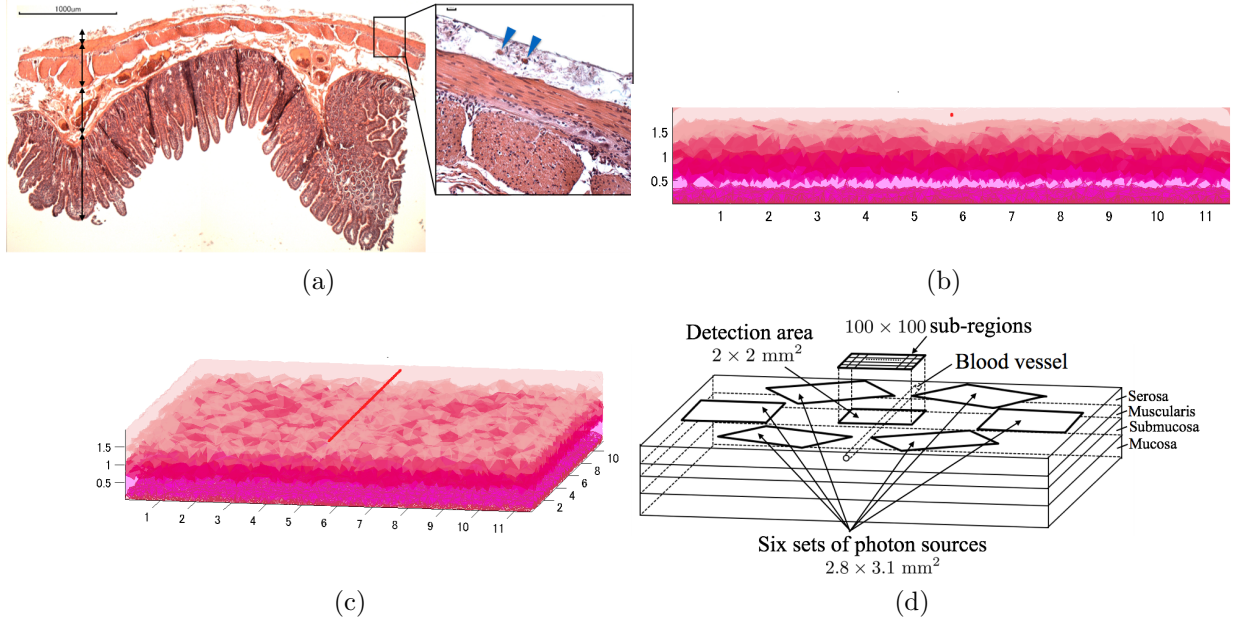


Fig 4.9: The tissue model. (a) The cross section of a small intestine of a pig H&E stained. The layers, from the top surface, serosa, muscularis, submucosa, and mucosa. The inset on the right is an enlarged image that shows blood vessels are present in the serosa (blue arrows). (b) (c) The simulated tissue model which has a layered structure and a straight blood vessel at 0.1 mm below the top surface in the serosa. (b) Side view. (c) Overview. (d) A schematic diagram of the tissue model and the geometry of the simulation.

LED chip source was assumed as a set of point sources. The initial incident angle was  $16^\circ$ . In this simulation study, the number of point sources per LED chip was 100. We set the initial launch area to be the same as that of a LED chip of the trial device. The area of a LED chip was  $2.8 \times 3.1 \text{ mm}^2$ .

As setups for the simulation, we set the number of incident photons as  $2.0 \times 10^7$  per LED chip. The photon detecting area was divided into sub-regions. The number of a sub-regions was  $100 \times 100$  and the area of a sub-region was  $0.02 \times 0.02 \text{ mm}^2$ . We assumed that a virtual SDF image acquired by a CCD camera was the spatial intensity distribution of the average weight of photons detected in each sub-region.

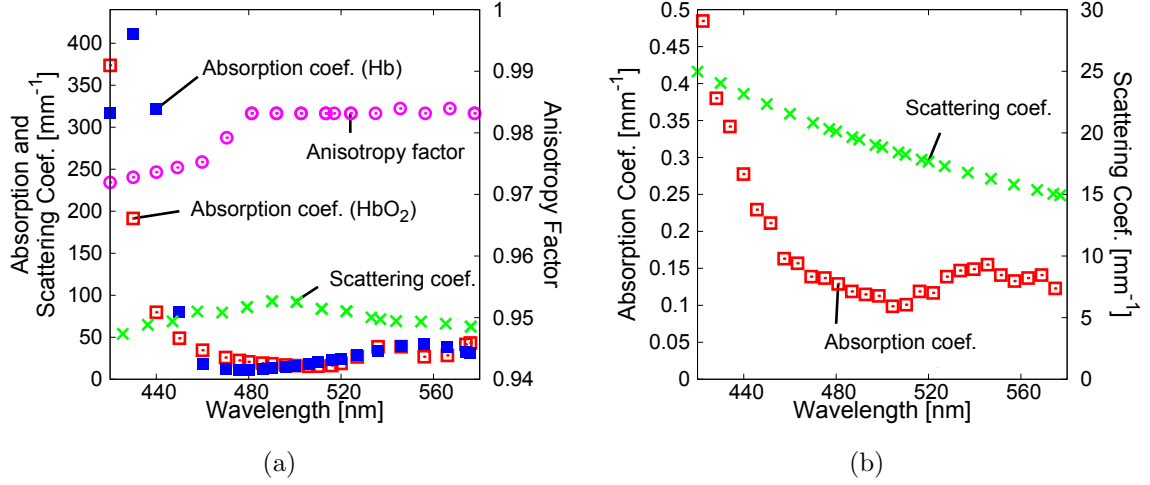


Fig 4.10: Optical properties used in this study. (a) Optical properties of blood [10, 73]. Open and closed squares represent the absorption coefficient of oxygenated and de-oxygenated hemoglobin respectively, crosses represent the scattering coefficient, and circles represents the anisotropy factor. (b) Optical properties of the tissue [74]. Squares represent the absorption coefficient and crosses represent the scattering coefficient.

### 4.2.3 Results

#### Virtual SDF images

Figure 4.11(a) shows a virtual SDF image simulated for the light at 470 nm with bandwidth  $w = 0$  and the oxygenated blood vessel with diameter  $d = 100 \mu\text{m}$ . The straight vessel in the image can be found as a dark region. Figure 4.11(b) shows the  $x$ -directional intensity profiles of the single pass, double pass, and never pass photons for the case of Fig. 4.11(a); there profiles were obtained by averaging the two-dimensional distribution along the  $y$ -direction. This result indicates that the double pass photons did not contribute to the virtual SDF image unlike for the single pass light. Moreover, in the blood vessel part, never pass photons also contribute sufficiently to the measured transmitted light intensity from the image. We measured the FWHM of the profiles from virtual SDF images, and then evaluated average extinction coefficients using Eq. (3.18). Figure 4.11(c) shows the resultant average extinction coefficients. Figure 4.11(d) shows the relation of intensities between incident and transmitted light for  $d = 100 \mu\text{m}$ . We used the weighted average of these intensities to evaluate the

Table 4.2: Optical properties of the tissue model.

$\lambda$ [nm]	$\mu_a$ [mm <sup>-1</sup> ]	$\mu_s$ [mm <sup>-1</sup> ]		
		Submucosa	Muscularis	Mucosa
420	0.4846	24.97280197	6.243200492	18.72960147
430	0.3801	24.03876908	6.009692271	18.02907681
440	0.2776	23.15995908	5.789989771	17.36996931
450	0.2113	22.33196052	5.58299013	16.74897039
460	0.1631	21.55080198	5.387700495	16.16310148
470	0.1389	20.81289982	5.203224955	15.60967487
480	0.1289	20.11501307	5.028753268	15.0862598
490	0.1148	19.45420438	4.863551094	14.59065328
500	0.1128	18.82780608	4.706951521	14.12085456
510	0.1008	18.23339072	4.558347679	13.67504304
520	0.1168	17.66874517	4.417186291	13.25155887

Lambert-Beer law below.

### Three SO<sub>2</sub> estimation methods and mean SO<sub>2</sub> estimation error

We estimated SO<sub>2</sub> using three methods: the first one was the Lambert-Beer law using weighted average values of the intensities of the incident and transmitted light of the blood vessel (Fig. 4.11(d)), which is called *the pure Lambert-Beer law method* (PLB); the second one was the image-based measurement with the extinction coefficients at the peak wavelength, which is called a method *using the extinction coefficients at the peak wavelength* (EPW); the third one was the image-based measurement with the average extinction coefficients defined in Eq. (3.18), which is called a method *using the average extinction coefficients* (AEC).

Before performing SO<sub>2</sub> estimation, we investigated dispersion of estimated values due to the number of incident photons. The number of incident photons was set to  $1.0 \times 10^7$ ,  $2.0 \times 10^7$ ,  $4.0 \times 10^7$ , or  $8.0 \times 10^7$ . We could not obtain virtual SDF images with the incident photons of  $1.0 \times 10^6$  or less since there were few photons to reach the top surface for this model. The numerical model was set to a blood vessel of a 100  $\mu\text{m}$  diameter and  $s = 100\%$ . Figure 4.12

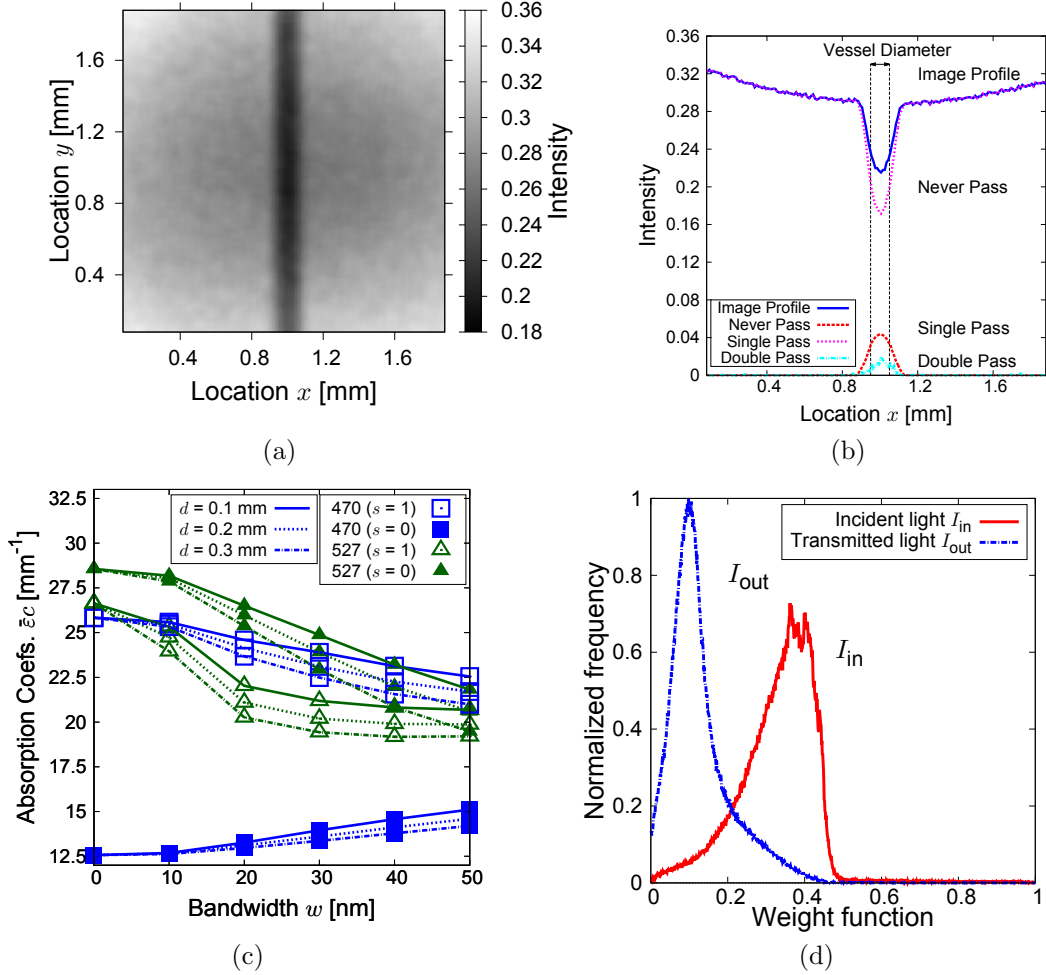


Fig 4.11: Results of the photon propagation simulation for a tissue model with the straight vessel. (a) The virtual SDF image (the gray level map of the intensity). (b) The profile of the virtual SDF image (blue line). The single pass, the double pass, and the no pass are depicted by red, magenta, and green, respectively. (c) Absorption coefficients with average extinction coefficients are plotted as a function of bandwidth of the illumination.  $\bar{\epsilon}(\lambda_0)$  for  $\lambda_0 = 470$  nm and  $527$  nm are depicted by squares and triangles, respectively. Open and closed symbols represent  $\text{SO}_2$   $s = 1$  and  $s = 0$ , respectively. Diameter  $d$  values of  $100 \mu\text{m}$ ,  $200 \mu\text{m}$ , and  $300 \mu\text{m}$  are depicted by solid lines, dashed lines, and chain lines, respectively. (d) The histogram of the intensity  $I_{in}$  of light directly entering into the blood vessel and  $I_{out}$  of light passing through it when the model is (a).

shows the result of estimated values with changing the number of incident photons. We found decrease of dispersion with increase of the number of photons. However, we must consider the calculation time using a computer with Intel Core i7-3930K processor (3.20 GHz, 6 cores), 64.0 GB of RAM, and NVIDIA GeForce GTX 680 GPU. The calculation time for performing a SO<sub>2</sub> estimation i.e. obtaining two-band images is shown in Fig 4.12(c). In the case of  $8.0 \times 10^7$  photons, the time was about 40 hours. Based on the above, in this study, we used the curve fitting approximation to obtain correspondence between estimated and true values.

We used the SO<sub>2</sub> estimation error (SEE) as an evaluation index of estimation accuracy. We modeled the estimated saturation  $s$  by a linear function to parameterize those trends:

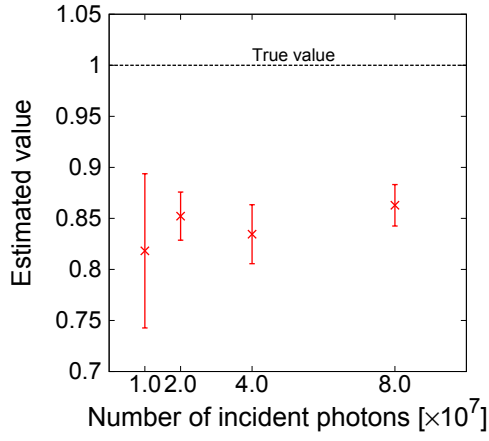
$$s = \alpha t + \beta, \quad (4.18)$$

where  $t$  ( $0 \leq t \leq 1$ ) represents the true SO<sub>2</sub> value and  $\alpha$  and  $\beta$  are fitting coefficients. Those coefficients are obtained by the Levenberg-Marquadt method. If these coefficients are close to  $\alpha = 1$  and  $\beta = 0$ , the estimation is accurate. When the SEE  $\Delta s(t)$  is defined as an absolute value of the difference between the estimated curve Eq. (4.18) and the true curve  $s = t$ , we define the mean SEE  $\overline{\Delta s}$  as:

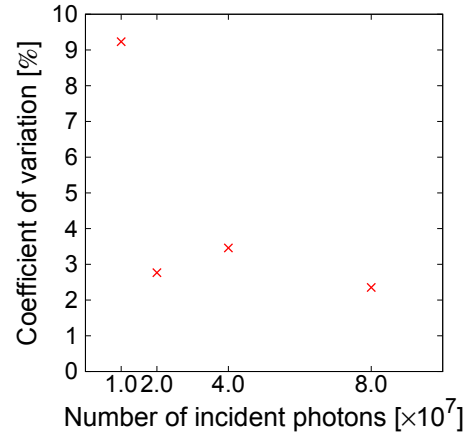
$$\overline{\Delta s} := \frac{1}{M} \sum_{i=1}^M \Delta s(t_i) = \frac{1}{M} \sum_{i=1}^M |(\alpha - 1)t_i + \beta|, \quad (4.19)$$

where  $M$  represents the number of sample points over the SO<sub>2</sub> range and  $t_i$  represents the true SO<sub>2</sub> value at the  $i$ -th sample point. In this study, we had 21 true SO<sub>2</sub> values, that is,  $M = 21$ . Figures 4.13, 4.14 and 4.15 show the results of the estimated value  $s$  and the estimated curve by Eq. (4.18) for  $d = 100 \mu\text{m}$ ,  $200 \mu\text{m}$ , and  $300 \mu\text{m}$ , respectively. Three methods (PLB, EPW, and AEC) are shown together. We show the  $\overline{\Delta s}$  and standard deviation (SD) of each measurement in Table 4.3 and summarize the  $\overline{\Delta s}$  of these results in Fig. 4.16. In Fig. 4.16, the plots are fitted by a surface with bivariate  $d$  and  $w$  power series up to the second-order of both variables. Since extinction coefficients at the peak wavelength and average extinction coefficients match in  $w = 0$ ,  $\overline{\Delta s}$  of EPW and AEC are equal. As a result, the tendency of the SEE of PLB (Fig. 4.16(a)) and AEC (Fig. 4.16(c)) are similar.

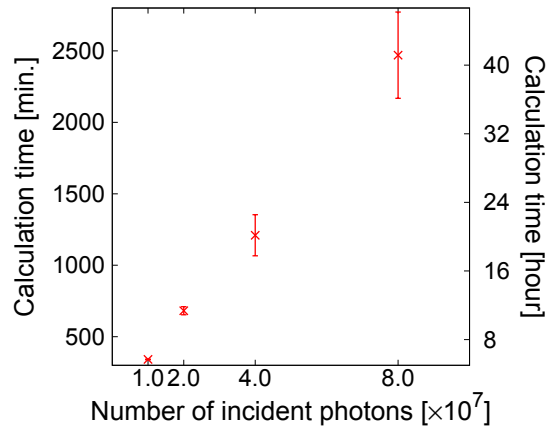
We focused on the changes in  $\overline{\Delta s}$  due to  $w$ . In the comparison between image-based methods, AEC is more accurate than EPW for all bandwidths in each  $d$ . As shown in Fig. 4.16(b) and Table 4.3,  $\overline{\Delta s}$  using EPW increases with increment of  $w$ . The changing rate of  $\overline{\Delta s}$  due to



(a)



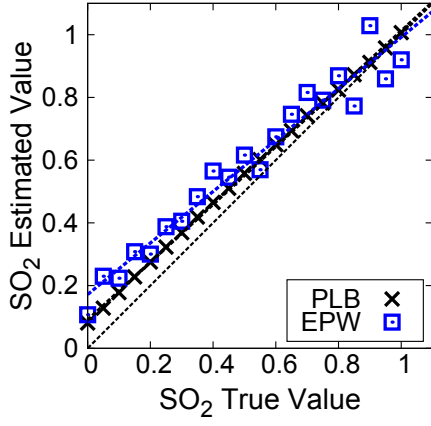
(b)



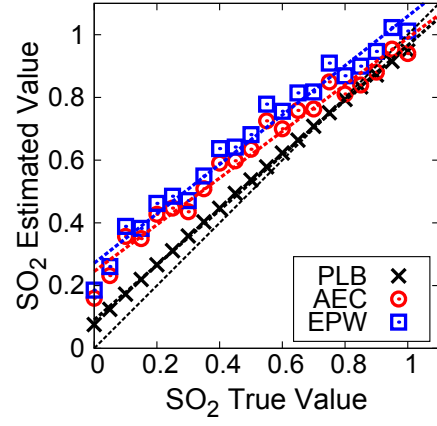
(c)

Fig 4.12: Dispersion of estimated values due to the number of incident photons. (a) Estimated values. (b) Coefficients of variation. (c) Calculation time for performing an  $\text{SO}_2$  estimation.

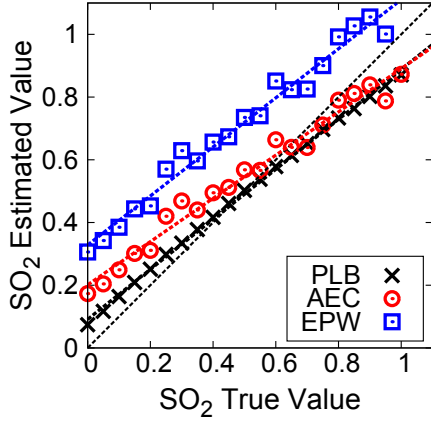




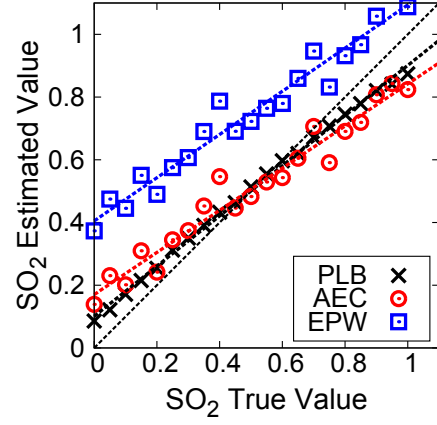
(a)



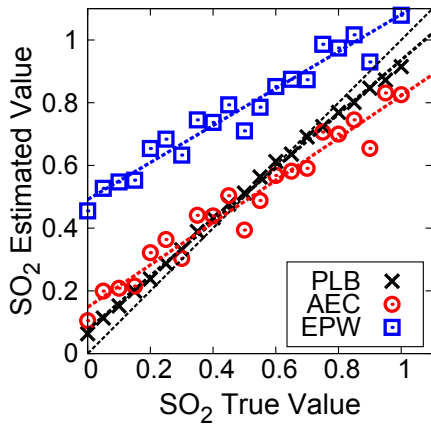
(b)



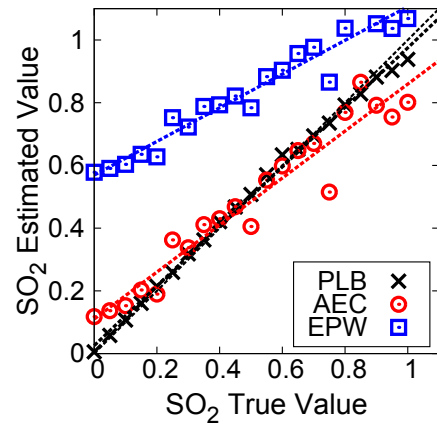
(c)



(d)

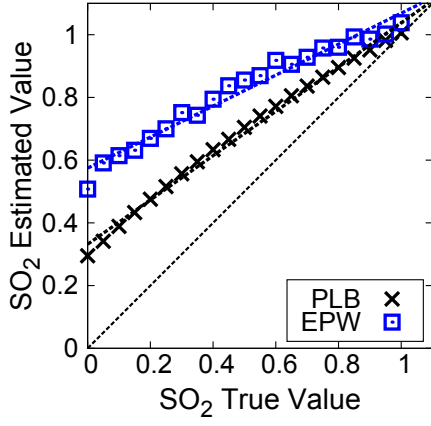


(e)

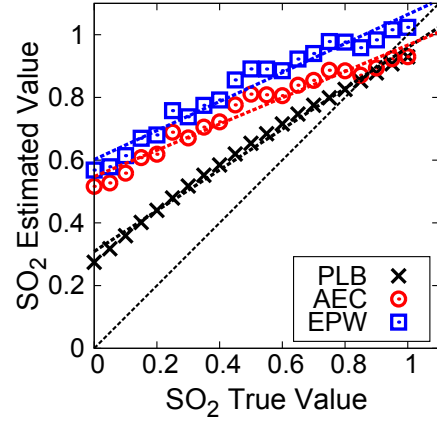


(f)

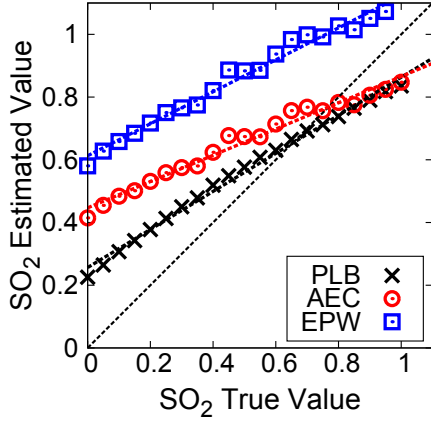
Fig 4.13: The  $\text{SO}_2$  estimation of  $d = 100 \mu\text{m}$  vessel. (a) The monochromatic light with no bandwidth ( $w = 0$ ). (b)  $w = 10 \text{ nm}$ . (c)  $w = 20 \text{ nm}$ . (d)  $w = 30 \text{ nm}$ . (e)  $w = 40 \text{ nm}$ . (f)  $w = 50 \text{ nm}$ .



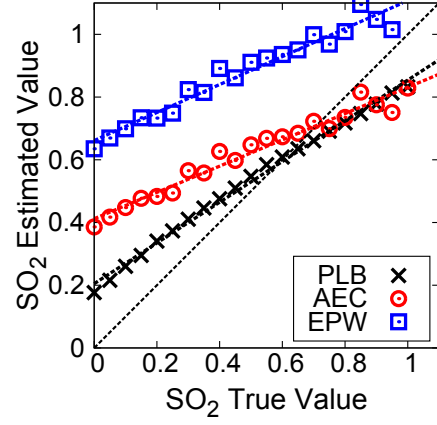
(a)



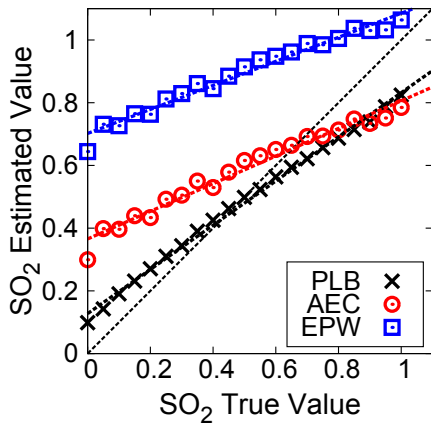
(b)



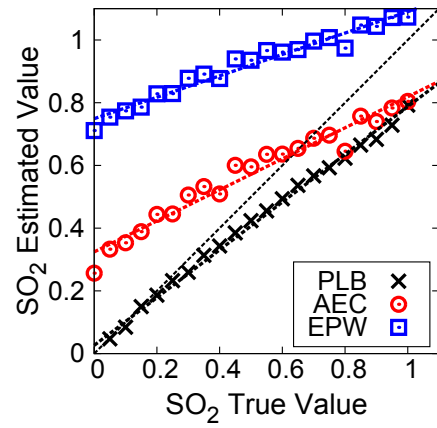
(c)



(d)

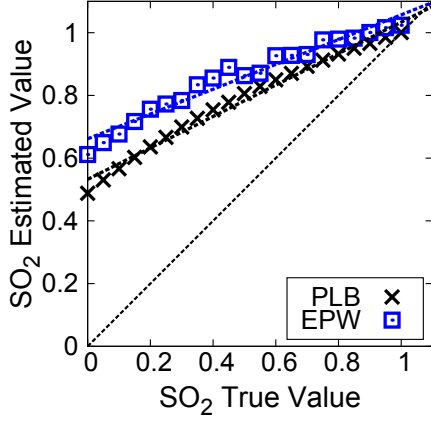


(e)

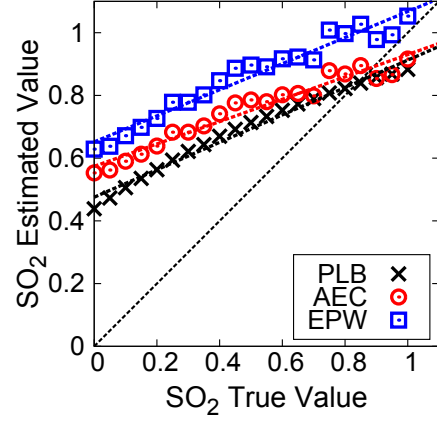


(f)

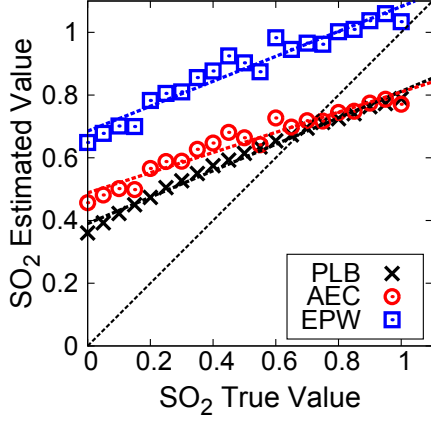
Fig 4.14: The  $\text{SO}_2$  estimation of  $d = 200 \mu\text{m}$  vessel. (a) The monochromatic light with no bandwidth ( $w = 0$ ). (b)  $w = 10 \text{ nm}$ . (c)  $w = 20 \text{ nm}$ . (d)  $w = 30 \text{ nm}$ . (e)  $w = 40 \text{ nm}$ . (f)  $w = 50 \text{ nm}$ .



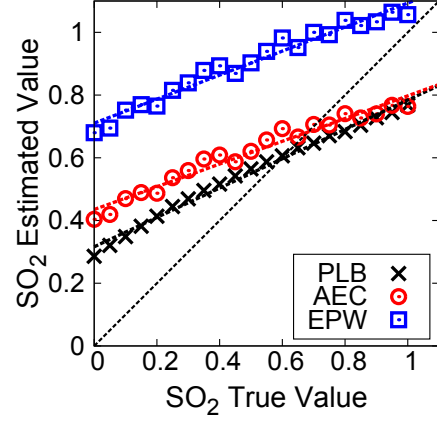
(a)



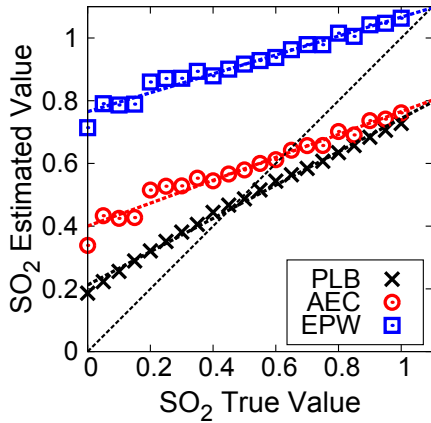
(b)



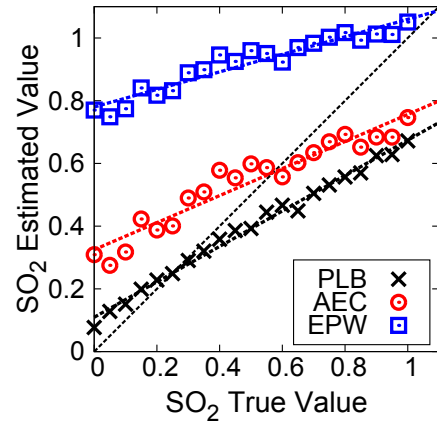
(c)



(d)



(e)



(f)

Fig 4.15: The  $\text{SO}_2$  estimation of  $d = 300 \mu\text{m}$  vessel. (a) The monochromatic light with no bandwidth ( $w = 0$ ). (b)  $w = 10 \text{ nm}$ . (c)  $w = 20 \text{ nm}$ . (d)  $w = 30 \text{ nm}$ . (e)  $w = 40 \text{ nm}$ . (f)  $w = 50 \text{ nm}$ .

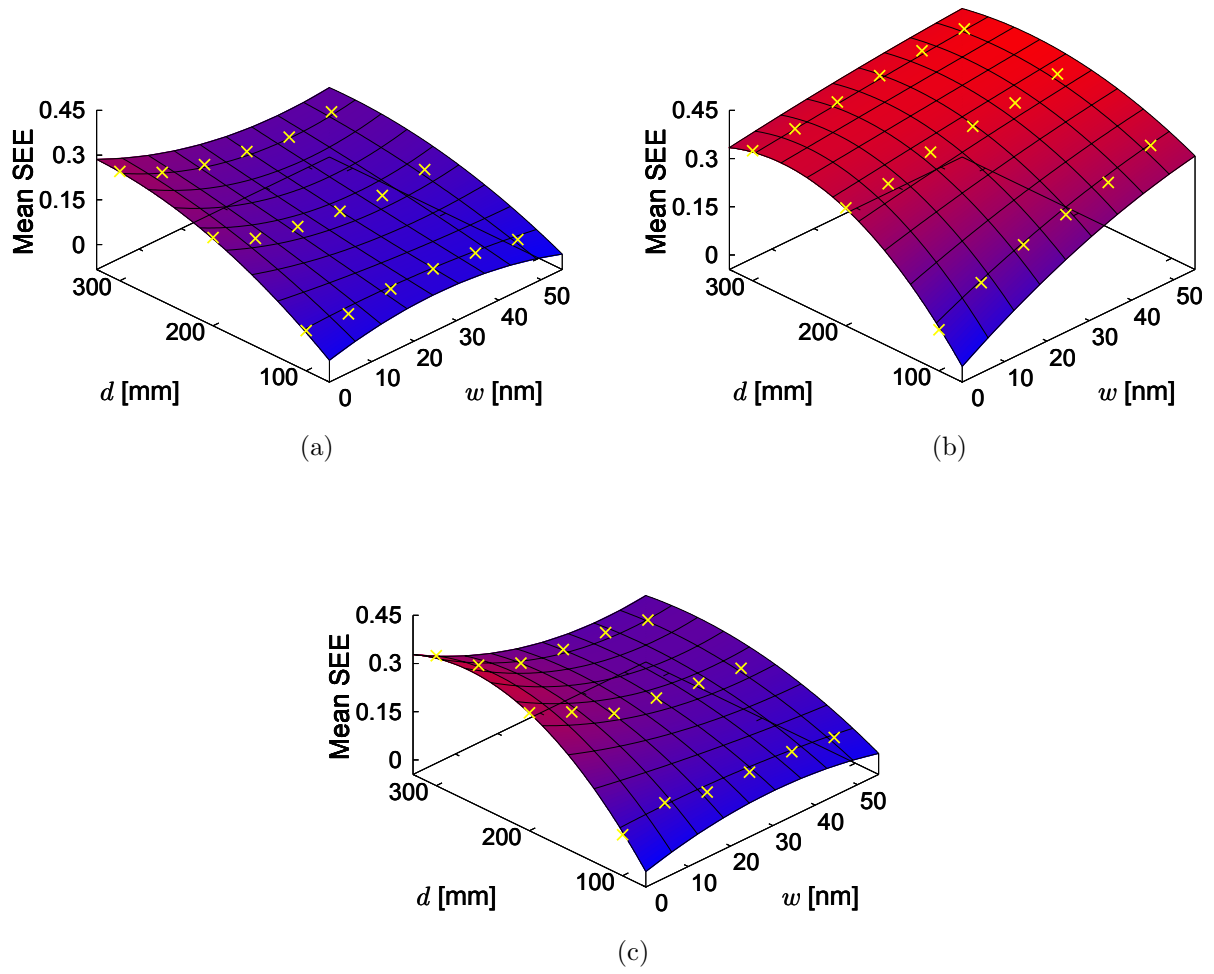


Fig 4.16: The mean of SEE  $\overline{\Delta s}$  surface with the contour interval color. (a) PLB. (b) EPW. (c) AEC.

Table 4.3: The mean SEE  $\overline{\Delta s} \pm \text{SD}$ .

$d$ [ $\mu\text{m}$ ]	$w$ [nm]	Using PLB	Image-based measurement	
			Using EPW	Using AEC
100	0	$0.0512 \pm 0.0237$	$0.0826 \pm 0.0532$	
100	10	$0.0388 \pm 0.0267$	$0.1652 \pm 0.0643$	$0.1183 \pm 0.0759$
100	20	$0.0536 \pm 0.0316$	$0.2194 \pm 0.0658$	$0.0879 \pm 0.0569$
100	30	$0.0524 \pm 0.0303$	$0.2496 \pm 0.0942$	$0.0863 \pm 0.0497$
100	40	$0.0369 \pm 0.0216$	$0.2863 \pm 0.1241$	$0.0860 \pm 0.0505$
100	50	$0.0132 \pm 0.0076$	$0.3377 \pm 0.1401$	$0.0666 \pm 0.0394$
200	0	$0.2121 \pm 0.0725$	$0.3217 \pm 0.1532$	
200	10	$0.1407 \pm 0.0968$	$0.3331 \pm 0.1627$	$0.2607 \pm 0.1705$
200	20	$0.1117 \pm 0.0727$	$0.3678 \pm 0.1485$	$0.1925 \pm 0.1353$
200	30	$0.0944 \pm 0.0569$	$0.3845 \pm 0.1677$	$0.1766 \pm 0.1206$
200	40	$0.0789 \pm 0.0468$	$0.3936 \pm 0.1867$	$0.1591 \pm 0.1036$
200	50	$0.0972 \pm 0.0667$	$0.4198 \pm 0.1994$	$0.1422 \pm 0.0912$
300	0	$0.2830 \pm 0.1510$	$0.3593 \pm 0.1831$	
300	10	$0.2113 \pm 0.1486$	$0.3640 \pm 0.1793$	$0.2663 \pm 0.1823$
300	20	$0.1686 \pm 0.1114$	$0.3838 \pm 0.1824$	$0.2092 \pm 0.1435$
300	30	$0.1440 \pm 0.0880$	$0.4019 \pm 0.1869$	$0.1875 \pm 0.1250$
300	40	$0.1239 \pm 0.0728$	$0.4158 \pm 0.2115$	$0.1769 \pm 0.1118$
300	50	$0.1397 \pm 0.0979$	$0.4199 \pm 0.2181$	$0.1520 \pm 0.0904$

$w$  decreases with an increase in  $d$ . On the other hand, as shown in Fig. 4.16(c) and Table 4.3,  $\overline{\Delta s}$  using AEC decreases with increment of  $w$ . Next, we focused on the changes in  $\overline{\Delta s}$  due to  $d$  of the vessel. From the results, AEC is more precise than EPW for all  $d$  values in each  $w$ .  $\overline{\Delta s}$  using EPW increases with increment of  $d$ . The changing rate of  $\overline{\Delta s}$  due to  $d$  decreases with an increase in  $w$ . By contrast,  $\overline{\Delta s}$  using AEC increases with increment of  $d$ .

The  $\text{SO}_2$  estimation error is caused by measurement errors  $\Delta\Psi$ :

$$\begin{aligned}
\Delta\Psi &= \Psi_{\text{estimated}} - \Psi_{\text{true}} \\
&= \Psi_{\text{estimated}} - \frac{\mu_a(\lambda_2)}{\mu_a(\lambda_1)},
\end{aligned} \tag{4.20}$$

where we used that  $\Psi_{\text{true}}$  is the ratio of absorption coefficients. The  $\text{SO}_2$  estimation error is

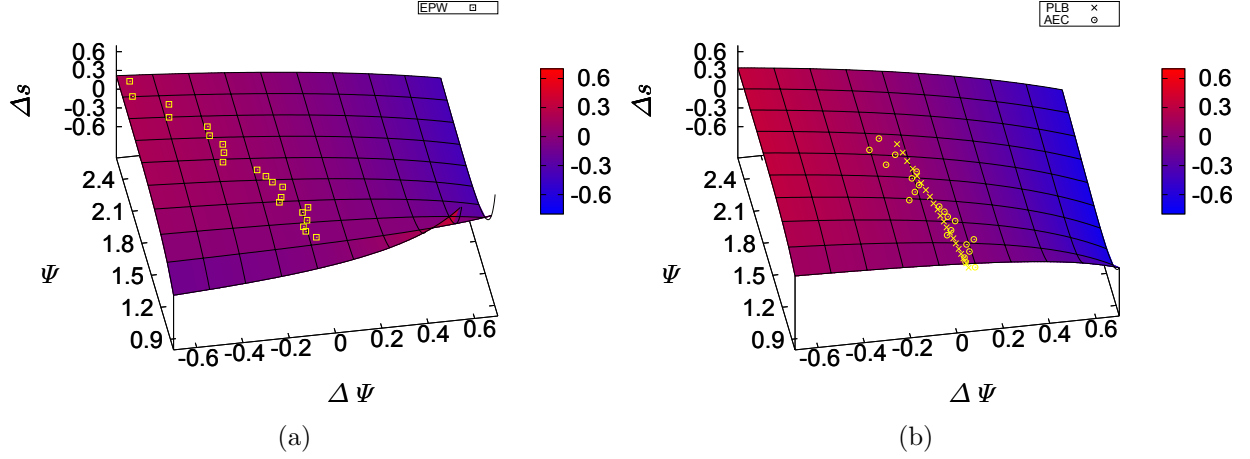


Fig 4.17: The  $\text{SO}_2$  estimation error caused by  $\Delta\Psi$  for use of (a) extinction coefficients at the peak wavelength and (b) AECs of a  $100\ \mu\text{m}$  diameter and a  $30\ \text{nm}$  bandwidth. Symbols depict  $\text{SO}_2$  estimation errors in the simulation.

defined by:

$$\begin{aligned}\Delta s &:= s(\Psi_{\text{true}} + \Delta\Psi) - s(\Psi_{\text{true}}) \\ &= \frac{\varepsilon_{\text{Hb}}(\lambda_1) - \Delta\lambda_1/(\Delta\lambda_2 - \Psi_{\text{true}} \cdot \Delta\lambda_1)}{(\Delta\lambda_2 - \Psi_{\text{true}} \cdot \Delta\lambda_1) + \Delta\lambda_1\Delta\Psi} \Delta\Psi.\end{aligned}\quad (4.21)$$

The relationship between  $\Delta s$ ,  $\Psi_{\text{true}}$ , and  $\Delta\Psi$  is shown in Fig. 4.17. Figures 4.17(a) and 4.17(b) show the relationship using extinction coefficients at the peak wavelength and AECs of a  $100\ \mu\text{m}$  and a  $30\ \text{nm}$  bandwidth. As seen in the results of the simulation,  $\Delta\Psi$  was decreased by use of AECs.

We considered that the SEE was caused by a deviation from Lambert-Beer law due to the scattering event in case of using the extinction coefficient of hemoglobin. In our study we assumed that, the scattering in a tissue and a vessel was more dominant than the absorption over the entire wavelength range and more than  $440\ \text{nm}$ , respectively. Therefore, its effect was not negligible. We considered that its possible effects were the overestimation of intensity in the vessel due to multiple scattering by the surrounding tissue. This caused a loss or a gain of detected intensity. A correction of these effects is included in the term of  $B(\lambda)$  in Eq. (3.11). In our study, we assumed that  $B(\lambda)$  was constant compared to extinction coefficients of hemoglobin and the camera sensitivity, and then it vanishes in Eq. (3.18), i.e. we did not

take into account the influence of the scattering and the other factors. This assumption might not be valid. Thus, we may be able to correct these influence using the average extinction coefficients that include  $B(\lambda)$ .

In addition to the above prediction, we considered that there was another cause of the SEE. Smith [42] pointed out that generally the SEE is due to the combination of the selected wavelengths in retinal vessel oximetry. Here this error is called the *potential error* (PE). The potential error occurs in the difference of the extinction coefficients of hemoglobin and oxygenated hemoglobin between selected wavelengths. Let us consider that  $SO_2$  is a function of the transmittance, and then the PE was defined (see Eqs. (21) and (22) in [42]) by:

$$\Delta s(T_{\lambda_1}, T_{\lambda_2}) = \sqrt{\left(\frac{\partial s(T_{\lambda_1}, T_{\lambda_2})}{\partial T_{\lambda_1}} \Delta T_{\lambda_1}\right)^2 + \left(\frac{\partial s(T_{\lambda_1}, T_{\lambda_2})}{\partial T_{\lambda_2}} \Delta T_{\lambda_2}\right)^2}. \quad (4.22)$$

We rewrite Eq. (4.22) using  $\varepsilon_{Hb, \lambda_i}$  and  $\varepsilon_{HbO_2, \lambda_i}$  to:

$$\begin{aligned} \Delta s(T_{\lambda_1}, T_{\lambda_2}) &= \left| \frac{\varepsilon_{Hb, \lambda_1} \Delta \lambda_2 - \varepsilon_{Hb, \lambda_2} \Delta \lambda_1}{[\Delta \lambda_2 - \Psi \Delta \lambda_1]^2} \frac{1}{D(\lambda_1) \cdot \ln 10} \right| \\ &\times \left[ \left( \frac{D(\lambda_2)}{D(\lambda_1)} \frac{\Delta T_{\lambda_1}}{T_{\lambda_1}} \right)^2 + \left( \frac{\Delta T_{\lambda_2}}{T_{\lambda_2}} \right)^2 \right]^{1/2}. \end{aligned} \quad (4.23)$$

Here, the transmittance and the absorption coefficient can be expressed using the Lambert Beer law:

$$\begin{aligned} T_{\lambda} &= 10^{-\mu_a(\lambda)d}, \\ \mu_a(\lambda) &= [s\varepsilon_{HbO_2, \lambda} + (1-s)\varepsilon_{Hb, \lambda}] c. \end{aligned} \quad (4.24)$$

Since average extinction coefficients vary in  $d$  and  $w$ , the PE also varies in a combination of  $d$  and  $w$ . Here, we evaluated the PE with the procedure proposed by Smith [42] with average extinction coefficients. Figure 4.18 shows the result of the mean PE for a combination of our calculated average extinction coefficients. We used mean FWHM of profiles as the diameter and  $\Delta T_1 = \Delta T_2$  was set as  $1.0 \times 10^{-3}$ . As a result, we verified that the tendency of our SEEs of AEC was consistent with the mean PEs due to changes in average extinction coefficients. From this result, the mean of SEE was greatly affected by the wavelength combination compared with the aforementioned scattering effect. When monochromatic light is irradiated to the model with vessel  $d = 300 \mu\text{m}$ , the mean PE takes the maximum value. In the case of

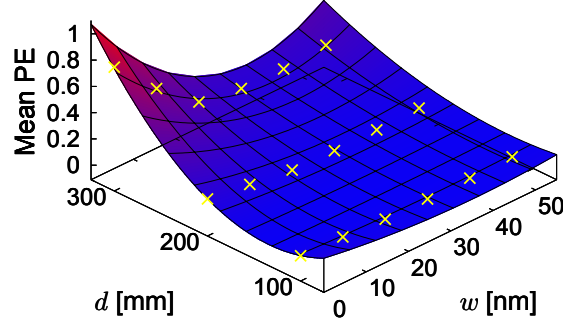


Fig 4.18: The mean PE evaluated by Smith's procedure [42]. The surface is a fitting curve with a bivariate power series until the second-order of both variables.

$w = 0$ , the mean PE occurs in the change of  $d$  rather than the difference of average extinction coefficients and increases as  $d$  increases. This is because average extinction coefficients of any  $d$  are equal.

To evaluate the influence of PE, we performed  $\text{SO}_2$  estimation simulation experiments using other combinations of two wavelengths. We produced the mean PE map for a range of  $400 \sim 600$  nm using AECs of a  $100 \mu\text{m}$  diameter vessel and a 30 nm bandwidth. Figure 4.19(a) shows the PE map. From the PE map, the mean PE for the combination of (474, 510) is small and large for one of (474, 548). We performed the simulation experiments for the two combinations. Figures 4.19(b) and 4.19(c) show the results of the combination of (474, 510) and (474, 548), respectively. The SEE of PLB for (474, 510) and (474, 548) was  $0.0170 \pm 0.001$  and  $0.1196 \pm 0.0284$ , respectively. For AEC, the SEE was  $0.0693 \pm 0.0422$  for (474, 510) and  $0.2559 \pm 0.0700$  for (474, 548). Thus, the optimal combination for SDF oximetry was (474, 510) since the influence of PE for  $\text{SO}_2$  estimation is minimum.

### 4.3 Evaluation of the scattering by tissue and a scattering correction method

We investigated the influence of the scattering by the tissue to the photon propagation in the biological tissue-like phantom model. Experiments of the phantom is described later



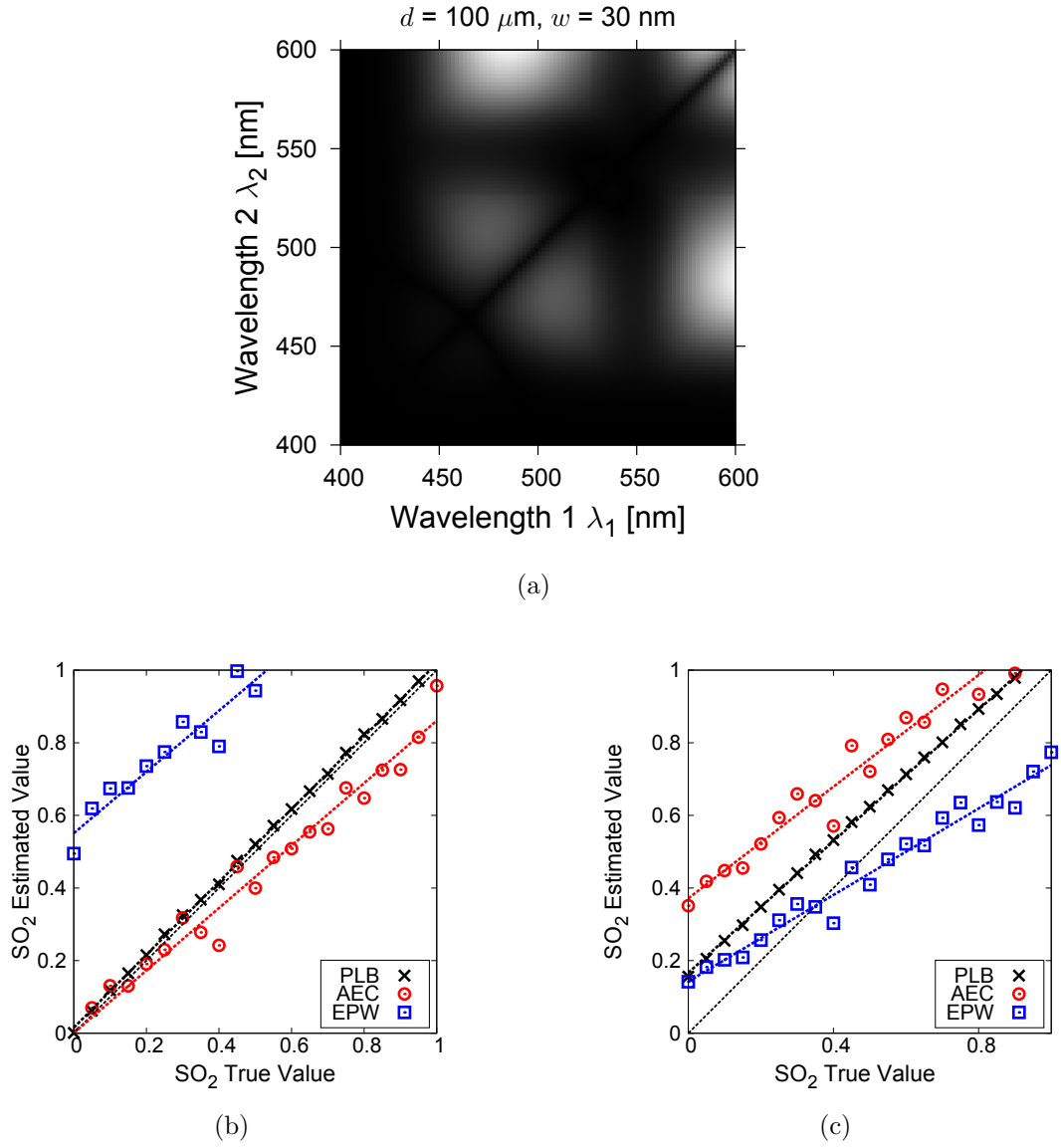


Fig 4.19: The  $\text{SO}_2$  estimation error for choosing wavelengths. (a) Error map.  $\text{SO}_2$  estimation simulation using combination of (b) (474, 510) and (c) (474, 548).

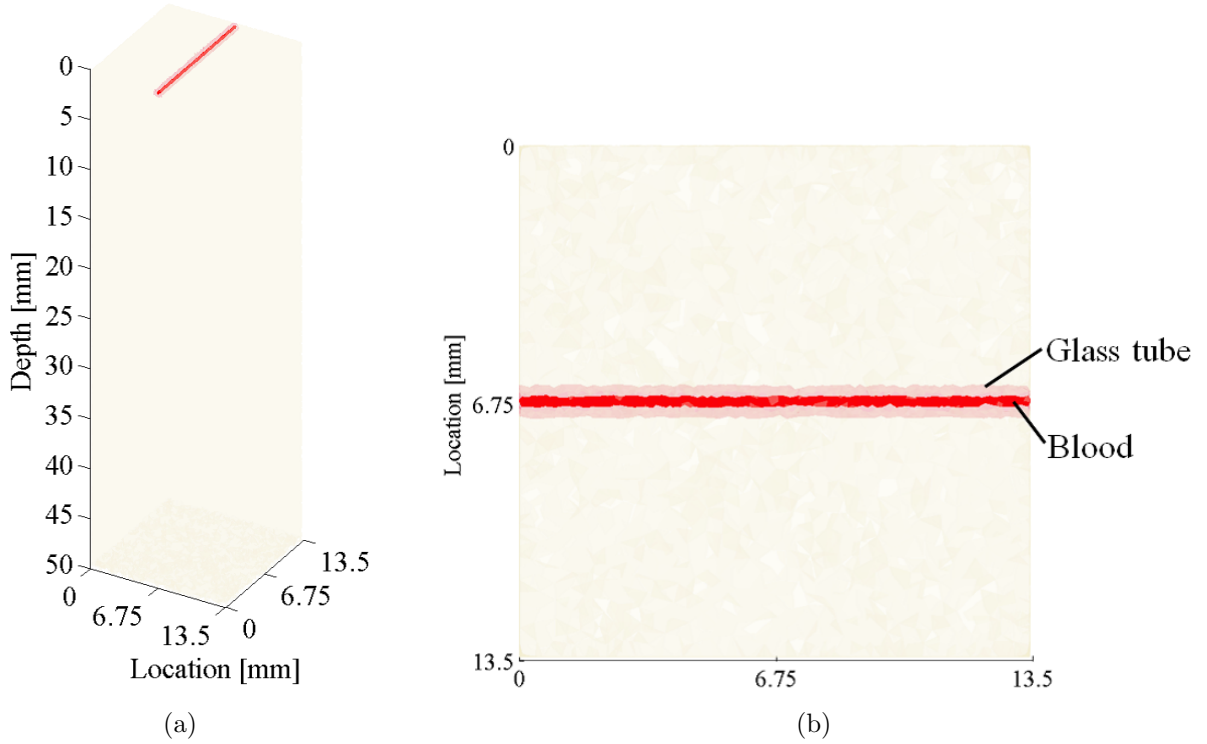


Fig 4.20: The digital phantom model. (a) Overview, and (b) overview from the top side.

in Chapter 5. In this simulation, we performed the tissue scattering correction method and evaluated the validity of the method.

### 4.3.1 Digital phantom model

The digital model simulated a biological tissue-like phantom was constructed using the mesh-generation software *iso2mesh* [71]. We modeled a tissue-like part that included fat emulsion and a blood-injected glass tube with a  $300\ \mu\text{m}$  inner diameter. Figures 4.20(a) and 4.20(b) show the digital model. The size of the model was  $13.5\ \text{mm}$  (width)  $\times 13.5\ \text{mm}$  (depth)  $\times 50\ \text{mm}$  (height).

The scattering coefficient and anisotropy factor of the phantom model were set to those of the fat emulsion by referring to the study by Staveren *et al.* [76]. Staveren *et al.* reported the scattering coefficient and the anisotropy factor of fat emulsion (10%-Intralipid) as:

$$\mu_s(\lambda) = 0.016\lambda^{-2.4},$$

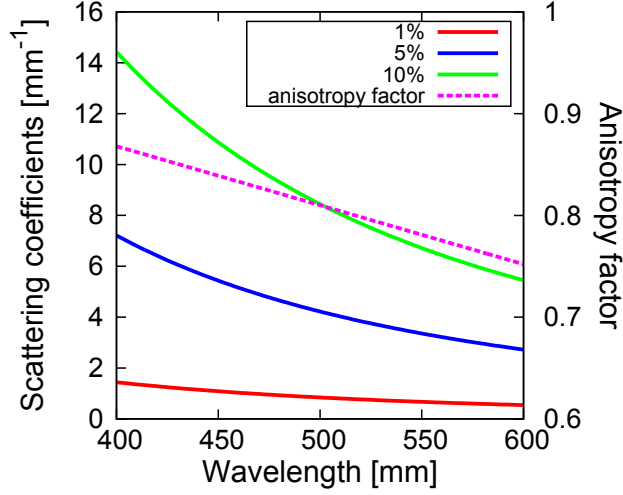


Fig 4.21: Optical properties of fat emulsion with referring to [76].

$$g(\lambda) = 1.1 - 0.58\lambda, \quad (4.25)$$

for  $0.4 \leq \lambda \leq 1.1$ , respectively. Here,  $\lambda$  is in unit of micrometers and  $\mu_s$  is unit of L/mL/mm. Figure 4.21 shows scattering coefficients with the concentration 0.1%, 0.5%, and 1% (left scale) and an isotropy factor of fat emulsion (right scale). Tables 4.4 and 4.5 show the value of the optical properties used in this study. Refractive index of the phantom body, the glass tube (Pyrex glass), and blood was set to 1.440, 1.470, and 1.402, respectively. In this simulation, in order to investigate the influence of fat emulsion, we neglected the optical properties of agar.

The number of incident photons was  $1.0 \times 10^8$  and the geometry of the illumination sources and the detection area were the same as the actual device described in Chapter 2. In our photons tracing, we stopped tracing photons when photons reached the boundary of the sides with the exception of the top and bottom surface.

### 4.3.2 Influence of the scattering on AECs

Figure 4.22 shows virtual SDF images obtained in the simulation. From the results of the AECs calculation shown in Fig. 4.23(a), we found the change of AECs was in the same manner as in the phantom experiment. As shown in Fig. 4.23(b), we also show the results of the calculation of  $\xi$  from Fig. 4.23(a) and found that the relationship between the values was similar to that of the phantom experiment described in Chapter 5.

Table 4.4: Optical properties ( $\mu_s$  and  $g$ ) under the blue illumination.

$\lambda$ [nm]	$\mu_s$ [mm <sup>-1</sup> ]				$g$
	Concentration of fat emulsion				
	0.0%	0.1%	0.5%	1.0%	
420	0.050	1.283	6.416	12.833	0.856
430	0.050	1.213	6.064	12.128	0.851
440	0.050	1.148	5.739	11.477	0.845
450	0.050	1.087	5.437	10.875	0.839
460	0.050	1.032	5.158	10.316	0.833
470	0.050	0.980	4.898	9.7968	0.827
480	0.050	0.931	4.657	9.3141	0.822
490	0.050	0.886	4.432	8.8644	0.816
500	0.050	0.844	4.222	8.4449	0.810
510	0.050	0.805	4.026	8.0529	0.804
520	0.050	0.769	3.843	7.6862	0.798

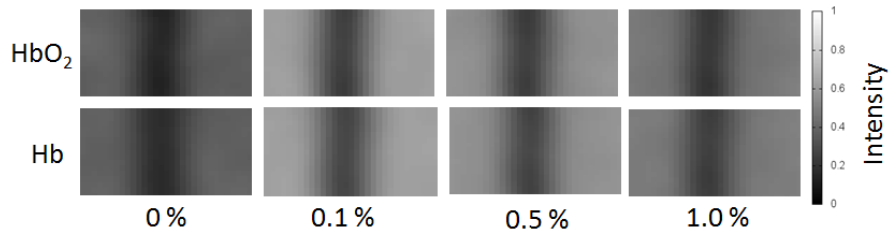
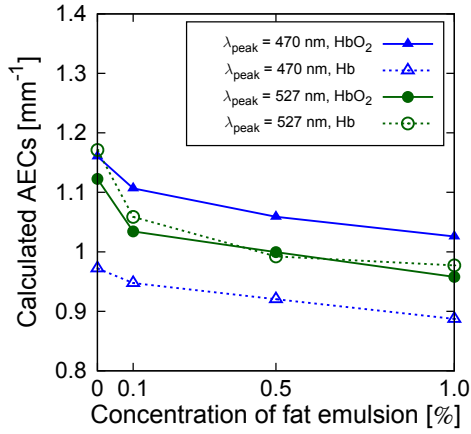


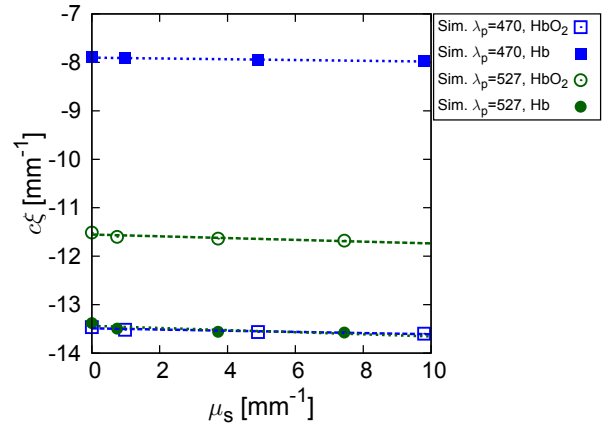
Fig 4.22: The virtual SDF images for the 470 nm peak wavelength illumination.

Table 4.5: Optical properties ( $\mu_s$  and  $g$ ) under the green illumination.

$\lambda$ [nm]	$\mu_s$ [mm <sup>-1</sup> ]				$g$
	0.0%	0.1%	0.5%	1.0%	
477	0.050	0.946	4.728	9.455	0.823
487	0.050	0.900	4.498	8.996	0.818
497	0.050	0.857	4.284	8.568	0.812
507	0.050	0.817	4.084	8.168	0.806
517	0.050	0.779	3.897	7.794	0.800
527	0.050	0.744	3.722	7.443	0.794
537	0.050	0.712	3.558	7.115	0.789
547	0.050	0.681	3.403	6.807	0.783
557	0.050	0.652	3.259	6.517	0.777
567	0.050	0.624	3.122	6.245	0.771
577	0.050	0.599	2.994	5.988	0.765



(a)



(b)

Fig 4.23: Results of the simulation. (a) The AECs normalized by the theoretical values. (b) Results of  $\xi$  in the simulation.

### 4.3.3 Correction method for the tissue scattering

We performed an experiment for  $\text{SO}_2$  estimation by varying  $\text{SO}_2$  of the modeled blood. First,  $\text{SO}_2$  estimation experiments using single-wavelength (470 nm and 527 nm) illuminations are described. Next, we performed the simulation experiments using LED illuminations and  $\text{SO}_2$  estimation using scattering-corrected AECs calculated in §4.3.2, single-wavelength extinction coefficients, and non-corrected AECs.

#### Single-wavelength illuminations

We performed the simulation of single-wavelength illuminations such as a laser light source. Absorption coefficients with  $\text{SO}_2$  was set to values of the literature [10, 73]. We estimated  $\text{SO}_2$  from SDF images under blue and green illumination using Eq. (3.10). The model was assumed to include 0.0%, 0.1%, 0.5%, or 1.0% fat emulsion and a glass tube of 300  $\mu\text{m}$  diameter. The total number of photons was  $1.0 \times 10^8$ .

Figures 4.24(a) and 4.24(b) show the relationship between average absolute maximum slope  $|m|$  calculated from blue (470 nm) or green (527 nm) image and  $\text{SO}_2$ . In this case, we could find both the  $\text{SO}_2$ -dependence of  $|m|$  calculated from blue images as expected and the  $\text{SO}_2$ -independence of one from green images. From these results,  $|m|$  was valid as a feature value for calculating the tissue correction term. Figure 4.25 show the relationships between  $|m|$  and  $\mu_s$  and between  $|m|$  and  $\xi$ . We performed  $\text{SO}_2$  estimation using these relationships.

Figure 4.26(a) shows results of  $\text{SO}_2$  estimation using extinction coefficients of single-wavelengths. As seen in results, the results were similar to ones shown in Fig. 4.15(a). The average absolute error (AAE) is shown in Table 4.6. The average of AAE was 29.3%. Figure 4.26(b) shows results for the tissue scattering correction. In this case, the average of AAE was 15.8%. For 0.1% fat emulsion, the AAE was minimum, 2.9%. From these results, we found the validity of the tissue scattering correction method.

#### LED illuminations

In this section, we investigated the influence of choosing AECs for our SDF oximetry method using LED illuminations. We estimated  $\text{SO}_2$  from SDF images under blue and green illumina-

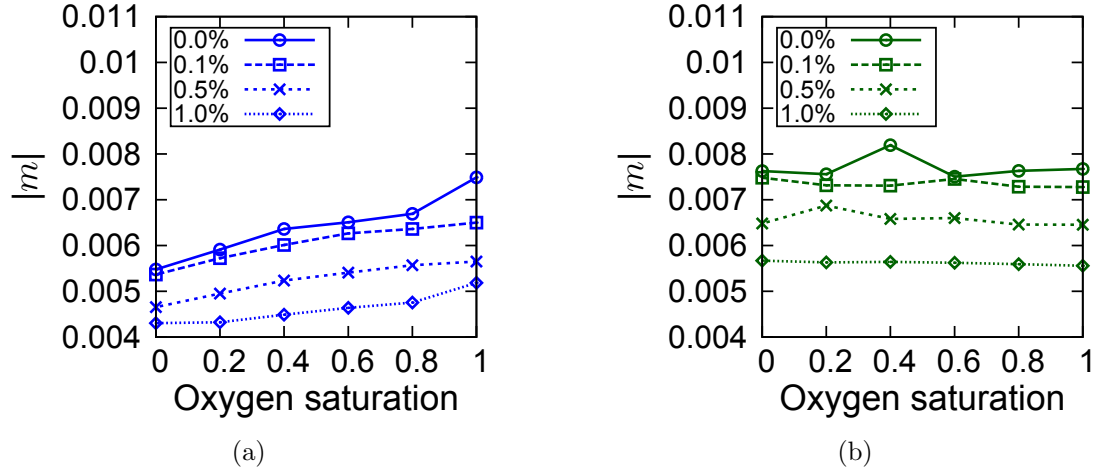
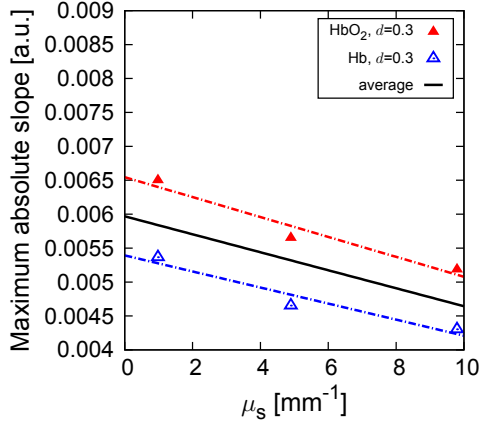


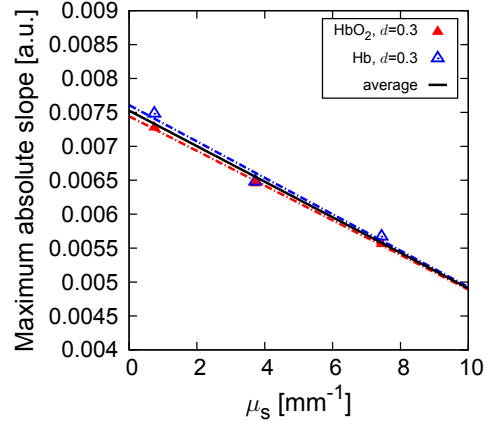
Fig 4.24: The average absolute maximum slope  $|m|$  calculated from (a) 470 nm (b) 527 nm images.

Table 4.6: The AAE [%] of estimated values.

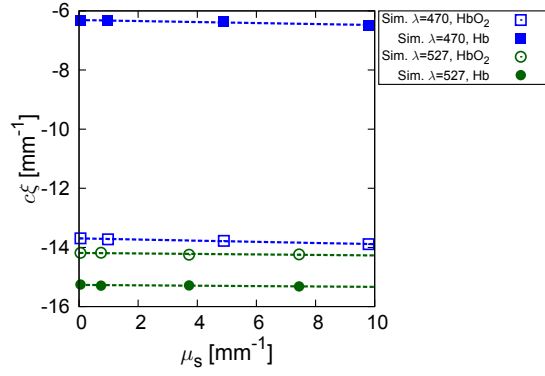
phantom		Correction method
fat emulsion content	Peak-wavelength	
0.0%	32.7	17.6
0.1%	29.0	2.9
0.5%	28.1	16.5
1.0%	27.5	26.2



(a)



(b)



(c)

Fig 4.25: The relationships for the tissue-scattering correction method. The relationships between  $\mu_s$  and  $|m|$  calculated from (a) blue- (b) green-band images. (c) The relationship between  $|m|$  and  $\xi$ .



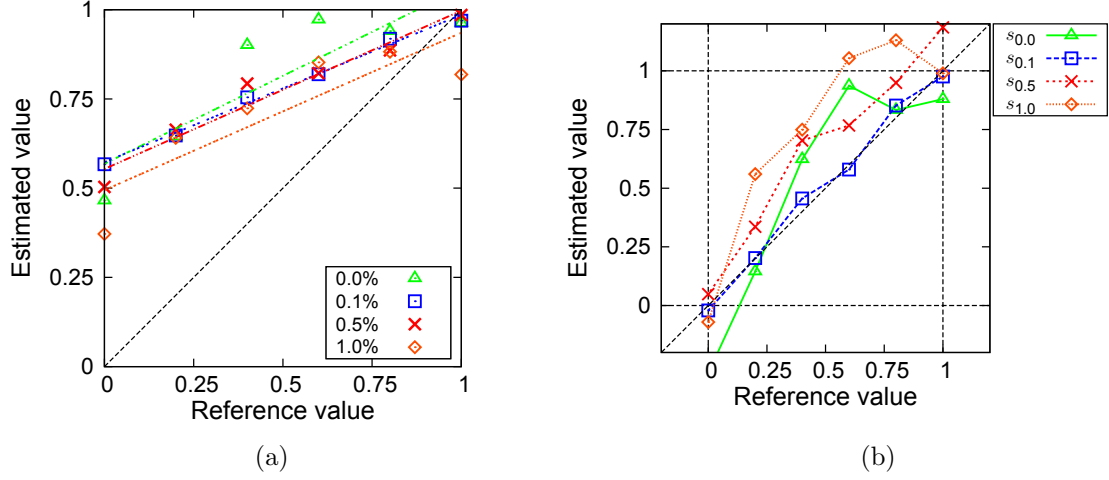
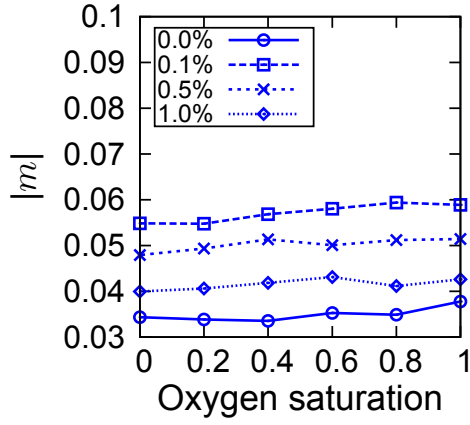


Fig 4.26: Results of the SO<sub>2</sub> estimation for the single-wavelength light sources. (a) Results using extinction coefficients at the peak-wavelength. (b) Results using the correction method.

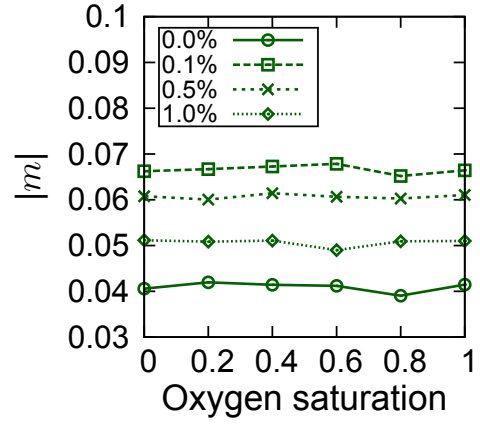
tion using Eq. (3.10). Seven types of hemoglobin extinction coefficients were tested: molar extinction coefficients [10], the theoretical value without the scattering correction determined by Eq. (3.18), the four types of AECs determined from the same scattering model, and corrected AEC by our the correction method. The model was assumed to include 0.0%, 0.1%, 0.5%, or 1.0% fat emulsion and a glass tube of 300  $\mu\text{m}$  diameter. The total number of photons was  $1.0 \times 10^8$ . The bandwidth was 30 nm.

Figure 4.27 shows the average absolute maximum slope  $|m|$  calculated from blue- or green-band images. We could find the SO<sub>2</sub>-dependence of  $|m|$  calculated from blue-band images as compared to green-band images. The relationship between  $\mu_s$  and  $|m|$  is shown in Fig. 4.28. Results of the SO<sub>2</sub> estimation are shown in Figs. 4.29(a), 4.29(b), 4.29(c), and 4.29(d) for 0.0%, 0.1%, 0.5% and 1.0% fat emulsion-included model, respectively. The estimation results of each fat emulsion concentration phantom using AECs determined from the same fat emulsion concentration phantom were extracted from Figs. 4.29(a) to 4.29(d) and summarized in Fig. 4.29(e). Estimated values using the AECs determined with the model of 0.0%, 0.1%, 0.5%, and 1.0% fat emulsion are represented by  $s_{0.0}$ ,  $s_{0.1}$ ,  $s_{0.5}$ , and  $s_{1.0}$ , respectively.  $s_{\text{Hemo}}$  and  $s_{\text{Theory}}$  are ones using diameter- and scatterers concentration-independence molar hemoglobin extinction coefficients and theoretical values, respectively.

As shown in Table 4.7, in case that AECs determined from models with a similar concen-

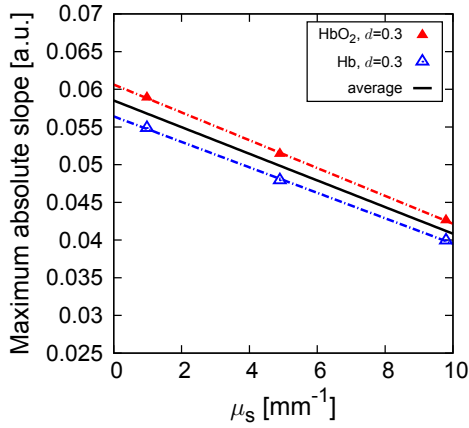


(a)

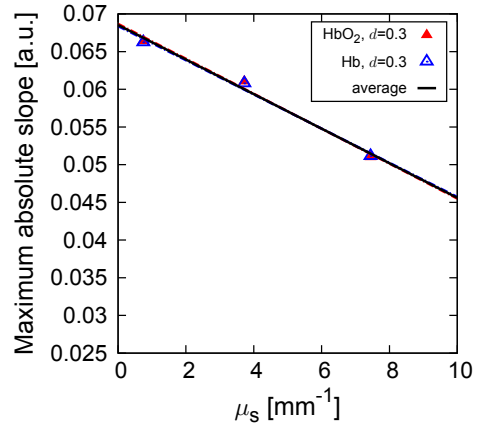


(b)

Fig 4.27: The average absolute maximum slope  $|m|$  calculated from (a) blue- (b) green-band images.



(a)



(b)

Fig 4.28: The relationship between  $\mu_s$  and  $|m|$  calculated from (a) blue- (b) green-band images.

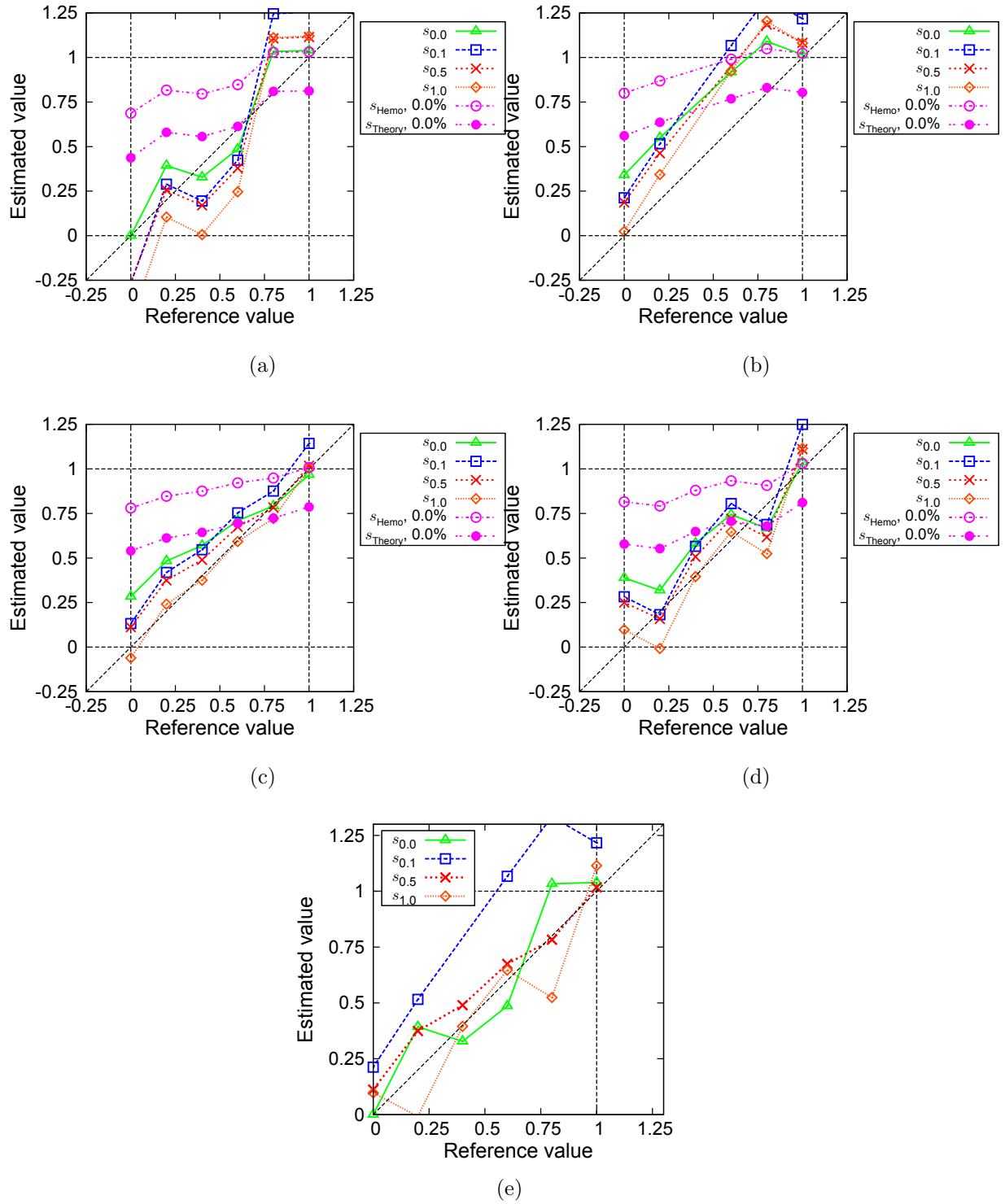


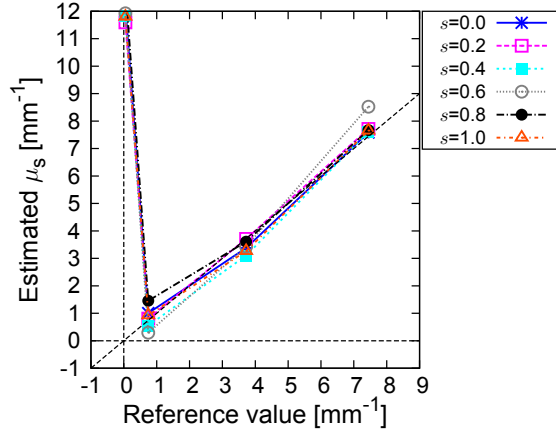
Fig 4.29:  $\text{SO}_2$  estimation results using six types of extinction coefficients for turbid phantoms of (a) 0.0% (b) 0.1% (c) 0.5% (d) 1.0% fat emulsion with the glass tube of  $300\ \mu\text{m}$  diameter. (e) Estimation values using the suitable AECs extracted from the results of (a) to (d).

Table 4.7: The AAE [%] of estimated values.

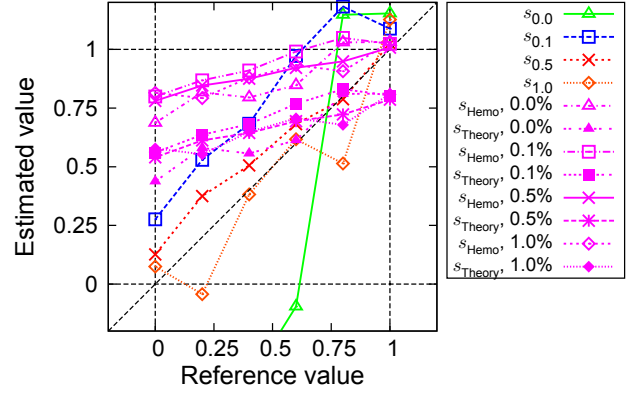
phantom	AECs used						
fat emulsion	Measured from a turbid phantom						Correction
content	$s_{0.0}$	$s_{0.1}$	$s_{0.5}$	$s_{1.0}$	$s_{\text{Hemo}}$	$s_{\text{Theory}}$	method
0.0%	10.9	24.0	19.8	29.3	36.8	19.7	60.0
0.1%	26.5	34.1	24.9	18.6	44.0	27.9	28.9
0.5%	14.8	14.5	8.1	3.6	39.7	26.3	8.8
1.0%	16.7	17.2	13.6	12.5	39.3	26.6	12.8

tration of scatterers were used, the absolute average error (AAE) of the results was smaller. When the AEC used is not suitable, the influence of the scattering causes an error in measurement of  $\Psi$  and the error of the estimated value increases. In  $s_{\text{Hemo}}$  and  $s_{\text{Th}}$ , although the results of  $s_{\text{Th}}$  were more accurate than those of  $s_{\text{Hemo}}$ , both absorption coefficients led to a greater estimation than the AECs did. By comparing estimation results with AECs calculated from the model and  $s_{\text{Th}}$ , we also found that the AAE could be reduced by 18.2% for a 0.5% phantom at the maximum. This means that the good performance of the SDF oximetry requires correction for the influence of the tissue scattering. In this study, we clarified that the tissue scattering had a great impact on the SDF oximetry.

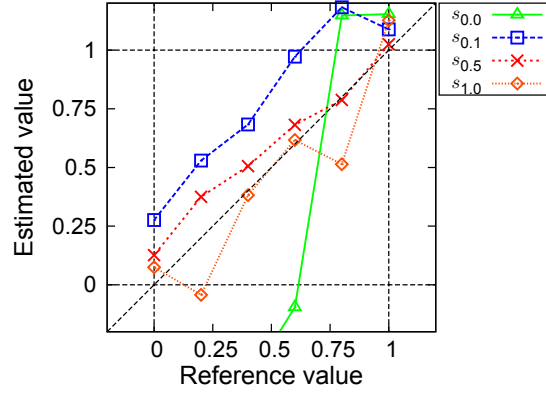
We show results using our scattering correction method in Fig. 4.30. Figures 4.30(a) and 4.30(b) show results of the estimation of the scattering coefficient of the models from the average maximum absolute slope and the  $\text{SO}_2$  estimation from the estimated scattering coefficients. The AAE of the estimation is shown in Table 4.7. From the results, by using our method, the accuracy was improved compared to both estimation results with the extinction coefficients at the peak wavelength and non-corrected AECs.



(a)



(b)



(c)

Fig 4.30:  $\text{SO}_2$  estimation results using our scattering correction method. (a) Results of the estimation of the scattering coefficient from the average maximum absolute slope. (b) Results of  $\text{SO}_2$  estimation using our correction method. (c) Comparison of (b) to results using the extinction coefficient at the peak wavelength and AECs without the scattering correction.

# Chapter 5 BIOLOGICAL PHANTOM EXPERIMENTS

We investigated the influence of the scattering by a medium surrounding a blood vessel using biological tissue-like phantoms. The biological tissue-like phantoms are described in § 5.1. The scattering was controlled in the amount of scatterers included in the phantoms. Blood vessels were simulated by glass tubes. Image analysis used in this experiment is shown in § 5.2. As shown in § 5.3, in this experiment, we determined AECs and performed  $\text{SO}_2$  estimation experiment. In the  $\text{SO}_2$  estimation experiments, we confirmed both the impact of the scattering for  $\text{SO}_2$  and the validity of our correction method.

## 5.1 Biological tissue-like phantoms

Agar and fat emulsion are widely used as materials of a solid biological tissue-like phantom [78]. Since the hardness of agar can be changed easily in an amount of agar powder, biological tissue can be simulated by using agar for the hardness. Fat emulsion such as Intralipid (Kabi Vitrum Inc, Alameda, California, USA) and Intralipos (Otsuka Pharmaceutical Co., Ltd., Tokyo, Japan) has similar spectral characteristics of the scattering to the biological tissue. In this study, we made a tissue-like agar phantom that included cylindrical glass tubes. Figure 5.1 shows a schematic cross-sectional diagram of the phantom and a photograph. The glass tubes were used to simulate blood vessels. The main body of the phantom was made by dissolving dry agar powder (Wako Pure Chemical Industries, Ltd., Tokyo, Japan) in water and mixing it with fat emulsion (Intralipos Injection 10%, Otsuka Pharmaceutical Co., Ltd., Tokyo, Japan). Fat emulsion is typically used as a scattering medium for phantoms that

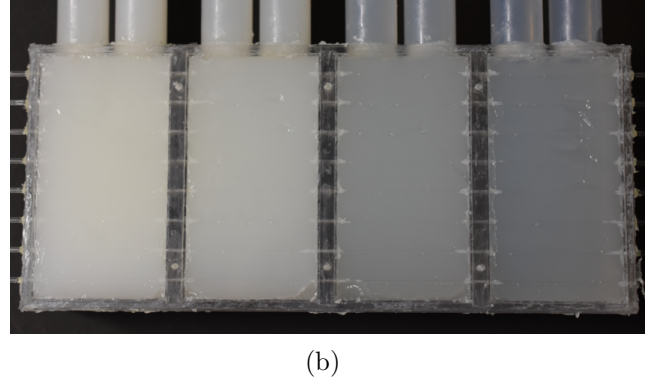
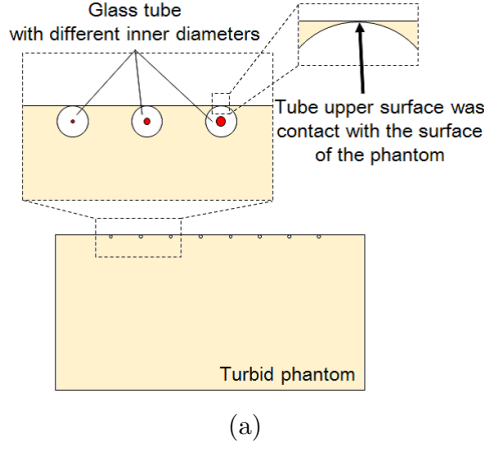


Fig 5.1: Tissue-like turbid phantom. (a) Schematic cross-sectional diagram of the phantom including glass tubes. (b) A photograph of four phantoms. From the right, the phantoms contain 0.0, 0.1, 0.5 or 1.0% fat emulsion.

mimic turbid tissues in optical experiments. The manufacturer's data sheet describes the constituents of the fat emulsion in a 250 mL bottle as: 25 g of soybean oil, 3 g of lecithin, and 5.5 g of glycerin. The scattering occurs in the soybean oil and lecithin [76]. Hereinafter, the soybean oil and lecithin are called scatterers in the fat emulsion. We prepared four agar phantoms simultaneously with the four different concentrations of fat emulsion. This was to solidify the agar under the same conditions. As a concentration of fat emulsion, we set to 0.0, 0.1, 0.5 or 1.0%. The scattering coefficient of these concentration of fat emulsion [76] is similar to ones of the human tissue [74]. The total size of each phantom is 5.4 cm (width)  $\times$  10 cm (depth)  $\times$  5 cm (height).

We used glass tubes with outer diameter of 1 mm and inner diameters of 100, 200 or 300  $\mu\text{m}$  (Sun-yell Co., Kyoto, Japan). Changing the inner diameter of the glass tubes allowed us to evaluate the influence due to blood vessel diameter. As shown in Fig. 5.1(a), glass tubes filled with heparinized bovine blood were positioned flatly within the phantom such that one point of a tube upper surface was in contact with the surface of the phantom body. In this study, depth of the center of each tube was fixed at 0.5 mm. The oxygenated blood ( $s = 1$ ) and the de-oxygenated blood ( $s = 0$ ) were prepared by injecting oxygen and mixing excess sodium dithionite ( $\text{Na}_2\text{S}_2\text{O}_4$ ) into blood, respectively. For measuring  $\text{SO}_2$  and the amount of hemoglobin of blood, blood analysis was performed with a blood gas analyzer i-STAT 300F

(Fuso Pharmaceutical Industries, Ltd., Osaka, Japan) with the EG6+ cartridges.

## 5.2 Image analysis

For further processing and analysis of the SDF images, we utilized custom-built software codes designed in C++ and Matlab (MathWorks, Natick, MA, USA). For all SDF images from the camera, a gamma correction was first performed to linearize the relationship between the light intensity and the camera signal. Then, smoothing with a Gaussian filter and morphological opening processing were performed to remove noise. For the measurement of the light intensity from an SDF image, we analyzed the profile of a blood vessel region in the image. Figure 5.2 shows an intensity profile  $f(x)$  of an SDF image along the direction  $x$  perpendicular to the glass tube filled with blood. The pixel value corresponding to the minimum intensity  $I_{\text{out}}$  of light transmitted through blood is represented by:  $p_{\text{out}} := f(x_{\text{min}})$ , where  $x_{\text{min}}$  represents the position of the minimum pixel value. The position of the two edges in the profile  $f(x)$  in Fig. 5.2 is then defined as follows. From each side of the valley of  $f(x)$  the maximum absolute slope ( $|m_{\text{left}}|$  or  $|m_{\text{right}}|$ ) is found. The edge point in each side is defined at the position around the shoulder that the slope is  $1/8$  of each maximum value [39]. The incident pixel value  $p_{\text{in}}$  corresponding to the intensity  $I_{\text{in}}$  of incident light is defined as one at  $x_{\text{min}}$  on the line  $c(x)$  that connects between two edges [77]:  $p_{\text{in}} := c(x_{\text{min}})$ . The optical density of Eq. (3.21) can be calculated with the following equation:

$$\bar{D} = -\log \left[ \frac{p_{\text{out}}}{p_{\text{in}}} \right]. \quad (5.1)$$

The light path in blood is defined as the width that the horizontal line  $p(x) = p_{\text{out}} + (p_{\text{in}} - p_{\text{out}})/2$  cuts the profile as shown in Fig. 5.2. The average maximum slope of both sides of the valley  $\bar{m} = (|m_{\text{left}}| + |m_{\text{right}}|)/2$  is used in the calculation of the relation to the tissue scattering coefficient.



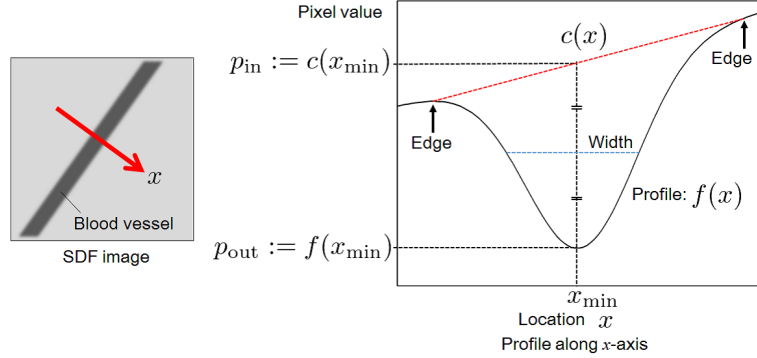


Fig 5.2: The optical density measurement procedure from an SDF image. The profile  $f(x)$  and the edge-connection line  $c(x)$  are depicted by the black solid line and the red dashed line, respectively. The location of the minimum pixel value represents  $x_{\min}$ .

## 5.3 Results

### 5.3.1 Calculation of AECs

We measured the AECs using Eq. (3.21) with our manufactured phantoms. We obtained the SDF images of the turbid phantoms described in the previous section. The concentration of hemoglobin of the blood was 126 g/L when it was measured with the blood gas analyzer. Representative SDF images are shown in Figs. 5.4(a) and 5.4(b). These are images of oxygenated and de-oxygenated blood in the tube with a 300  $\mu\text{m}$  inner diameter. Pseudo-RGB color images were synthesized using the 624, 527, and 470 nm peak-wavelength images as R, G, and B components, respectively. Three-band images were obtained by switching the color of the LEDs. We also confirmed more blur in the images of the phantom with a higher concentration of fat emulsion. This means more scatterers (soybean oil and lecithin) are in the main body of the phantom. Figures 5.5(a) and 5.5(b) show the calculation results of the AECs of oxygenated and de-oxygenated hemoglobin as a function of the concentration of fat emulsion. In Fig. 5.5(b), calculated values of both oxygenated and de-oxygenated hemoglobin under the 527 nm wavelength illumination were approximately the same for each diameter except for the 0.1% fat emulsion. This consistency was attributed to the wavelength being near the isosbestic point as shown in Fig. 2.6. We found the AECs monotonically decreased with increasing of concentration of scatterers in all cases of 100, 200, and 300  $\mu\text{m}$  diameter. This means that the transmittance  $T$  of the blood vessel in an SDF image was

overestimated by adding the circumjacent scattered light intensity  $I'$  to the transmitted light intensity  $I_{\text{out}}$  that passed through only blood, i.e.  $I_{\text{out}} + I'$ . Since the AEC is proportional to  $-\log(T)$ , the AECs resulted in underestimation due to an apparent increase of  $T$ . Theoretical values without both the scattering and the light entry from the peripheral region calculated in Eq. (3.16) were  $c\bar{\varepsilon}_{\text{HbO}_2} = 14.1 \text{ mm}^{-1}$  and  $c\bar{\varepsilon}_{\text{Hb}} = 8.1 \text{ mm}^{-1}$  for 470 nm peak wavelength and  $c\bar{\varepsilon}_{\text{HbO}_2} = 13.1 \text{ mm}^{-1}$  and  $c\bar{\varepsilon}_{\text{Hb}} = 15.1 \text{ mm}^{-1}$  for 527 nm peak wavelength using  $c = 126 \text{ g/L}$ . These values were numerically calculated with the condition:  $S(\lambda)$  was manufacturer's data,  $R(\lambda)$  was unity, extinction coefficients  $\varepsilon(\lambda)$  are set to the literature values [10], and  $B(\lambda_{\text{peak}}) - B(\lambda)$  was vanished. Compared with theoretical values, all AECs shown in Figs. 5.5(a) and 5.5(b) were reduced to less than 1/2.

### 5.3.2 Scattering correction term of AECs and maximum slope of intensity profile

We calculated the term  $\xi$  in Eq. (3.22) by subtracting the theoretical value (the first term of the right hand side of Eq. (3.22)) from the measured value (the left hand side). We then regarded  $\xi$  as a function of the scattering coefficient  $\mu_s^{\text{phantom}}$  of the phantom body. The scattering coefficients were calculated from the literature values of ones per unit concentration with reference to [76] and the concentration  $C$  of fat emulsion used. We also assumed that  $\mu_s^{\text{phantom}}$  was linearly correlated with the concentration  $C$  of fat emulsion. Figure 5.5(c) shows the calculated  $\xi$ . We performed line fitting and obtained:

$$\begin{aligned}\xi_{\lambda_p=470, \text{HbO}_2} &= -10.97 - 0.13\mu_s^{\text{phantom}}, \\ \xi_{\lambda_p=470, \text{Hb}} &= -6.3 - 0.08\mu_s^{\text{phantom}}, \\ \xi_{\lambda_p=527, \text{HbO}_2} &= -9.56 - 0.15\mu_s^{\text{phantom}}, \\ \xi_{\lambda_p=527, \text{Hb}} &= -11.4 - 0.11\mu_s^{\text{phantom}},\end{aligned}\tag{5.2}$$

in unit of  $\text{mm}^{-1}$  as a linear function for a 300  $\mu\text{m}$  diameter. The influence of  $\xi$  increased with the increase of scatterers.

We determined the relation between  $\bar{m}$  calculated from a SDF image under green illumination and  $\mu_s^{\text{phantom}}$ . Figure 5.3 shows the average absolute maximum slope  $|m|$  calculated from blue- or green-band images. From Fig. 5.3,  $\text{SO}_2$ -independence of green-band images

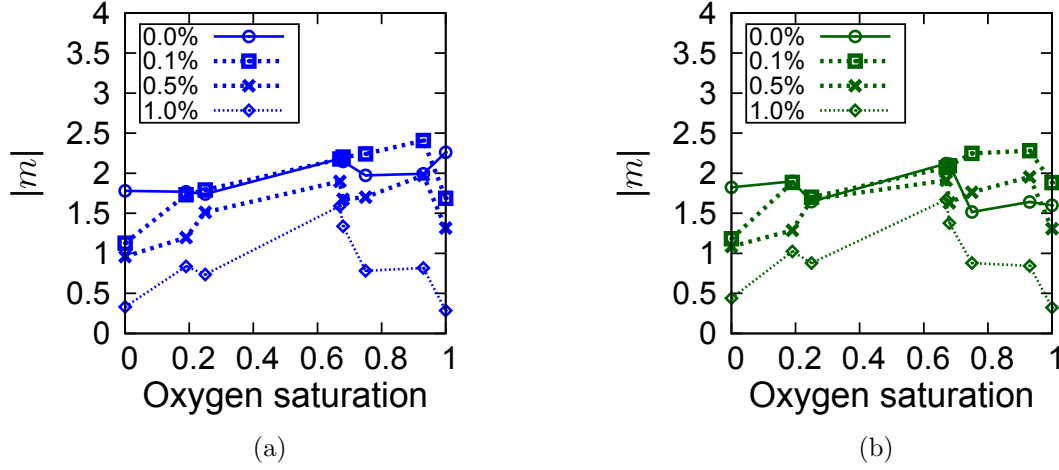
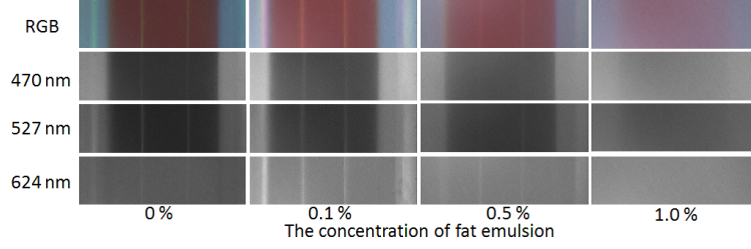


Fig 5.3: The average absolute maximum slope  $|m|$  calculated from (a) blue- (b) green-band images.

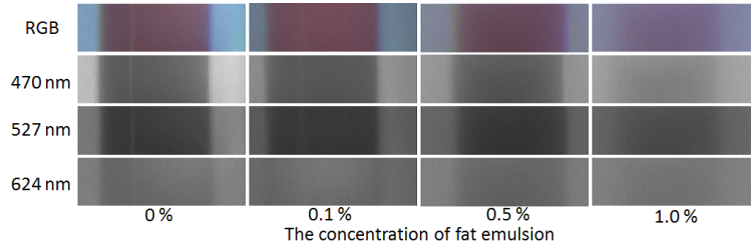
could not find in the same manner as the simulation. We obtained the relationship between  $|m|$  and  $\mu_s$  using line fitting as a linear function. As shown in Fig. 5.5(d), the results was  $|\bar{m}_{\text{HbO}_2}| = 2.10 - 0.23\mu_s^{\text{phantom}}$  and  $|\bar{m}_{\text{Hb}}| = 1.35 - 0.11\mu_s^{\text{phantom}}$  for a 300  $\mu\text{m}$  diameter glass tube and the average of them was  $|\bar{m}| = 1.73 - 0.17\mu_s^{\text{phantom}}$ . We found the decrease of  $\bar{m}$  with the increase of  $\mu_s^{\text{phantom}}$  and the difference of the characteristics for oxygenated or de-oxygenated blood. This was because green LED illumination sources have a non-negligible bandwidth.

### 5.3.3 $\text{SO}_2$ estimation

We performed an experiment for  $\text{SO}_2$  estimation by varying  $\text{SO}_2$  of bovine blood injected into glass tubes within the turbid phantoms.  $\text{SO}_2$  was controlled by injecting oxygen and carrying out an anaerobic treatment. In this section, we investigated the influence of choosing AECs for our SDF oximetry method. We estimated  $\text{SO}_2$  from SDF images under blue and green illumination using Eq. (3.10). Six types of hemoglobin extinction coefficients were tested: molar extinction coefficients [10], the theoretical value without the scattering correction determined by Eq. (3.18), and the four types of AECs determined experimentally from the phantoms. Those phantoms were as shown in Fig. 5.1 and included 0.0%, 0.1%, 0.5%, or 1.0% fat emulsion and the glass tube of 300  $\mu\text{m}$  diameter.



(a)



(b)

Fig 5.4: Cropped SDF images of the turbid phantom with the glass tube of  $300\ \mu\text{m}$  inner diameter for (a)  $\text{SO}_2 = 100\%$  and (b)  $\text{SO}_2 = 0\%$  blood-filled glass tube. These images are captured using blue (the second row), green (the third row), and red (the lower row) LED illumination sources and, from the left hand side, for the phantom containing with the only agar powder, and phantoms with 0.1, 0.5, or 1.0% fat emulsion. Color images of the top row are synthetic images using red, green, and blue illumination.

For the experiment, we made another set of phantoms with the same concentrations of fat emulsion as those for the AECs determination. Results of the  $\text{SO}_2$  estimation are shown in Figs. 5.6(a), 5.6(b), 5.6(c), and 5.6(d) for 0.0%, 0.1%, 0.5% and 1.0% fat emulsion-included phantoms with the glass tube of  $300\ \mu\text{m}$  diameter, respectively. The estimation results of each fat emulsion concentration phantom using AECs determined from the same fat emulsion concentration phantom were extracted from Figs. 5.6(a) to 5.6(d) and summarized in Fig. 5.6(e). Reference value was  $\text{SO}_2$  measured with the blood gas analyzer. Estimated values using the AECs calculated with the phantoms of 0.0%, 0.1%, 0.5%, and 1.0% fat emulsion are represented by  $s_{0.0}$ ,  $s_{0.1}$ ,  $s_{0.5}$ , and  $s_{1.0}$ , respectively.  $s_{\text{Hemo}}$  and  $s_{\text{Theory}}$  are ones using diameter- and scatterers concentration-independence molar hemoglobin extinction coefficients and theoretical values, respectively. We set  $\text{SO}_2$  values to be in roughly the full range from 19% to

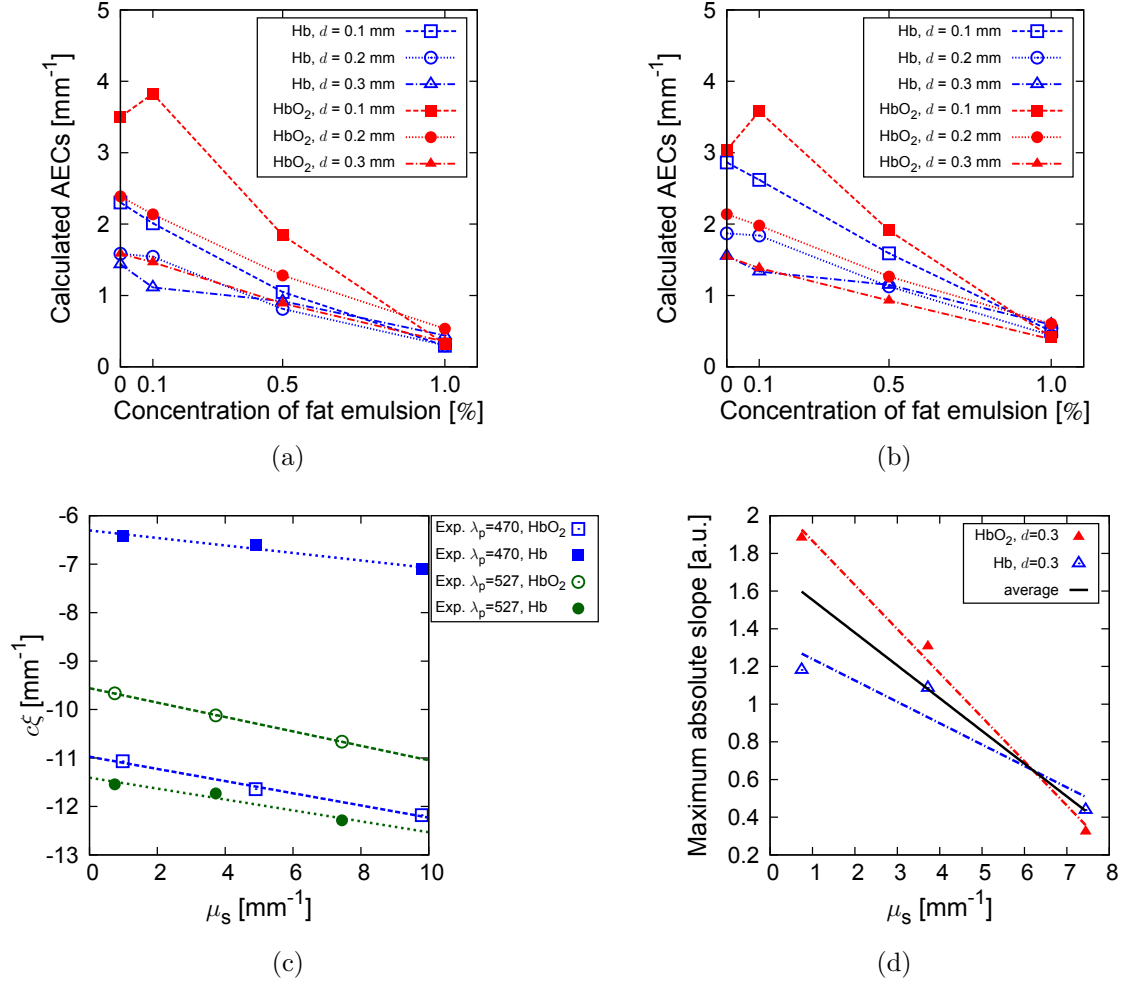


Fig 5.5: AECs of oxygenated and de-oxygenated hemoglobin obtained using the turbid phantoms. (a) and (b) The AEC versus the concentration of fat emulsion for bovine blood for LED sources of (a) 470 nm peak wavelength and (b) 527 nm peak wavelength. (c) The influence  $\xi$  on the AECs due to the scattering by surrounding tissue for the experiments and the simulation. Solid lines represent the fitting results obtained with a linear function. (d) The relation between the maximum absolute slope and the scattering coefficient of the phantoms with a 300  $\mu$ m diameter glass tube.

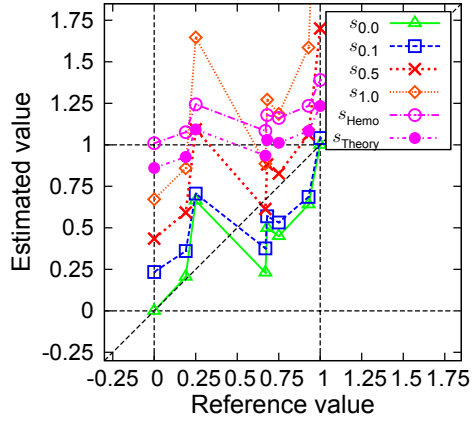
Table 5.1: The AAE [%] of estimated values.

phantom	AECs used						
fat emulsion	Measured from a turbid phantom						Correction
content	$s_{0.0}$	$s_{0.1}$	$s_{0.5}$	$s_{1.0}$	$s_{\text{Hemo}}$	$s_{\text{Theory}}$	method
0.0%	27.3	24.9	28.5	66.1	58.5	43.5	22.7
0.1%	42.8	30.0	18.3	34.4	50.7	35.7	14.6
0.5%	67.1	38.1	17.7	7.7	40.9	25.9	11.4
1.0%	93.1	51.2	32.8	11.2	33.6	21.4	18.8

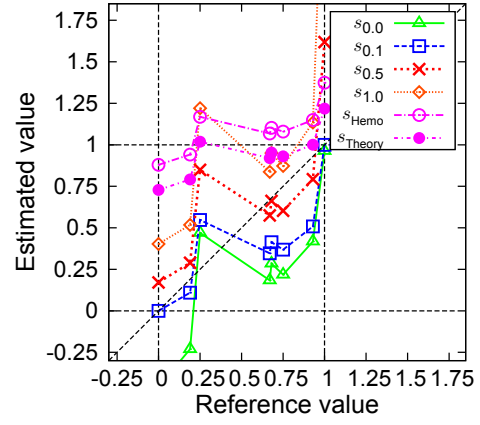
93%.

As shown in Table 5.1, in case that AECs determined from phantoms with a similar concentration of scatterers were used, the absolute average error (AAE) of the results was smaller. For example, for 0.5% and 1.0% phantoms, the AAE was less than 20%. There was an especially large error when  $\text{SO}_2$  of blood within a 1.0% phantom was estimated using the 0.0% phantom AECs, the AAE of  $s_{0.0}$  was more than 90%. When the AEC used is not suitable, the influence of the scattering causes an error in measurement of  $\Psi$  and the error of the estimated value increases. In  $s_{\text{Hemo}}$  and  $s_{\text{Th}}$ , although the results of  $s_{\text{Th}}$  were more accurate than those of  $s_{\text{Hemo}}$  in the same manner as the previous study [47], both absorption coefficients led to a greater estimation than the AECs did. By comparing estimation results with AECs measured from the phantoms and  $s_{\text{Th}}$ , we also found that the AAE could be reduced by 16.2% for a 0.0% phantom at the maximum and 5.7% for a 0.1% phantom at the minimum. This means that the good performance of the SDF oximetry requires correction for the influence of the tissue scattering. For glass tubes with a 200  $\mu\text{m}$  diameter, we also found the good performance of the SDF oximetry with correction for the influence of the tissue scattering. In this study, we clarified that the tissue scattering had a great impact on the SDF oximetry.

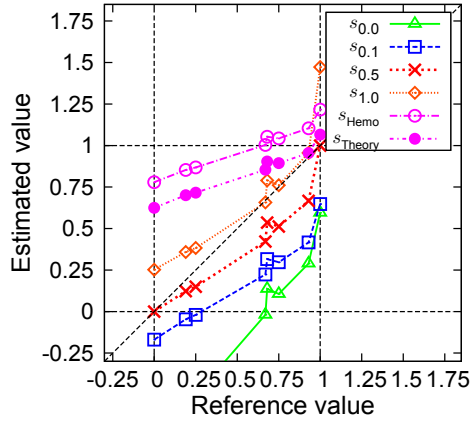
We show results using our scattering correction method in Fig. 5.7. Figures 5.7(a) and 5.7(b) show results of the estimation of the scattering coefficient of the phantoms from the average maximum absolute slope and the  $\text{SO}_2$  estimation from the estimated scattering coefficients. The AAE of the estimation is shown in 5.1. From the results, by using our method, the accuracy was improved compared to both estimation results with the extinction coefficients at the peak wavelength and non-corrected AECs.



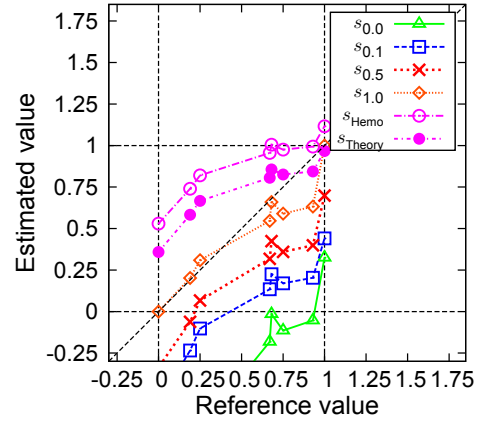
(a)



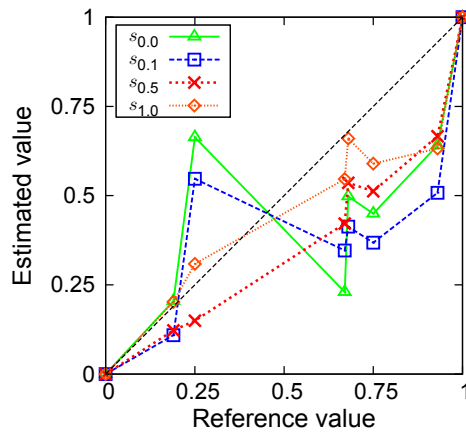
(b)



(c)



(d)



(e)

Fig 5.6:  $\text{SO}_2$  estimation results using six types of extinction coefficients for turbid phantoms of (a) 0.0% (b) 0.1% (c) 0.5% (d) 1.0% fat emulsion with the glass tube of  $300 \mu\text{m}$  diameter. (e) Estimation values using the suitable AECs extracted from the results of (a) to (d).

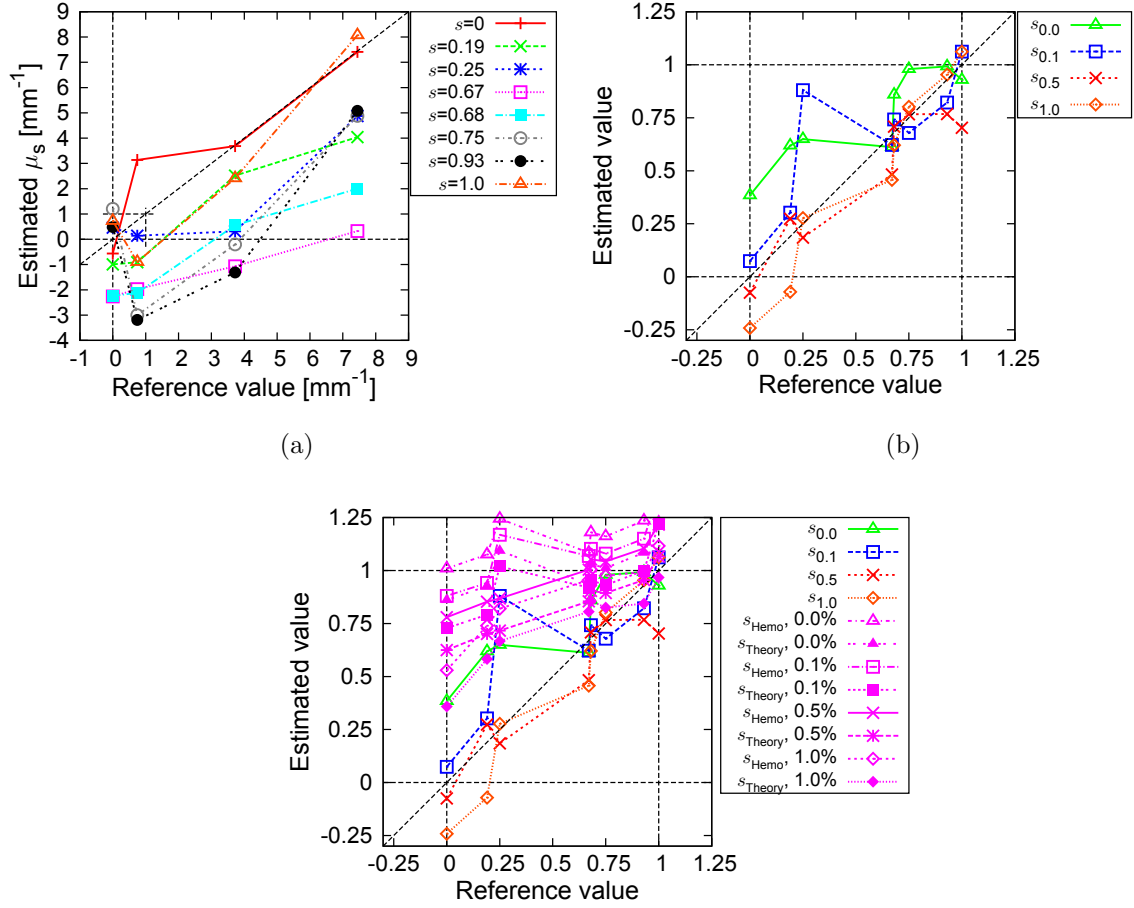


Fig 5.7: SO<sub>2</sub> estimation results using our scattering correction method. (a) Results of the estimation of the scattering coefficient from the average maximum absolute slope. (b) Results of SO<sub>2</sub> estimation using our correction method. (c) Comparison of (b) to results using the extinction coefficient at the peak wavelength and AECs without the scattering correction.



# Chapter 6 *IN VIVO* ANIMALS EXPERIMENTS

To understand the distribution of oxygen transportation in microcirculation,  $\text{SO}_2$  maps were produced from SDF images. In this chapter, we introduce a proposed method for producing an  $\text{SO}_2$  map. We performed animal experiments shown in § 6.1. To produce the maps, we proposed the method of a blood vessel extraction for an SDF image and the procedure of producing  $\text{SO}_2$  maps in § 6.2. The produced  $\text{SO}_2$  maps and results of the investigated oxygen transportation are shown in § 6.3.

## 6.1 Setups of experiments

Rat and pig small intestines were used in this study as *in vivo* experiments. Figure 6.1 shows SDF images of pig's stomach and colon. The reason why a small intestine was chosen is that both clear and dense blood vessels images can be obtained. In other digestive organs, a stomach is covered by the peritoneum having a structure such a foam and a colon has both thin and sparse blood vessels as compared to ones of a small intestine. Male Slc:Wistar rats (260 ~ 280 gbw, 12 week-old) and a female pig (about 30 kgbw) were used. Each experimental environment is shown in Fig. 6.2(a) for rats and Fig. 6.2(b) for pigs. For both animals, a protocol was as follows: an animals was anesthetized with isoflurane (Escain, Pfizer, Tokyo, Japan) and made an incision in its abdomen. Then, a small intestine was pulled out and fixed on the top of the stage. Finally, the SDF probe was pressed against the surface of the small intestine and obtained SDF images.

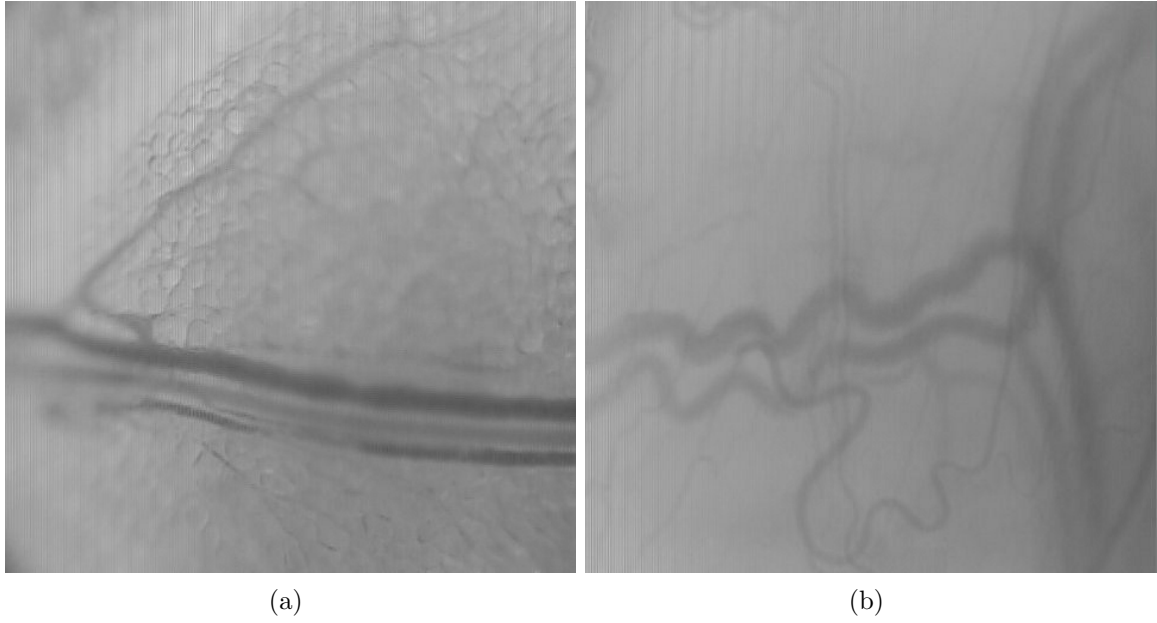


Fig 6.1: SDF images of pig's (a) stomach and (b) colon.

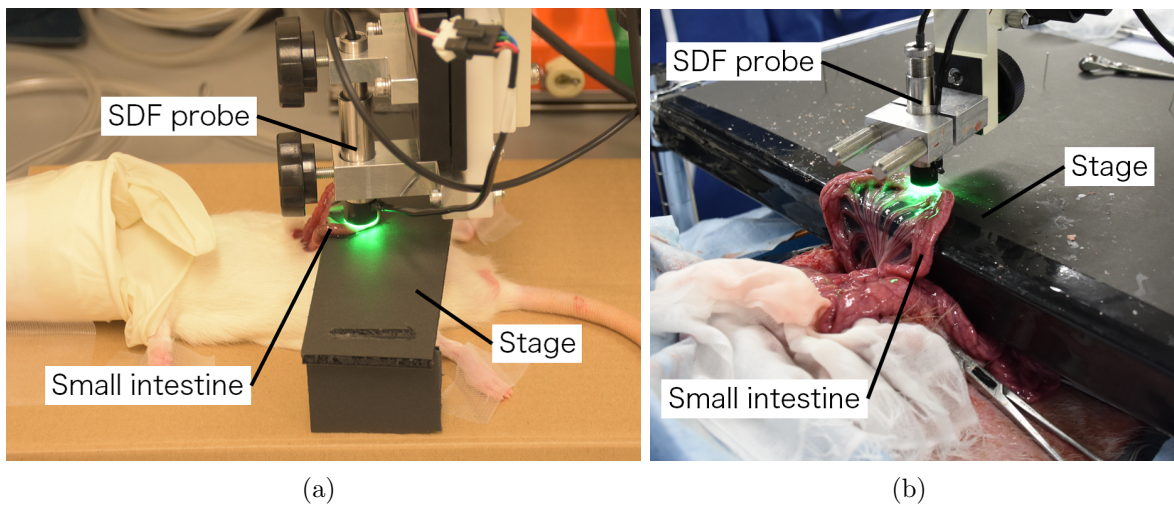


Fig 6.2: Environment of experiments *in vivo*. (a) A rats experiment. (b) A pigs experiment.

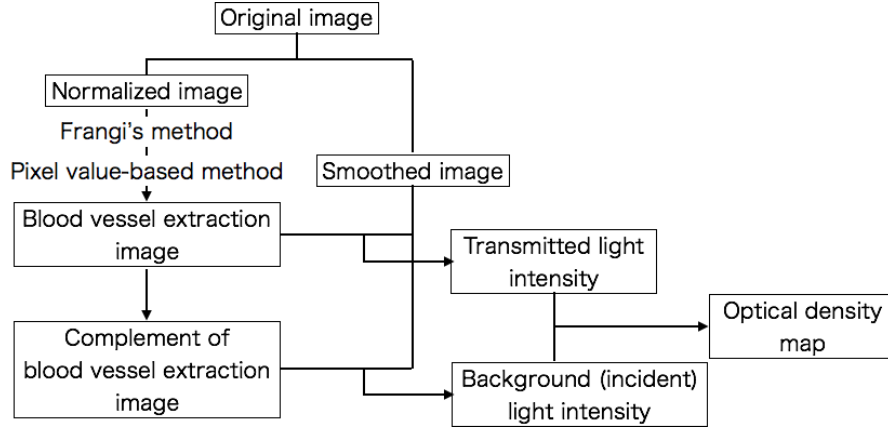


Fig 6.3: A flowchart of the image analysis for producing optical density map.

## 6.2 Image analysis

Figure 6.3 shows a flowchart of our image analysis to calculate an optical density distribution map for a band image. To generate  $\text{SO}_2$  distribution map, optical density maps of two-band images were used.

### 6.2.1 Normalization of an SDF image

As the first of all, in order to improve contrast of an original image for distinguishing blood vessel parts explicitly, normalization for each band image was performed. A pixel value at  $(x, y)$  of an SDF image,  $I = I(x, y)$ , is normalized by:

$$\bar{I} = (I - \beta_1) \frac{\alpha_2 - \alpha_1}{\beta_2 - \beta_1} + \alpha_1. \quad (6.1)$$

Here,  $\bar{I}$  is a normalized SDF image and coefficients,  $\alpha_1$ ,  $\alpha_2$ ,  $\beta_1$ ,  $\beta_2$ , are parameters, the lowest and highest pixel values:  $\beta_1 = \min_{x,y} I(x, y)$ ,  $\beta_2 = \max_{x,y} I(x, y)$ , respectively. In this study,  $\alpha_1$  and  $\alpha_2$  was fixed to 0 and 0.8, respectively.

### 6.2.2 Blood vessel extraction

As a vessel extraction method, combination of both the Frangi's method [79] and a pixel value-based method was used to a normalized SDF image.

As the first step, tube-like structure in an image was extracted using the Frangi's method. The Frangi's method is a multiscale Hessian-based one for extracting geometrical structures in an image. In this method, a normalized SDF image with a scale  $s$  is used. We first calculate eigen values of a Hessian matrix  $\mathcal{H}$ . The Hessian matrix of a normalized image  $\bar{I} = \bar{I}(x, y)$  is defined by:

$$\mathcal{H}(x, y) := \begin{pmatrix} \frac{\partial^2 \bar{I}}{\partial x^2} & \frac{\partial^2 \bar{I}}{\partial x \partial y} \\ \frac{\partial^2 \bar{I}}{\partial y \partial x} & \frac{\partial^2 \bar{I}}{\partial y^2} \end{pmatrix}. \quad (6.2)$$

The eigen values of  $\mathcal{H}$  at  $(x, y)$  are  $\lambda_1$  and  $\lambda_2$  ( $|\lambda_1| \leq |\lambda_2|$ ). If the structure of around  $(x, y)$  is a tubular, the eigen values satisfy the conditions:

$$\begin{aligned} |\lambda_1| &\sim 0, \\ |\lambda_1| &\ll |\lambda_2|. \end{aligned} \quad (6.3)$$

Reciprocals of  $\lambda_1$  and  $\lambda_2$  are represented half lengths of a major and minor axis of an ellipsoid, respectively. To quantify the structure, the indicator of quantification is defined by:

$$\begin{aligned} \mathcal{R}_B &= \frac{(\text{Area})/\pi}{(\text{Half length of major axis})^2} \\ &= \frac{1/(\lambda_1 \lambda_2)}{(1/\lambda_1)^2} = \frac{\lambda_1}{\lambda_2}. \end{aligned} \quad (6.4)$$

If the structure of around  $(x, y)$  is tubular,  $\mathcal{R}_B$  is approximately zero. To distinguish between a blood vessel part and a background part, the derivative of pixel values is used. The Frobenius norm of  $\mathcal{H}$  was adopted as a matrix norm:

$$\mathcal{S} = \|\mathcal{H}\|_F = \sqrt{\lambda_1^2 + \lambda_2^2}. \quad (6.5)$$

By using two geometrical values defined in Eq. (6.4) and (6.5), the blood vessel extraction with an image with a scale  $s$  is performed using the following equation:

$$\mathcal{V}(s) = \begin{cases} 0, & \text{if } \lambda_2 > 0 \\ \exp\left[-\frac{\mathcal{R}_B^2}{2\beta^2}\right] \left(1 - \exp\left[-\frac{\mathcal{S}^2}{2c^2}\right]\right), & \text{otherwise.} \end{cases} \quad (6.6)$$

Here,  $\beta$  and  $c$  are control parameters. In this study,  $\beta$  was set to 10 in accordance with Frangi's study [79] and  $c$  was set to the half value of the maximum Hessian norm:

$$c = \frac{1}{2} \|\mathcal{H}\|_{\max} = \frac{1}{2} \max_{ij} \{h_{ij}\}, \quad (6.7)$$

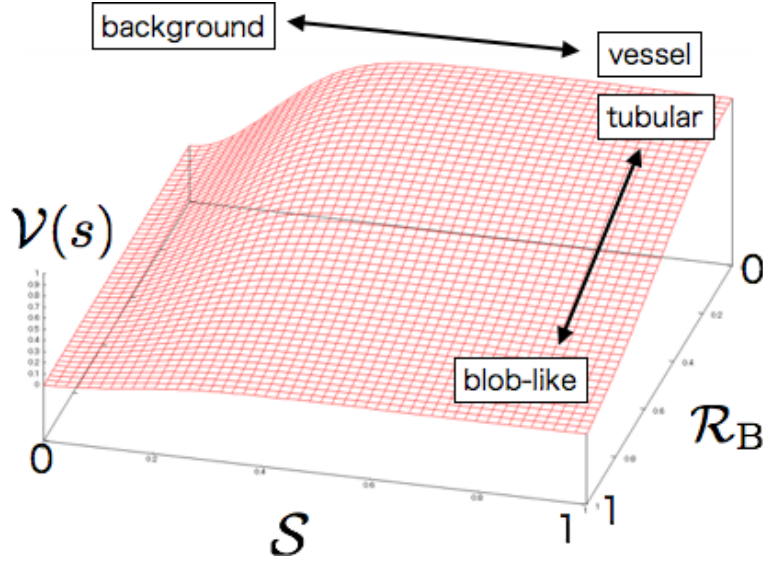


Fig 6.4: The outline of  $\mathcal{V}(s)$ .

where  $\|\mathcal{H}\|_{\max}$  is the maximum Hessian norm and  $h_{ij}$  represents a component of  $\mathcal{H}$ . Note that  $\mathcal{V}(s, x, y)$  has a greater value if the structure of around  $(x, y)$  is like a tubular and not in a background part since the ratio of eigen values is approximately zero and the derivative is not small. Figure 6.4 shows the outline of  $\mathcal{V}(s)$  as a function of  $\mathcal{S}$  and  $\mathcal{R}_B$ .

The tube-like structure image  $\mathcal{V}_F(x, y)$  using multiscale images is produced by use of the maximum value in each location among scaled images:

$$\mathcal{V}_F(x, y) = \max_{s_{\min} \leq s \leq s_{\max}} \mathcal{V}(s, x, y). \quad (6.8)$$

The use of multiscale images allows extracting both thin and thick blood vessels.

On the other hand,  $\mathcal{V}_F = \mathcal{V}_F(x, y)$  does not include all parts of blood vessel since parts of overlap with blood vessels cannot be distinguished from a tubular. As the second step, we therefore performed pixel value-based blood vessel extraction method in addition to Frangi's method. The binarization of  $\mathcal{V}_F$  using a threshold  $t$  is performed by:

$$\mathcal{V}_{\text{bin}}(x, y) = \begin{cases} 1, & \text{if } \mathcal{V}_F(x, y) \leq t \\ 0, & \text{otherwise.} \end{cases} \quad (6.9)$$

In this study,  $t$  was fixed to 0.05. The set of locations of non-zero in  $\mathcal{V}_{\text{bin}}$  is defined by:  $V'_F := \{(x', y') | \mathcal{V}_{\text{bin}}(x, y) = 1\}$ .  $V'_F$  represents the region of blood vessel parts extracted by the

Frangi's method and the complement of  $V'_F$  is defined as  $B$ . Next, the average pixel value of an original image  $I$  at  $(x', y') \in V'_F$  is set to a threshold for the blood vessel extraction:

$$I_{\text{threshold}} := \frac{1}{N} \sum_{(x,y) \in V'_F} I(x, y). \quad (6.10)$$

The pixel value-based blood vessel extraction using  $I_{\text{threshold}}$  over  $(x, y) \in B$  in an original image is performed by:

$$\mathcal{V}'(x, y) = \begin{cases} 0, & \text{if } I(x, y) > I_{\text{threshold}}(x, y) \\ 1, & \text{if } I(x, y) \leq I_{\text{threshold}}(x, y) \end{cases} \quad (6.11)$$

Finally, the blood vessel extraction image is defined by:

$$\mathcal{V} = \mathcal{V}_{\text{bin}} \cup \mathcal{V}'. \quad (6.12)$$

A background part  $\mathcal{B}$  is defined as the complement of  $\mathcal{V}$ :

$$\mathcal{B} = \mathcal{V}^c = (\mathcal{V}_{\text{bin}} \cup \mathcal{V}')^c. \quad (6.13)$$

### 6.2.3 Optical density map and $\text{SO}_2$ map

In order to produce an  $\text{SO}_2$  map, we used optical density maps of two-band images. The optical density map  $D(x, y)$  in blood vessel parts is calculated by:

$$D(x, y) = -\log_{10} \left[ \frac{I(x, y)}{I_{\text{in}}(x, y)} \right], \quad (6.14)$$

where  $I_{\text{in}}(x, y)$  is the incident light intensity on the blood vessel at  $(x, y)$ .  $I_{\text{in}} = I_{\text{in}}(x, y)$  is calculated in two ways. The ways were as follows:

1.  $I_{\text{in}}(x, y)$  is fixed to the average pixel value of a background part throughout the image:

$$I_{\text{in}} = \frac{1}{M} \sum_{(x,y) \in \mathcal{B}} I(x, y), \quad (6.15)$$

where  $M$  is the number of pixels of  $\mathcal{B}$ .

2.  $I_{\text{in}}$  is set to the average pixel value of  $\mathcal{B}$  in a ROI at each position. Since the reflected light is irregular from the behind blood vessels, the incident light intensity is determined in each position. When a ROI is set be centered at  $(x, y)$ , the incident light intensity is defined by:

$$I_{\text{in}}(x, y) = \frac{1}{M'} \sum_{(x, y) \in \mathcal{B} \subset \text{ROI}} I(x, y), \quad (6.16)$$

where  $M'$  represents the number of pixel values of  $\mathcal{B}$  in a  $n \times n$  size of a ROI.

An  $\text{SO}_2$  map  $s(x, y)$  using both  $D_{\lambda_1}$  and  $D_{\lambda_2}$  of two bands of the peak-wavelength  $\lambda_1$  and  $\lambda_2$  is calculated by:

$$s(x, y) = \frac{\Phi(x, y) \cdot \varepsilon_{\text{Hb}}(\lambda_1) - \varepsilon_{\text{Hb}}(\lambda_2)}{\Delta\lambda_2 - \Phi(x, y) \cdot \Delta\lambda_1}, \quad (6.17)$$

where  $\varepsilon_{\text{Hb}}(\lambda)$  is an extinction coefficient of de-oxygenated hemoglobin at  $\lambda$  and  $\Delta\lambda$  is the difference of extinction coefficients of oxygenated and de-oxygenated hemoglobin:  $\Delta\lambda := \varepsilon_{\text{HbO}_2}(\lambda) - \varepsilon_{\text{Hb}}(\lambda)$ .  $\Phi(x, y)$  that is the ratio of  $D_{\lambda_1}(x, y)$  and  $D_{\lambda_2}(x, y)$  is defined by:

$$\Phi(x, y) := \frac{D_{\lambda_2}(x, y)}{D_{\lambda_1}(x, y)}. \quad (6.18)$$

$\Phi(x, y)$  is a measured value from two-band images.

## 6.3 Results

Objectives of experiments are as follows:

- producing an optical density map of each band image and then an  $\text{SO}_2$  map using two-band images,
- investigating the oxygen transportation using the  $\text{SO}_2$  map.

### 6.3.1 Blood vessel extraction from band images

The blood vessel extraction was performed using our technique. Figure 6.5 shows the results of the blood vessel extraction for an SDF image obtained under blue illumination. A original

image, a normalized image, Frangi's blood vessel extraction, a pixel value-based extraction is shown in Fig. 6.5(a), 6.5(b), 6.5(c), and 6.5(e), respectively. This data represent the thick of an arteriole and a venule that were parallel running and overlapping, and had the branch. Figure 6.5(d) is binarized Frangi's blood vessel extraction as shown in Fig. 6.5(c) and Fig. 6.5(f) is a result of the blood vessel extraction obtained by calculating the union of the result of both the Frangi's (Fig. 6.5(d)) and the pixel value-based method (Fig. 6.5(e)).

By using the normalizing procedure, arterioles and venules could be distinguished by differences in the shade as compared to the original image. This was because the peak wavelength of blue-color illumination sources is 470 nm in which there is a large difference between the light absorption of the  $\text{HbO}_2$  and Hb. Although Frangi's method allowed extracting blood vessels roughly, blood vessels overlap area could not be extracted. This area could be extracted by thresholding the pixel values of the original image using a threshold determined in the pixel value-based method. As a result, the blood vessel extraction was performed well by taking the union of results of both Frangi's and pixel value-based method as compared to a result produced by only Frangi's method.

Figures 6.6 and 6.8 show the results of the blood vessel extraction for an SDF image obtained and an optical density map under green illumination, respectively.

### 6.3.2 Optical density distribution map

Figures 6.7 and 6.8 show pseudo-color results of a transmittance map for the blue-band and green-band image, respectively. The transmittance map was obtained by applying the gamma correction shown in Chapter 2 to the original image shown in Figs. 6.7(a) and 6.6(a).

Figures 6.9 and 6.10 show the incident light intensity maps and the optical density maps for the blue and green band images. Figure 6.9 shows the results of use of the average pixel value as the incident light intensity. The incident light intensity map was produced by substituting the average pixel value for one in the blood vessel parts in  $\mathcal{B}$ . The average transmittance of blood vessel parts in Eq. (6.10) was  $I_{\text{threshold}} = 45.66\%$  and  $52.40\%$  and the incident light intensity in Eq. (6.15) was  $56.74\%$  and  $67.25\%$  for a blue and green image, respectively.

In the case of use of the average pixel value of ROIs as the incident light intensity, as shown in Figs. 6.10(a) and 6.10(b), we could correct the non-uniformity of the incident light intensity



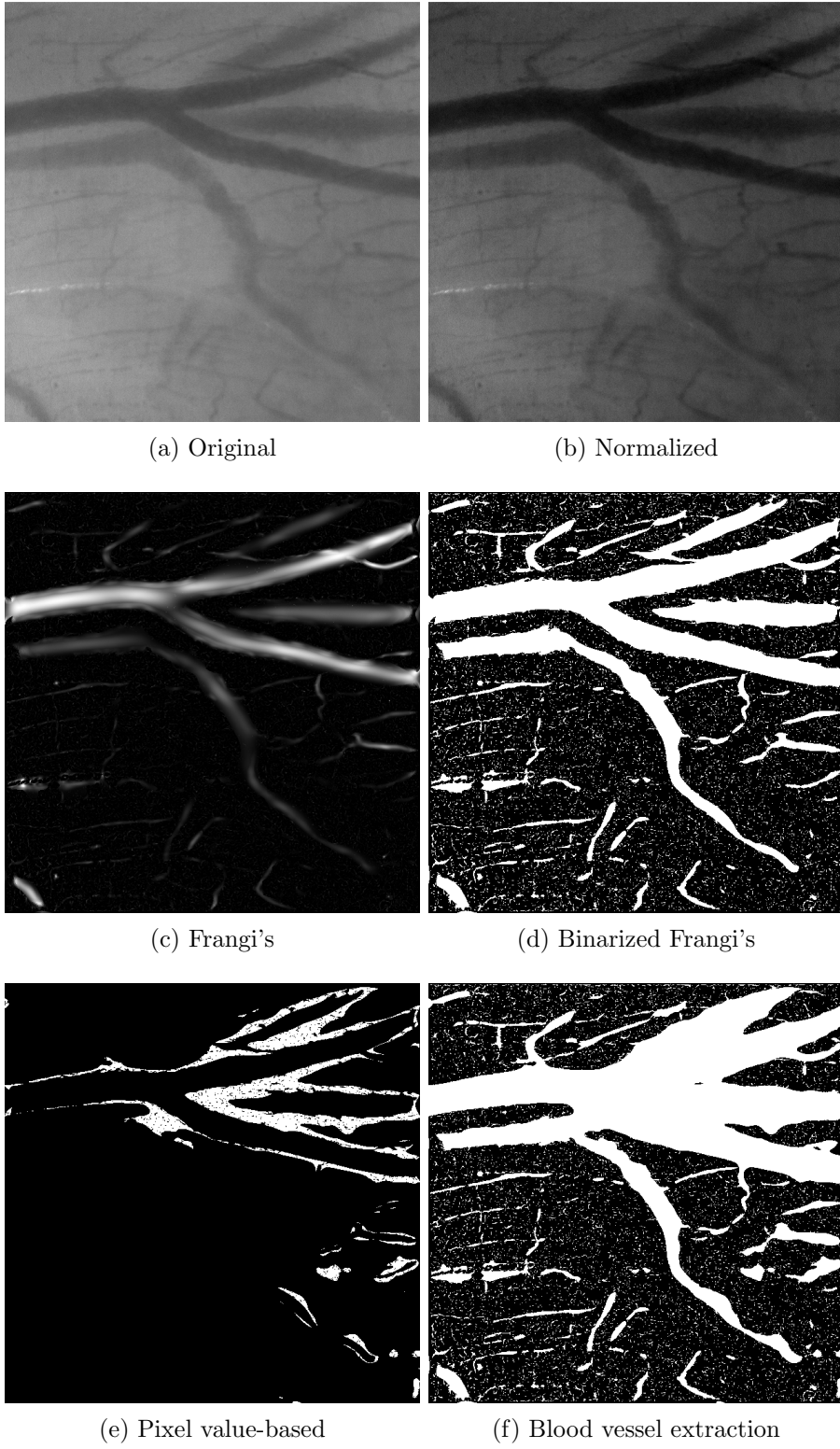


Fig 6.5: Results of the blood vessel extraction for a blue-band image.

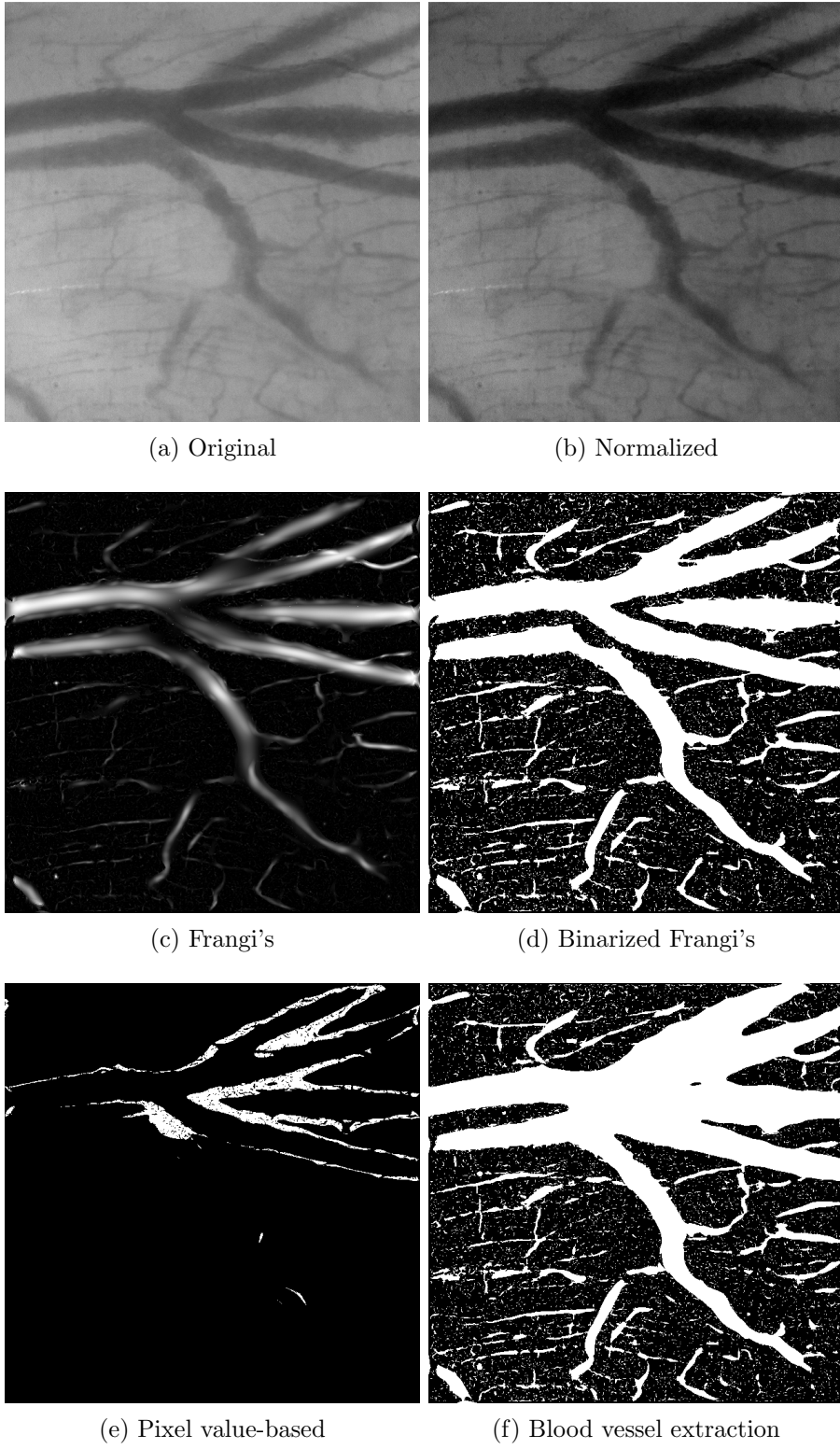
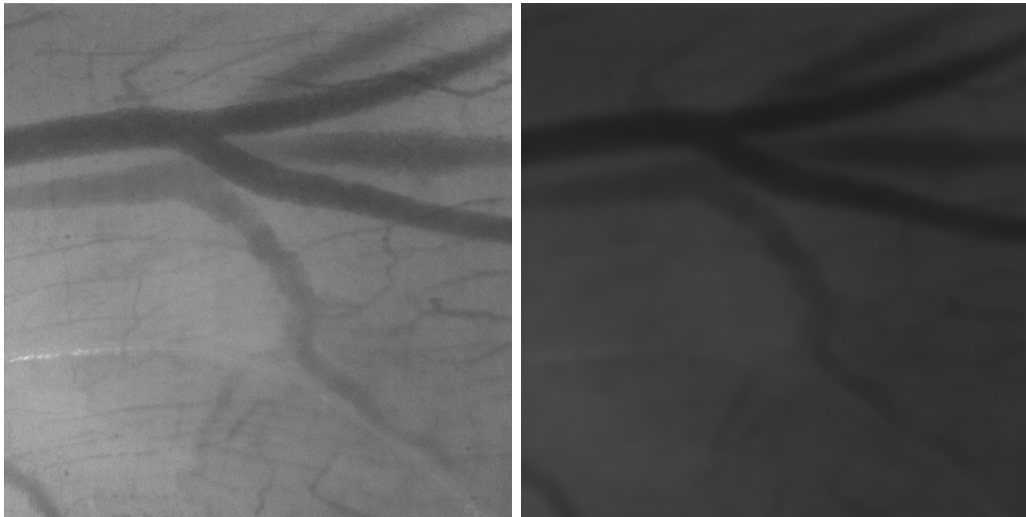
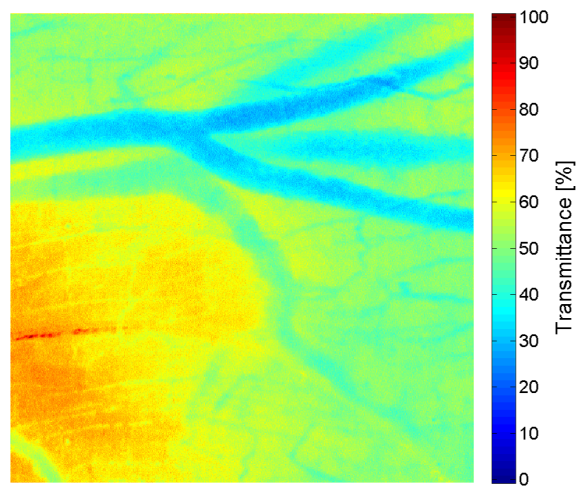


Fig 6.6: Results of the blood vessel extraction for a green-band image.



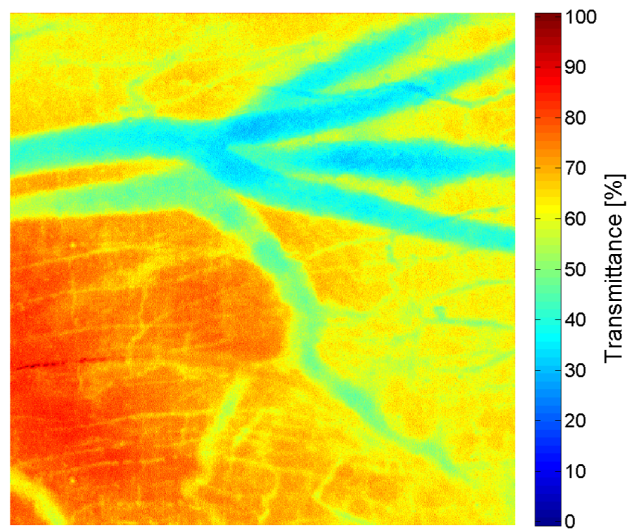
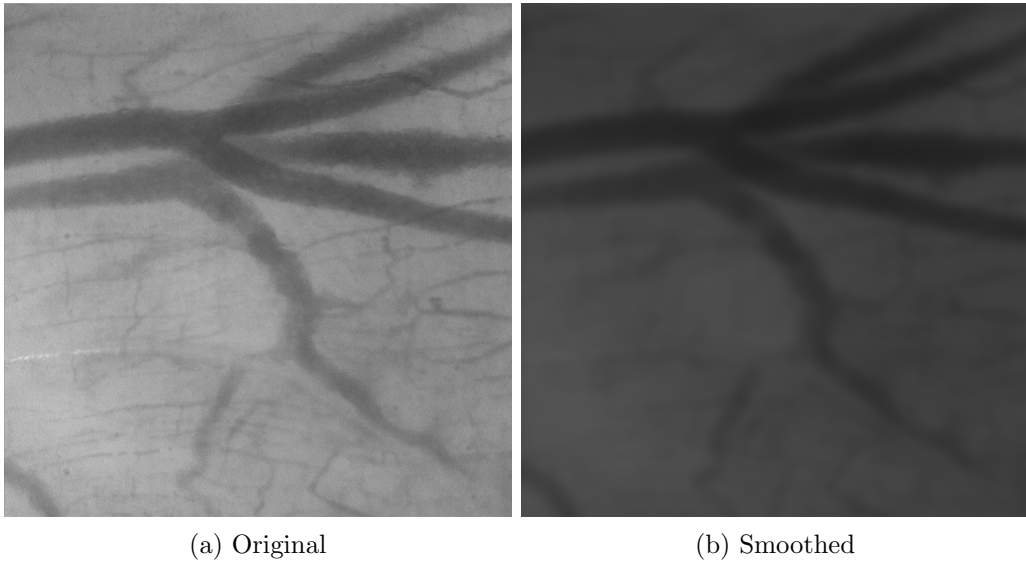
(a) Original

(b) Smoothed



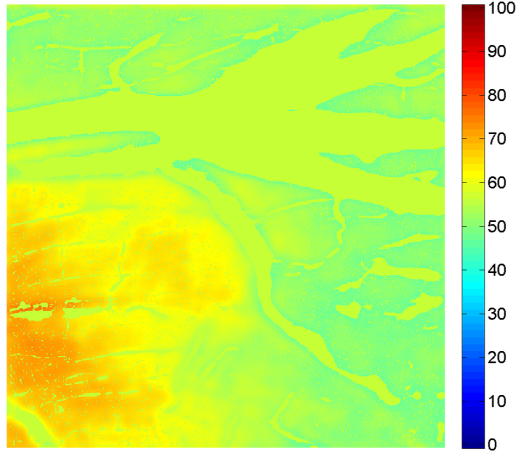
(c) Transmittance

Fig 6.7: The intensity image of the blue-band image. (a) The Original image. (b) A smoothed image obtained by filtering with the Gaussian filter. (c) The transmittance image with pseudo-color.

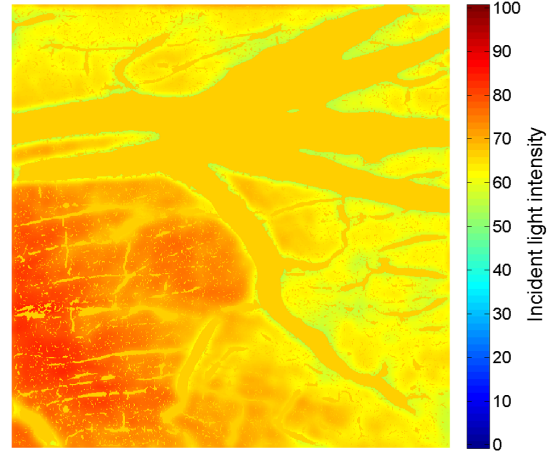


(c) Transmittance

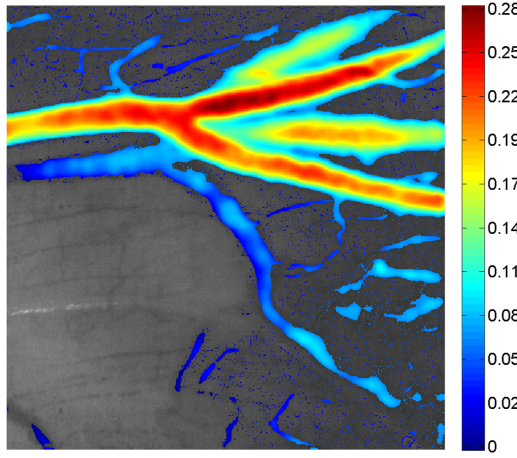
Fig 6.8: The intensity image of the green-band image. (a) The Original image. (b) A smoothed image obtained by filtering with the Gaussian filter. (c) The transmittance image with pseudo-color.



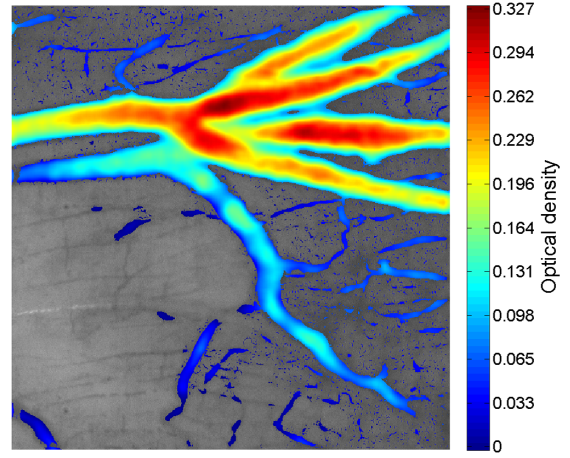
(a)  $I_{\text{in}}$  of blue-band



(b)  $I_{\text{in}}$  of green-band



(c)  $D$  of blue-band



(d)  $D$  of green-band

Fig 6.9: Incident light intensity maps and optical density maps obtained from the incident light intensity maps using the average pixel value of  $\mathcal{B}$  as the incident light intensity. The incident light intensity map of (a) a blue-band and (b) green-band image. The optical density map of (c) a blue-band and (d) green-band image.

as compared to Figs. 6.9(a) and 6.9(a). Furthermore, the optical density for the small blood vessels can be calculated.

### 6.3.3 SO<sub>2</sub> map

From the optical density maps of the blue and green band images, the distribution of  $\Psi$  in Eq. (6.18) is calculated and shown in Fig. 6.12. We consider the range that can be taken of  $\Psi$ . Since the peak-wavelength (527 nm) of a green-band region is isosbestic point, the optical densities calculated from the green-band image for arterioles and venules become roughly the same:  $D_{\text{arteriole}}(\lambda_{527}) \sim D_{\text{venule}}(\lambda_{527})$ . The optical density calculated from the blue-band image (the peak-wavelength: 470 nm) for arterioles is also roughly equal to one of the green-band image. For venules, the optical densities of the blue-band image satisfy the following relationship:  $D_{\text{arteriole}}(\lambda_{470}) \geq D_{\text{venule}}(\lambda_{470})$ . Thus, from Eq. (6.18),  $\Psi_{\text{arteriole}} \sim 1$  for arterioles and  $\Psi_{\text{venule}} \geq \Psi_{\text{arteriole}}$  for venules. As shown in Eq. (3.2), an optical density can be expressed using extinction coefficients. We evaluated the tend of  $\Psi$  over SO<sub>2</sub> using the extinction coefficients of 470 nm and 527 nm peak-wavelengths by:

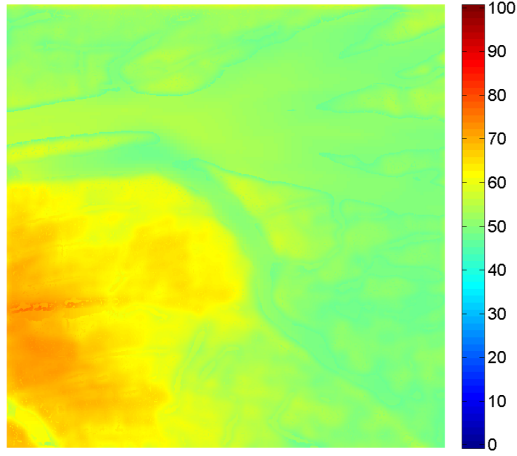
$$\begin{aligned}\Psi(s) &= \frac{\mu_a(\lambda_{527})}{\mu_a(\lambda_{470})} \\ &= \frac{s\varepsilon_{\text{HbO}_2}(\lambda_{527}) + (1-s)\varepsilon_{\text{Hb}}(\lambda_{527})}{s\varepsilon_{\text{HbO}_2}(\lambda_{470}) + (1-s)\varepsilon_{\text{Hb}}(\lambda_{470})}.\end{aligned}\tag{6.19}$$

Figure 6.11 shows SO<sub>2</sub>-dependence of  $\Psi$ . From Fig. 6.12, we could distinguish between arterioles and venules on the basis of  $\Psi$ . Compared Fig. 6.12(a) with Fig. 6.12(b), we found that  $\Psi$  could be calculated in small blood vessels in Fig. 6.12(b).

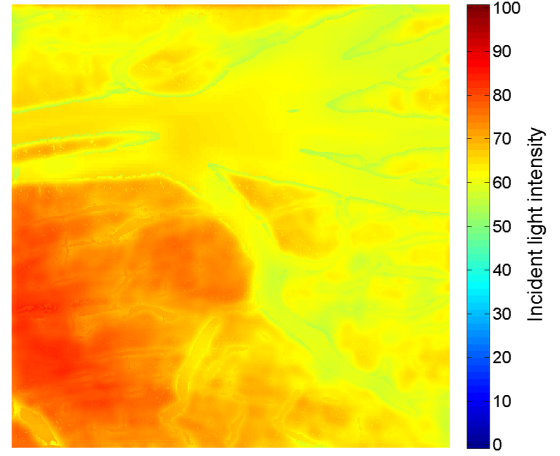
The SO<sub>2</sub> distribution map produced by using  $\Psi$  is shown in Figs. 6.13 and 6.14. Figure 6.13 represents results of  $\Psi$  using the average pixel value of  $\mathcal{B}$  as the incident light intensity shown in 6.12(a) and Fig. 6.14 represents the ones of  $\Psi$  shown in Fig. 6.12(b). In each result, as extinction coefficients, ones of the peak-wavelengths and AECs were used. We also show two types of the SO<sub>2</sub> map: the map with a range of  $[0, 1]$  and the relative SO<sub>2</sub> map. The relative SO<sub>2</sub> map is defined by the ratio of the maximum value in the SO<sub>2</sub> map with a range of  $[0, 1]$ :

$$s_{\text{relative}}(x, y) = \frac{s(x, y)}{\max_{(x, y)} s(x, y)}.\tag{6.20}$$

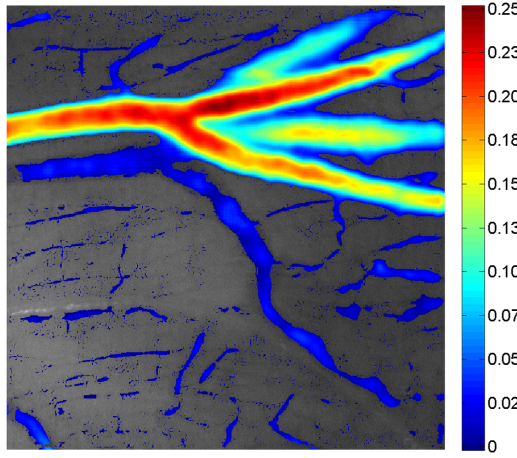




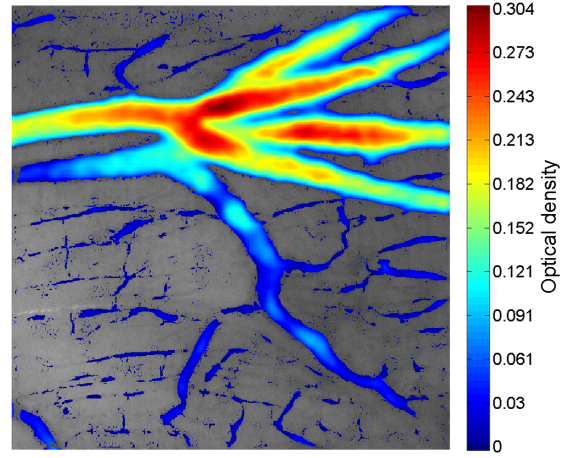
(a)  $I_{\text{in}}$  of blue-band



(b)  $I_{\text{in}}$  of green-band



(c)  $D$  of blue-band



(d)  $D$  of green-band

Fig 6.10: Incident light intensity maps and optical density maps obtained from the incident light intensity maps using the average pixel value of ROIs as the incident light intensity. The incident light intensity map of (a) a blue-band and (b) green-band image. The optical density map of (c) a blue-band and (d) green-band image.

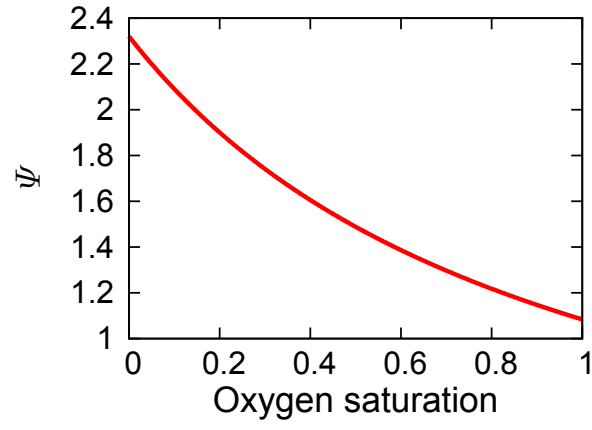


Fig 6.11: The  $\text{SO}_2$ -dependence of  $\Psi$ .

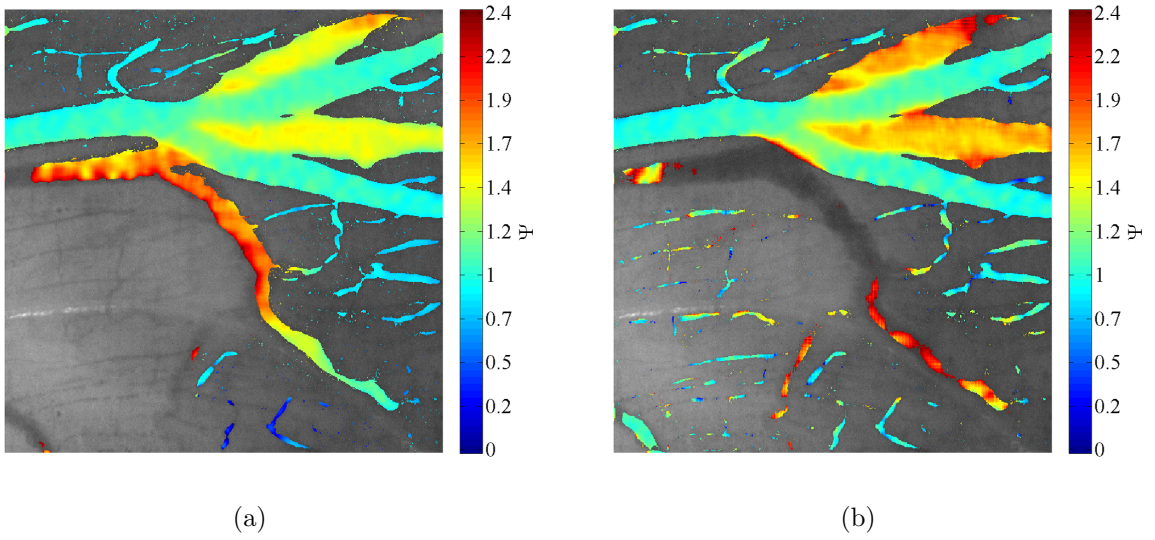


Fig 6.12: The distribution of  $\Psi$  from (a) Figs. 6.9(c) and 6.9(d) and (b) Figs. 6.10(c) and 6.10(d).



Figures 6.13(a), 6.13(b), 6.14(a), and 6.14(b) show the maps using the extinction coefficients of the peak-wavelength shown in Fig. 1.3 in Chapter 1. Figures 6.13(c), 6.13(d), 6.14(c), and 6.14(d) show the maps using AECs.

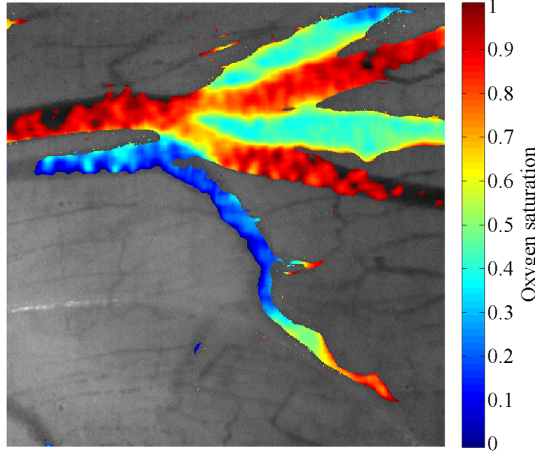
We could produce the  $\text{SO}_2$  maps of microcirculation from SDF images. As shown in Fig. 6.14, using the incident light intensity of ROIs,  $\text{SO}_2$  could be estimated in small blood vessels. The results using extinction coefficients at the peak-wavelength were higher than ones using AECs. This was corresponding to results of the numerical simulation shown in Chapter 4. We could not find the differences of Figs. 6.13 and 6.14 for estimated values. On the other hand, the incident light intensity of ROIs was reasonable to correct the unevenness of the reflected light from behind the blood vessels. However, the blue and green-band images were not obtained simultaneously. The time interval of obtaining images is a range from 30 ms to 100 ms. During the interval, we considered the possibility of artifacts due to blood flow and the body movement though the motion artifacts such as the deviation of the rigid deformation were corrected with the template matching technique. These artifacts were reported in [82].

### 6.3.4 Analysis of oxygen saturation transportation

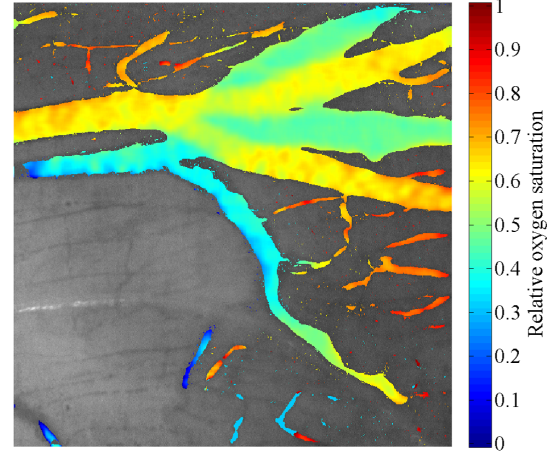
We analyzed the oxygen transportation using  $\text{SO}_2$  maps. As a way to investigate the oxygen transportation, we referred to the study [46]. The oxygen transportation is evaluated by the variation of  $\text{SO}_2$  along a blood vessel. The positions to be measured  $\text{SO}_2$  is defined by points on the skeleton obtained from the blood vessel extraction image. The skeleton was produced by the Voronoi-based technique. The code of the Voronoi diagram was used Qhull (2015. 2 for Windows 10, 8, 7, XP, and NT) [80]. In addition to the above, we evaluated the distribution of  $\text{SO}_2$  along a cross section.

We used the relative  $\text{SO}_2$  map shown in Fig. 6.14(d). The variation of  $\text{SO}_2$  along the blood vessel is shown in Fig. 6.15. We found that reduction of  $\text{SO}_2$  by about 20% along the flow of blood. The decrease of  $\text{SO}_2$  agreed with the previous study [46, 81]. The variation of  $\text{SO}_2$  along a cross section of the blood vessel is shown in Fig. 6.16.

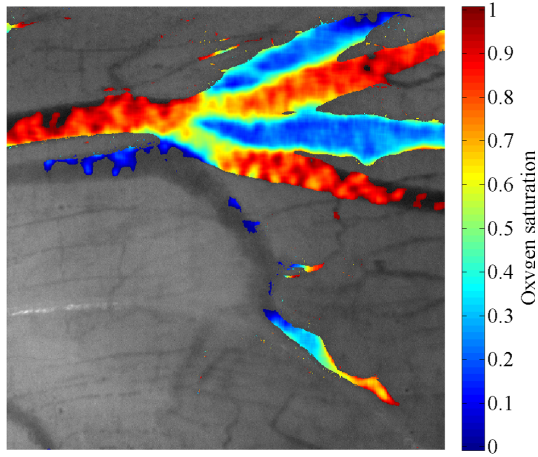
We investigated the oxygen transportation in a branch of blood vessels of the pig small intestine. As shown in Fig 6.17(a). we produced the relative  $\text{SO}_2$  map and chose a branch. This blood vessel was regarded as a venule based on the flow. This vessel was one to join



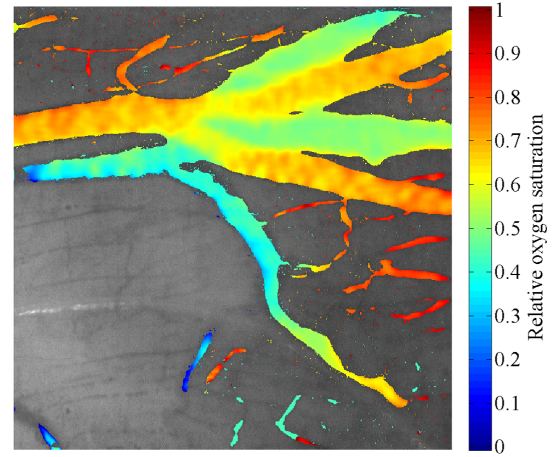
(a)



(b)



(c)



(d)

Fig 6.13: The  $\text{SO}_2$  distribution map using  $\Psi$  shown in Fig. 6.12(a). (a and b) Maps using the extinction coefficients of the peak-wavelengths. (c and d) Maps using AECs. (a and c) A range of  $[0, 1]$  of  $\text{SO}_2$ . (b and d) The relative  $\text{SO}_2$  maps.

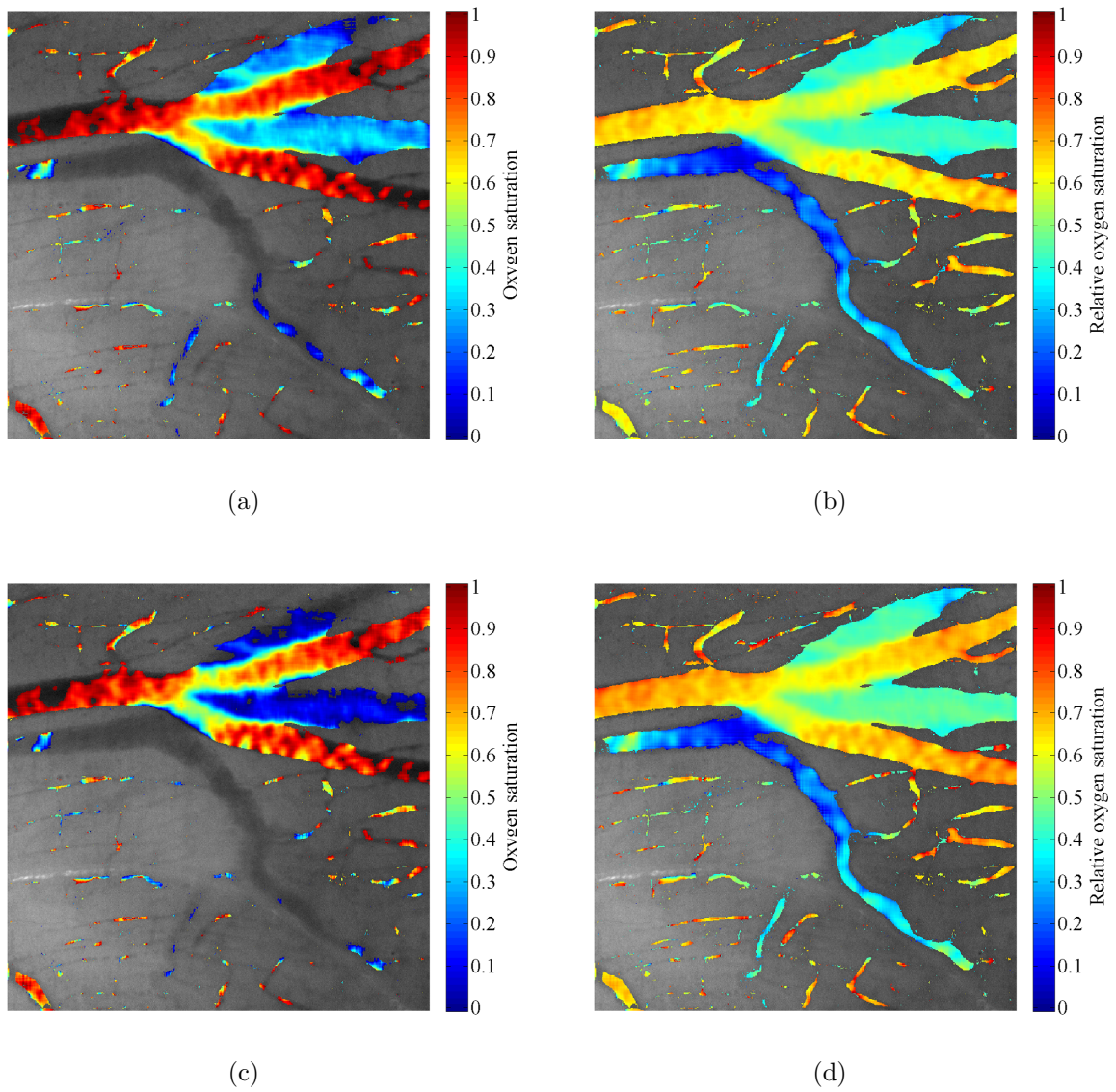


Fig 6.14: The SO<sub>2</sub> distribution map using  $\Psi$  shown in Fig. 6.12(b). (a and b) Maps using the extinction coefficients of the peak-wavelengths. (c and d) Maps using AECs. (a and c) A range of  $[0, 1]$  of SO<sub>2</sub>. (b and d) The relative SO<sub>2</sub> maps.

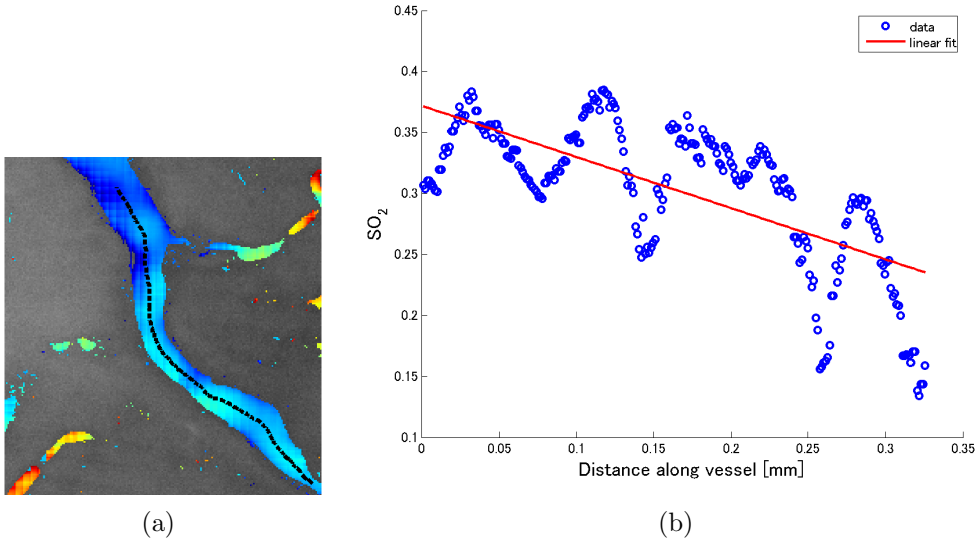


Fig 6.15: The variation of  $SO_2$  along the blood vessel. (a) The positions to be measured  $SO_2$  is depicted by a black dashed line. (b) The  $SO_2$  along the blood vessel. Blue points represent the data and a red line represents the fitting result.

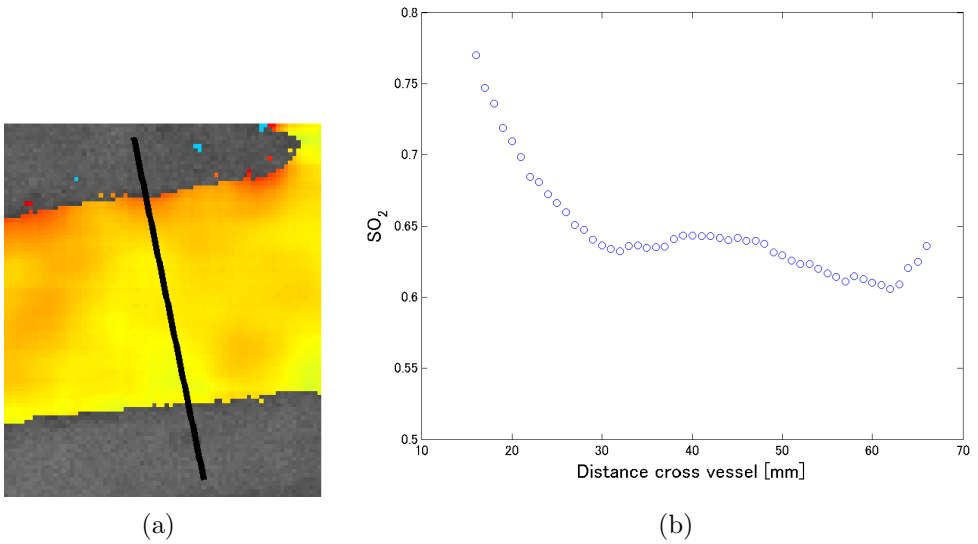


Fig 6.16: The variation of  $SO_2$  along a cross section of the blood vessel. (a) The positions to be measured  $SO_2$  is depicted by a black solid line. (b) The  $SO_2$  along the blood vessel. Blue points represent the data.

two of the blood flow. Results of the oxygen transportation along the vessel are shown in Figs. 6.17(c) and 6.17(e). Both results are converged to 74% by confluence of the blood flow.

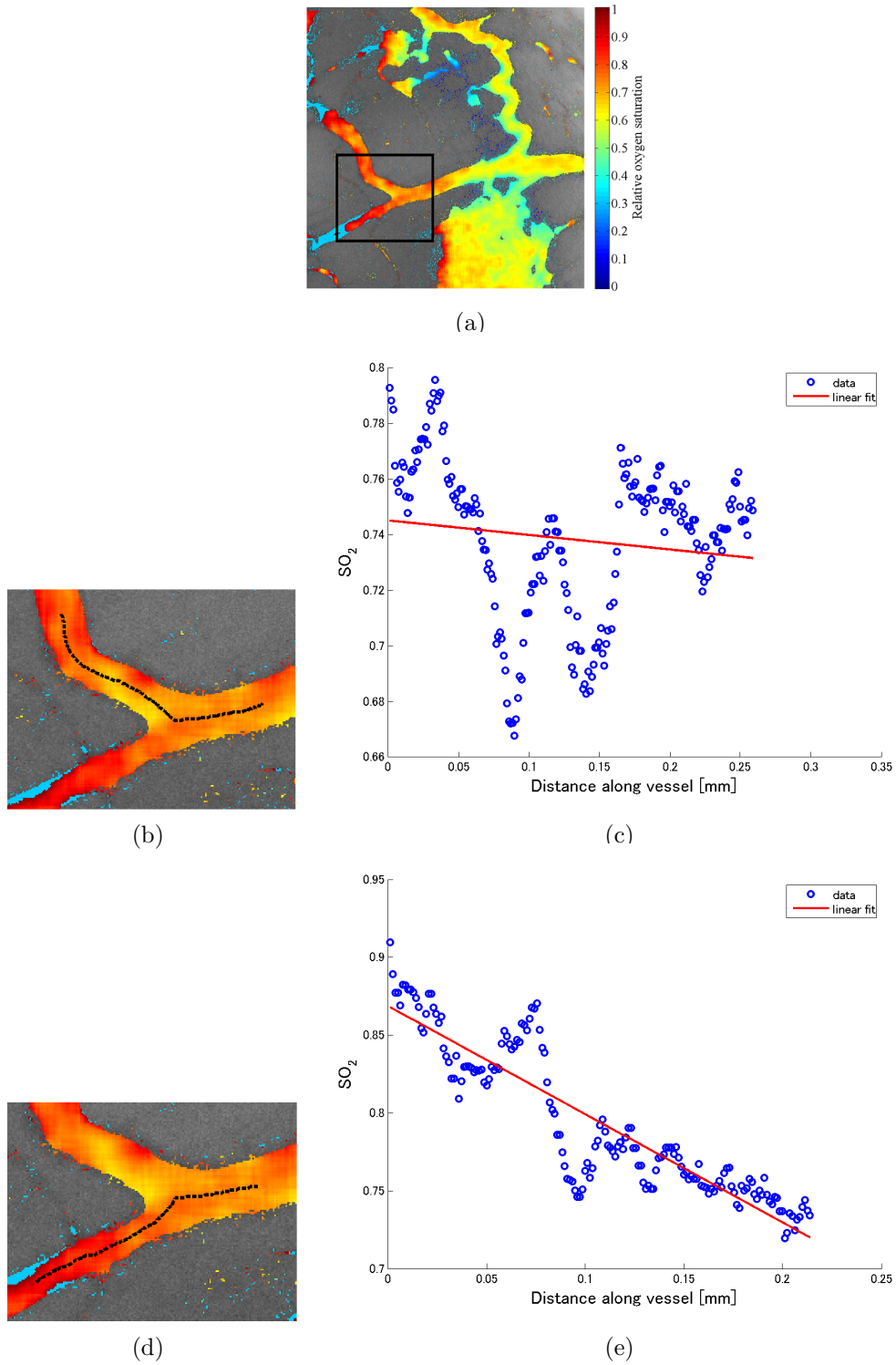


Fig 6.17: Oxygen transportation at a branch of the vessel. (a) Relative SO<sub>2</sub> map of the pig small intestine. (b and d) Locations of SO<sub>2</sub> estimation. (c and e) The variation of SO<sub>2</sub> along the black line shown in (b) and (d), respectively.

# Chapter 7 CONCLUSIONS

In this study, we have proposed the SDF oximetry method and performed the experiments to establish the SDF oximetry. In § 7.1, we summarize our proposed oximetry method that is SDF image-based one. We performed approaches to evaluate the validity of the SDF oximetry. As the first approach, we performed the Monte Carlo photon propagation approach as summarized in § 7.2. After that, the biological tissue-like phantom experiments was conducted as summarized in § 7.3. In addition to the above, we performed to produce  $\text{SO}_2$  maps as summarized in § 7.4. At the end of this Chapter, we show the issues of this study in § 7.5.

## 7.1 Proposal of SDF oximetry method

We have proposed an  $\text{SO}_2$  estimation method for individual blood vessels in microcirculation using band images obtained by SDF imaging. As the first approach, we investigated the structure of tissues and location of blood vessels in microcirculation to understand the light propagation in a pig's small intestine which is one of the target tissue by OCT and HE stained specimen. We clarified the location of the target blood vessels and the structure of the tissue. In SDF imaging, the light that is scattered in muscularis, submucosa, or mucosa is obtained with an imaging camera. Thus, we assumed that absorption of the intensity of the light that goes through the blood vessels follows the Lambert-Beer law. This  $\text{SO}_2$  estimation method using band SDF images is called SDF oximetry. Moreover, modified extinction coefficients were proposed to correct both the bandwidth of light illumination sources and characteristics of the imaging camera for spectroscopy. These extinction coefficients were defined as the average extinction coefficients (AECs). However, the above method does not include the scattering by tissues surrounding the target blood vessels. The contrast of the blood vessel parts in SDF images are affected by the tissue scattering. Thus, we were focus on the maximum slope of the intensity profile of the blood vessel as a feature value and proposed a correction method

for the tissue scattering. We then modified AECs by adding the term of the tissue scattering correction. Our correction method uses the relationship between the tissue scattering and the correction term to correct AECs. The proposed method uses the average of the maximum absolute slope calculated from an SDF image and determine the scattering correction term of the AECs.

To obtain band images for spectroscopy, we developed the SDF probe using multicolor LEDs. Spectral band images can be obtained by changing the color of the LEDs. Using our SDF probe, we can obtain continuously images of microcirculation. The peak-wavelengths of the multicolor LED are 470 nm (blue color), 527 nm (green), and 624 nm (red). In this study, we used blue- and green-color LEDs for SDF oximetry.

## 7.2 Photon propagation simulation

As an initial study, we have investigated the validity of an  $\text{SO}_2$  estimation of individual blood vessels by the Monte Carlo photon propagation simulation where two image-based methods (EPW and AEC) were compared with the intensity method (PLB). We also investigated the influence of both bandwidth of illumination sources and diameter of a target blood vessel. As an experiment, we performed the simulation with illumination sources from  $w = 0$  nm to 50 nm at 10 nm intervals and the tissue model with vessel diameter  $d = 100, 200$ , and  $300 \mu\text{m}$ .

There were strong correspondences between PLB and the image-based methods. The SEE of AEC was especially similar to the SEE of PLB. In the EPW, the SEE was an increasing function with respect to  $d$  and  $w$ . On the other hand, in the PLB and AEC, the errors were not a monotone function. In addition, for all conditions, AEC was more accurate than EPW, hence using AECs of hemoglobin is effective for the SDF oximetry with narrowband illumination sources such as LEDs.

We also investigated the influence of the scattering by a medium surrounding the target blood vessel in the simulation approach. As a result, we found that absolute average error (AAE) was increased with increase of the concentration of the scatterers within a medium. Our proposed tissue scattering correction method allowed reducing AAE.



### 7.3 Biological tissue phantom experiments

We have investigated the influence of tissue scattering for our SDF oximetry method and proposed a correction method for the scattering using turbid phantoms. We used the developed SDF probe and conducted experiments with phantoms that made from agar, fat emulsion, and blood-filled glass tubes. The phantoms simulated tissues such as biological tissues and blood vessels. We made four turbid phantoms using 0.0, 0.1, 0.5, or 1.0% fat emulsion, and glass tubes of three different inner diameters, 100, 200, and 300  $\mu\text{m}$  and determined the AECs of oxygenated and de-oxygenated hemoglobin.

We found the influence of the decrease of the AECs with the increase of the concentration of fat emulsion included in the phantom body. We also validated the decrease using a Monte Carlo photon propagation simulation. After that, we performed the  $\text{SO}_2$  estimation experiment with bovine blood having controlled  $\text{SO}_2$  using six types of oxygenated and de-oxygenated hemoglobin extinction coefficients. As a result, we found that the AAE of the estimated values was smaller when using the appropriate AECs. We also found that the AAE could be reduced by 16.2% at the maximum using the appropriate AECs compared to AAE using the AECs without the tissue scattering. This means that the influence of the scattering by tissues must be considered for our SDF oximetry method. We also performed the  $\text{SO}_2$  estimation using our scattering correction method. As a result, by using the correction method, the AAE could be reduced to the same level as a result of using the appropriate AECs. Therefore, the correction method was more effective than methods without the scattering correction.

### 7.4 Animal experiments

We have produced  $\text{SO}_2$  distribution maps from two-band SDF images by our proposed SDF oximetry method. Rats and pigs experiment were performed *in vivo*. In this experiments, we used small intestines of them. As a method, the blood vessel extraction was performed using a proposed technique based on both the Hessian-based and the pixel value-based techniques. By our extraction method, we could obtain region of blood vessel parts from a SDF image. Using the results of the extraction, we produced several  $\text{SO}_2$  maps with assumptions of the incident light intensity and with extinction coefficients; extinction coefficients at peak-wavelength of

LEDs used and AECs without the scattering. We could obtain the  $\text{SO}_2$  map of individual blood vessels. The results were corresponding to arterioles and venules those were determined based on the blood flow from relative  $\text{SO}_2$  maps. However, the accuracy of the absolute values of the  $\text{SO}_2$  estimation was not confirmed. We must compare the value with estimated ones from other measurements with other modalities. In addition to the  $\text{SO}_2$  map production, using  $\text{SO}_2$  maps, we investigated the oxygen transportation along a blood vessel and a cross section. We found the variation in  $\text{SO}_2$ .

The mechanism of the oxygen transportation in microcirculation have been studied for many years [27, 28, 83]. The studies of this used approach of fluid dynamics to model the flow of blood. We are also interested in understanding by comparison with estimated values by our SDF oximetry and the above model.

## 7.5 Future issues

We investigated the validity of our proposed oximetry method in this study. However, there are several issues to establish our SDF oximetry and use in clinical and physiological research field. As a future issue, the major issues are the improvement of the accuracy of the  $\text{SO}_2$  estimation and the establishment of analytical ways. The conceivable issues are as follows:

- strict calculation of universal AECs as a function of the scattering coefficient or wavelengths,
- development of a correction method for depth of blood vessels,
- investigation of a feature value calculated from a SDF image instead of the maximum average slope of the intensity profile of a blood vessel.
- optimal wavelengths for SDF oximetry are chosen to correct the PE defined in § 4.2.3 in Chapter 4,
- investigation of spatial and sequential oxygen transportation.

We must calculate universal AECs strictly as a function of the scattering coefficient of tissues or wavelengths. After that, we will estimate intravascular  $\text{SO}_2$  of microvessels near

the surface of tissues of an animal *in vivo* using the AECs calculated by taking into account the influence of the tissue scattering. However, to do so, we need to consider the same calibration procedure as this study, that is to calibrate with the same medium as the tissues to be measured. This is difficult for the case of the *in vivo* measurement. Therefore, we will estimate  $\text{SO}_2$  of microvessels after we calibrate with a phantom that has the same scattering coefficient as the target tissues. To obtain the scattering coefficient of the tissue or the phantom, we will perform the numerical-based method experiment such as the inverse Monte Carlo simulation and the Adding-Doubling technique [84]. This experiment is a widely used technique to obtain optical properties of tissues [10, 73, 74, 85–89]. In this experiment, the diffusion reflected and transmitted light is obtained by using an integrating sphere. After that, the numerical simulation is performed with changing an initial value of optical properties until the calculation results of both the diffusion reflectance and the transmittance match with the measured ones. Using the scattering coefficients estimated by the above method, we will calculate AECs as the scattering coefficients or wavelengths.

In this study, as the first approach, our correction method was proposed to use the average maximum slope of an intensity profile of a blood vessel with fixed depth as a feature value. To apply the correction method to actual tissues, we must determine the relationship between the scattering coefficients and depth of blood vessels. Furthermore, in that case, we have to investigate the relationship of the influence of between the tissue scattering and the blood vessel depth for reduction of contrast. Since the reason for use of the maximum slope in this study was that the maximum slope is corresponding to reduction in contrast of the image due to the tissue scattering, we investigate new feature values from SDF images for characterizing both depth and the scattering.

Furthermore, to improve the accuracy of  $\text{SO}_2$  estimation, we investigate optimal wavelengths of used LEDs. The previous study [42] suggested that the optimal wavelengths were 488, 635, and 905 nm for retinal oximetry. For SDF oximetry, the region of 450 ~ 600 nm of wavelength is required to obtain images of microcirculation. This is because that penetration depth is shorter than the longer wavelength, the scattering domain, and the difference of the absorption between blood and tissue.

To analyze spatial oxygen transportation accurately, we must improve  $\text{SO}_2$  estimation considering the above-mentioned issues though we showed the attempt of analysis of the oxygen

transportation in Chapter 6. Moreover, nonuniformity of reflected light on the tissue behind vessels may be correctable using the red-band images under illumination with a range of 624 nm wavelength, in which no blood vessels appear. Meanwhile, analysis of sequential oxygen transportation can be performed since SDF imaging allows obtaining images continuously as well as a typical camera with a 30 fps. To realize this analysis, we must perform rigid and non-rigid registration between frames due to the movement of subject's body or surgeon's hand. To perform real-time  $\text{SO}_2$  estimation with more than 30 fps, we consider the influence of our technique for obtaining band images. In this study, although band images were obtained by changing color of LEDs with  $\sim 100$  ms, we will apply a snap-shot spectral camera to obtain band images simultaneously in order to investigate the influence of color-changing for  $\text{SO}_2$  estimation.

# APPENDIX

## A Influence of other components of blood on SDF oximetry

Blood is composed of cells (RBCs, leukocytes, and platelets) and humoral (blood plasma) parts. The volume ratio of cells to humoral parts is about 45% to 55%. The volume ratio among cells is RBCs:leukocytes:platelets = 96% : 3% : 1%. The size of a RBC, leukocyte, and platelet is about  $7 \sim 8 \mu\text{m}$ ,  $6 \sim 30 \mu\text{m}$ , and  $2 \mu\text{m}$ , respectively. In normal blood vessels for SDF oximetry, the number of RBCs is dominant among the cell components and thus the influence (absorption or scattering) of both leukocytes and platelets is considered to be almost negligible. The absorption coefficient of platelets is small compared with one of hemoglobin [90].

There are several types of hemoglobin: methemoglobin, carboxyhemoglobin, and sulfhemoglobin. Normal human has methemoglobin in blood with  $1 \sim 2\%$ , which cannot bind with oxygen molecules and carry it. Carboxyhemoglobin and sulfhemoglobin is hemoglobin bind with a carbon monoxide (CO) and a sulfur atom, respectively. These are present in blood in the case of the carbon monoxide poisoning or sulfhemoglobinemia. The spectral absorption coefficient methemoglobin [91], carboxyhemoglobin [91], sulfhemoglobin [92]. Although the absorption coefficient of methemoglobin has the peak at 500 nm, the influence of one can be negligible because the amount of one included in blood is small. The absorption coefficient of carboxyhemoglobin is similar to one of de-oxygenated hemoglobin. The absorption coefficient of sulfhemoglobin has peaks near  $600 \mu$  and a nonnegligible value in the range of  $450 \sim 600 \text{ nm}$  compared with oxygenated and de-oxygenated hemoglobin. Thus, in the case that there is carboxyhemoglobin or sulfhemoglobin in blood,  $\text{SO}_2$  estimation method cannot be performed. The absorption coefficient of plasma is small compared with one of hemoglobin [90].

## **B Absorption coefficients of blood with $\text{SO}_2 = 0.0 \sim 1.0$**

Absorption coefficients of blood with  $\text{SO}_2$ ,  $s$ , used in the simulation is shown in Table B.1. These values of blood with  $s$  were calculated using both literature values of ones of blood with  $s = 0.0$  and  $s = 1.0$  with reference to previous studies [10, 73].

Table B.1: Optical properties of blood with SO<sub>2</sub> with reference to [10, 73]. The upper rows show the wavelength region of the blue illumination and the lower rows show one of the green illumination.

$\lambda$	$\mu_a$ [mm <sup>-1</sup> ]										
	SO <sub>2</sub>										
[nm]	1.0	0.9	0.8	0.7	0.6	0.5	0.4	0.3	0.2	0.1	0.0
420	257.2255291	253.327199	249.4288689	245.5305388	241.6322087	237.7338786	233.8355485	229.9372184	226.0388882	222.1405581	218.242228
430	131.7678416	146.8967896	162.0257375	177.1546854	192.2836334	207.4125813	222.5415292	237.6704772	252.7994251	267.928373	283.057321
440	54.93004159	71.5675576	88.20507361	104.8425896	121.4801056	138.1176216	154.7551376	171.3926537	188.0301697	204.6676857	221.3052017
450	33.63701981	35.80444852	37.97187722	40.13930592	42.30673463	44.47416333	46.64159203	48.80902073	50.97644944	53.14387814	55.31130684
460	23.81836859	22.68896667	21.55956474	20.43016282	19.3007609	18.17135897	17.04195705	15.91255512	14.7831532	13.65375128	12.52434935
470	17.78302532	16.86987362	15.95672192	15.04357022	14.13041852	13.21726682	12.30411512	11.39096342	10.47781172	9.564660024	8.651508325
480	14.25953464	13.61271171	12.96588879	12.31906586	11.67224293	11.02542001	10.37859708	9.731774153	9.084951227	8.4381283	7.791305373
490	12.68263869	12.30777784	11.93291699	11.55805613	11.18319528	10.80833443	10.43347357	10.05861272	9.683751867	9.308891014	8.934030161
500	11.20919843	11.20540719	11.20161596	11.19782473	11.19403349	11.19024226	11.18645103	11.18265979	11.17886856	11.17507733	11.1712861
510	10.72854718	11.03582983	11.34311249	11.65039515	11.95767781	12.26496047	12.57224312	12.87952578	13.18680844	13.4940911	13.80137376
520	12.96001987	13.35559328	13.75116669	14.1467401	14.54231351	14.93788692	15.33346033	15.72903374	16.12460715	16.52018056	16.91575397
477	15.44916791	14.69638323	13.94359855	13.19081387	12.43802919	11.68524451	10.93245983	10.17967515	9.426890468	8.674105788	7.921321108
487	13.21019842	12.7215149	12.23283137	11.74414785	11.25546432	10.7667808	10.27809727	9.789413749	9.300730224	8.812046699	8.323363175
497	11.70055938	11.55013096	11.39970254	11.24927412	11.0988457	10.94841728	10.79798886	10.64756044	10.49713202	10.3467036	10.19627518
507	10.68078192	10.88578696	11.090792	11.29579705	11.50080209	11.70580713	11.91081217	12.11581721	12.32082225	12.52582729	12.73083233
517	11.24603979	11.688436	12.13083221	12.57322842	13.01562463	13.45802084	13.90041704	14.34281325	14.78520946	15.22760567	15.67000188
527	18.33671671	18.46918497	18.60165322	18.73412148	18.86658973	18.99905799	19.13152625	19.2639945	19.39646276	19.52893101	19.66139927
567	26.64144501	26.31158631	25.98172761	25.65186891	25.3220102	24.9921515	24.6622928	24.3324341	24.0025754	23.6727167	23.34285799
547	26.70356126	26.77852915	26.85349703	26.92846492	27.00343281	27.07840069	27.15336858	27.22833647	27.30330435	27.37827224	27.45324013
557	18.46180598	19.53616006	20.61051414	21.68486821	22.75922229	23.83357636	24.90793044	25.98228451	27.05663859	28.13099266	29.20534674
567	19.54262872	20.20303154	20.86343437	21.52383719	22.18424001	22.84464284	23.50504566	24.16544849	24.82585131	25.48625413	26.14665696
577	29.74083164	28.91361456	28.08639748	27.2591804	26.43196332	25.60474623	24.77752915	23.95031207	23.12309499	22.29587791	21.46866083

# Reference

- [1] M. J. Leahy, “Microcirculation imaging,” Wiley-Blackwell, New Jersey, USA (2012).
- [2] J. D. Briers and S. Webster, “Quasi real-time digital version of single-exposure speckle photography for full-field monitoring of velocity or flow fields,” *Optics Communications*, Vol. 116, 1–3, 36–42 (1995).
- [3] S. Yuan, A. Devor, D. A. Boas, and A. K. Dunn, “Determination of optimal exposure time for imaging of blood flow changes with laser speckle contrast imaging,” *Applied Optics*, Vol. 44, 10, 1823–1830 (2005).
- [4] R. K. Wang, S. L. Jacques, Z. Ma, S. Hurst, S. R. Hanson, and A. Gruber, “Three dimensional optical angiography,” *Optics Express*, Vol. 15, 7, 4083–4097 (2007).
- [5] M. A. Yaseen, V. J. Srinivasan, I. Gorczynska, J. G. Fujimoto, D. A. Boas, and S. Sakadzic, “Multi-modal optical imaging system for in vivo investigation of cerebral oxygen delivery and energy metabolism,” *Biomedical Optics Express*, Vol. 6, 12, 4994–5007 (2015).
- [6] L. V. Wang and S. Hu, “Photoacoustic tomography: in vivo imaging from organelles to organs,” *Science*, Vol. 335, 6075, 1458–1462 (2012).
- [7] F. S. Foster, M. Y. Zhang, Y. Q. Zhou, G. Liu, J. Mehi, E. Cherin, K. A. Harasiewicz, B. G. Starkoski, L. Zan, D. A. Knapik, and S. L. Adamson, “A new ultrasound instrument for in vivo microimaging of mice,” *Ultrasound in Medicine & Biology*, Vol. 28, 9, 1165–1172 (2002).
- [8] S. M. Jorgensen, O. Demirkaya, and E. L. Ritman, “Three-dimensional imaging of vasculature and parenchyma in intact rodent organs with X-ray micro-CT,” *American Journal of Physiology Heart and Circulatory Physiology*, Vol. 275, 3, H1103–H1114 (1998).
- [9] W. Groner, J. W. Winkelman, A. G. Harris, C. Ince, G. J. Bouma, K. Messmer, and R. G. Nadeau, “Orthogonal polarization spectral imaging: A new method for study of the microcirculation,” *Nature Medicine*, Vol. 5, 10, 1209–1213 (1999).
- [10] S. Prahl, “Optical absorption of hemoglobin,”  
<http://omlc.ogi.edu/spectra/hemoglobin/index.html> (accessed on November 14, 2014).
- [11] Cytoscan video microscope, Cytometrics,  
<http://www.cytometrics.com/home.htm> (accessed on October 7, 2016).
- [12] C. Ince, “Sidestream dark field imaging: an improved technique to observe sublingual microcirculation,” *Critical Care*, 9 Suppl 1, P72 (2005).
- [13] C. Ince, “The microcirculation is the motor of sepsis,” *Critical Care*, 9 Suppl 4, S13–S19 (2005).



- [14] P. T. Goedhart, M. Khalilzadeh, R. Bezemer, J. Merza and C. Ince, "Sidestream dark field (SDF) imaging: a novel stroboscopic LED ring-based imaging modality for clinical assessment of the microcirculation," *Optics Express*, Vol. 15, 23, 15101–15114 (2007).
- [15] R. Bezemer, P. Goedhart, M. Khalilzadeh, and C. Ince, "Sidestream dark-field imaging versus orthogonal polarization spectroscopic imaging: a comparative study," *Critical Care*, 12 Suppl 2, P63 (2008).
- [16] Microscan, MicroVision Medical,  
<http://www.microvisionmedical.com/> (accessed on October 7, 2016).
- [17] M. Trompeter, T. Brazda, C. T. Remy, T. Vestring, and P. Reimer, "Non-occlusive mesenteric ischemia: etiology, diagnosis, and interventional therapy," *European Radiology*, Vol. 12, 1179–1187 (2002).
- [18] A. Rieber, D. Wruk, S. Potthast, K. Nüssle, M. Reinshagen, G. Adler, and H.-J. Brambs, "Diagnostic imaging in Crohn's disease: comparison of magnetic resonance imaging and conventional imaging methods," *International Journal of Colorectal Disease*, Vol. 15, 176–181 (2000).
- [19] D. De Backer, J. Creteur, J. C. Preiser, M. J. Dubois, and J. L. Vincent, "Microvascular blood flow is altered in patients with sepsis," *American Journal of Respiratory and Critical Care Medicine*, Vol. 166, 98–104 (2002).
- [20] P. E. Spronk, C. Ince, M. J. Gardien, K. R. Mathura, H. M. Oudemans-van Straaten, and D. F. Zandstra, "Nitroglycerin in septic shock after intravascular volume resuscitation," *Lancet*, 360, 1395–1396 (2002).
- [21] Y. Sakr, M.-J. Dubois, D. De Backer, J. Creteur, J.-L. Vincent, "Persistent microcirculatory alterations are associated with organ failure and death in patients with septic shock," *Critical Care*, Vol. 32, 1825–1831 (2004).
- [22] A. Draisma, R. Bemelmans, J. G. van der Hoeven, P. Spronk, P. Pickkers, "Microcirculation and vascular reactivity during endotoxemia and endotoxin tolerance in humans," *Shock*, Vol. 31, 6, 582–586 (2009).
- [23] A. Spanos, S. Jhanji, A. Vivian-Smith, T. Harris, R. M. Pearse, "Early microvascular changes in sepsis and severe sepsis," *Shock*, Vol. 33, 4, 387–391 (2010).
- [24] D. De Backer, S. Hollenberg, C. Boerma, P. Goedhart, G. Buchele, G. Ospina-Tascon, I. Dobbe, and C. Ince, "How to evaluate the microcirculation: report of a round table conference," *Critical Care*, Vol. 11, 5, R101 (2007).
- [25] J. G. Dobbe, G. J. Streekstra, B. Atasever, R. Van Zijderveld, and C. Ince, "Measurement of functional microcirculatory geometry and velocity distributions using automated image analysis," *Medical & Biological Engineering & Computing*, Vol. 46, 659–670 (2008).
- [26] H. Akbari, Y. Kosugi, K. Kojima, and N. Tanaka, "Detection and analysis of the intestinal ischemia using visible and invisible hyperspectral imaging," *IEEE Transactions on Biomedical Engineering*, Vol. 57, 2011–2017 (2010).
- [27] D. Goldman, "Theoretical models of microvascular oxygen transport to tissue," *Microcirculation*, Vol. 15, 8, 795–811 (2008).
- [28] R. N. Pittman, "Oxygen transport in the microcirculation and its regulation," *Microcirculation*, Vol. 20, 2, 117–137 (2013).

- [29] D. M. J. Milstein, J. A. H. Lindeboom, and C. Ince, "Intravital sidestream dark-field (SDF) imaging is used in a rabbit model for continuous noninvasive monitoring and quantification of mucosal capillary regeneration during wound healing in the oral cavity: A pilot study," *Archives of Oral Biology*, 55, 343–349 (2010).
- [30] J. A. Lee, R. T. Kozikowski, and B. S. Sorg, "In vivo microscopy of microvessel oxygenation and network connections," *Microvascular Research*, 98, 29–39 (2015).
- [31] E. Damiani, E. Pierpaoli, F. Orlando, A. Donati, and M. Provinciali, "Sidestream dark field videomicroscopy for in vivo evaluation of vascularization and perfusion of mammary tumours in HER2/neu transgenic mice," *Clinical and Experimental Pharmacology and Physiology*, 42, 225–229 (2015).
- [32] R. N. Pittman and B. R. Duling, "Measurement of percent oxyhemoglobin in the microvasculature," *Journal of Applied Physiology*, Vol. 38, 321–327 (1975).
- [33] B. Styp-Rekowska, N. Disassa, B. Reglin, L. Ulm, H. Kuppe, T. Secomb, and A. Pries, "An imaging spectroscopy approach for measurement of oxygen saturation and hematocrit during intravital microscopy," *Microcirculation*, Vol. 14, 3, 207–221 (2007).
- [34] J. B. Hickam, R. Frayser, and J. C. Ross, "A study of retinal venous blood oxygen saturation in human subjects by photographic means," *Circulation*, Vol. 27, 3, 375–385 (1963).
- [35] A. J. Cohen and R. A. Laing, "Multiple scattering analysis of retinal blood oximetry," *IEEE Transactions on Biomedical Engineering*, Vol. 23, 5, 391–400 (1976).
- [36] V. Twersky "Multiple scattering of electromagnetic waves by arbitrary configurations," *Journal of Mathematical Physics*, Vol. 8, 589 (1967).
- [37] V. Twersky, "Interface effects in multiple scattering by large, low-refracting, absorbing particles," *Journal of the Optical Society of America*, Vol. 60, 7, 908–914 (1970).
- [38] V. Twersky, "Absorption and multiple scattering by biological suspensions," *Journal of the Optical Society of America*, Vol. 60, 1084–1093 (1970).
- [39] F. C. Delori "Noninvasive technique for oximetry of blood in retinal vessels," *Applied Optics*, Vol. 27, 1113–1125 (1988).
- [40] J. M. Beach, K. J. Schwenzer, S. Srinivas, D. Kim, and J. S. Tiedeman "Oximetry of retinal vessels by dual-wavelength imaging: calibration and influence of pigmentation," *Journal of Applied Physiology*, Vol. 86, 2, 748–758 (1999).
- [41] S. H. Hardarson, A. Harris, R. A. Karlsson, G. H. Halldorsson, L. Kagemann, E. Rechtman, G. M. Zoega, T. Eysteinnsson, J. A. Benediktsson, A. Thorsteinsson, P. K. Jensen, J. Beach, and E. Stefansson "Automatic Retinal Oximetry," *Investigative ophthalmology & visual science*, Vol. 47, 11, 5011–5016 (2006).
- [42] M. H. Smith, "Optimum wavelength combinations for retinal vessel oximetry," *Applied Optics*, Vol. 38, 1, 258–267 (1999).
- [43] H. F. Zhang, K. Maslov, G. Stoica, and L. V. Wang, "Functional photoacoustic microscopy for high-resolution and noninvasive in vivo imaging ," *Nature Biotechnology*, 24, 848–851 (2006).

- [44] J. Yao, K. I. Maslov, Y. Zhang, Y. Xia, and L. V. Wang, "Label-free oxygen-metabolic photoacoustic microscopy in vivo," *Journal of Biomedical Optics*, 16(7), 076003 (2011).
- [45] L-D. Liao, C-T. Lin, Y-Y. I. Shih, T. Q. Duong, H-Y. Lai, P-H. Wang, R. Wu, S. Tsang, J-Y. Chang, M-L. Li, Y-Y. Chen, "Transcranial imaging of functional cerebral hemodynamic changes in single blood vessels using in vivo photoacoustic microscopy," *Journal of Cerebral Blood Flow & Metabolism*, 32(6), 938–951 (2012).
- [46] S. P. Chong, C. W. Merkle, C. Leahy, H. Radhakrishnan, and V. J. Srinivasan, "Quantitative microvascular hemoglobin mapping using visible light spectroscopic optical coherence tomography," *Biomedical Optics Express*, Vol. 6, 4, 1429–1450 (2015).
- [47] T. Kurata, Z. Li, S. Oda, H. Kawahira, and H. Haneishi, "Impact of vessel diameter and bandwidth of illumination in sidestream dark-field oximetry," *Biomedical Optics Express*, Vol. 6, 5, 1616–1631 (2015).
- [48] S. Sakadžić, E. Roussakis, M. A. Yaseen, E. T. Mandeville, V. J. Srinivasan, K. Arai, S. Ruvinskaya, A. Devor, E. H. Lo, S. A. Vinogradov, and D. A. Boas "Two-photon high-resolution measurement of partial pressure of oxygen in cerebral vasculature and tissue," *Nature Methods*, Vol. 7, 9, 755–759 (2010).
- [49] S. Hu, K. Maslov, V. Tsytarev, and L. V. Wang, "Functional transcranial brain imaging by optical-resolution photoacoustic microscopy," *Journal of Biomedical Optics*, 14(4), 040503 (2009).
- [50] F. E. Robles, S. Chowdhury, and A. Wax, "Assessing hemoglobin concentration using spectroscopic optical coherence tomography for feasibility of tissue diagnostics," *Biomedical Optics Express*, Vol. 1, 1, 310–317 (2010).
- [51] S. Chen, Q. Liu, X. Shu, B. Soetikno, S. Tong, and H. F. Zhang, "Imaging hemodynamic response after ischemic stroke in mouse cortex using visible-light optical coherence tomography," *Biomedical Optics Express*, Vol. 7, 9, 3377–3390 (2016).
- [52] T. Kurata, S. Oda, H. Kawahira, and H. Haneishi, "Correction method for influence of tissue scattering for sidestream dark-field oximetry using multicolor LEDs" *Optical Review*, (2016) (in press)
- [53] Z. Li, S. Kaneko, S. Oda, H. Kawahira, and H. Haneishi, "Microcirculation imaging with multicolor LEDs and mini CCD camera," *World Congress on Medical Physics and Biomedical Engineering*, Beijing, China, Vol. 39, 1006–1009 (2012).
- [54] 金子, "微小循環の定量的画像解析のための基礎研究," 千葉大学大学院工学研究科修士論文 (Non-publication), (2013).
- [55] G. H. Weiss, R. Nossal, and R. F. Bonner, "Statistics of penetration depth of photons re-emitted from irradiated tissue," *Journal of Modern Optics*, Vol. 36, 3, 349–359 (1989).
- [56] R. V. Maikala, "Modified Beer's Law – historical perspectives and relevance in near-infrared monitoring of optical properties of human tissue," *International Journal of Industrial Ergonomics*, Vol. 40, 125–134 (2010).
- [57] M. Hammer, S. Leistritz, L. Leistritz, and D. Schweitzer, "Light paths in retinal vessel oximetry," *IEEE Transactions on Biomedical Engineering*, Vol. 48, 592–598 (2001).
- [58] A. R. Pries, G. Kanzow, and P. Gaehtgens, "Microphotometric determination of hematocrit in small vessels," *American Journal of Physiology*, Vol. 245, 167–177 (1983).

- [59] J. Lowell, A. Hunter, D. Steel, A. Basu, R. Ryder, and R. L. Kennedy, "Measurement of retinal vessel widths from fundus images based on 2-D modeling," *IEEE Transactions on Medical Imaging*, Vol. 23, 1196–1204 (2004).
- [60] L. Pedersen, M. Grunkin, B. Ersbøll, K. Madsen, M. Larsen, N. Christoffersen, and U. Skands, "Quantitative measurement of changes in retinal vessel diameter in ocular fundus images," *Pattern Recognition Letters*, Vol. 21, 1215–1223 (2000).
- [61] iDule Corporation, Data sheet of ID04MB-IP-U,  
[http://www.idule.jp/product/product\\_iPork.html](http://www.idule.jp/product/product_iPork.html) (accessed on October 7, 2016).
- [62] V. V. Tuchin, "Tissue optics: light scattering methods and instruments for medical diagnosis," SPIE press Bellingham, Washington, USA (2007).
- [63] L. Wang, S. L. Jacques, and L. Zheng, "MCML – Monte Carlo modeling of light transport in multi-layered tissues," *Computer Methods and Programs in Biomedicine*, Vol. 47, 131–146 (1995).
- [64] D. Boas, J. Culver, J. Stott, and A. Dunn, "Three dimensional Monte Carlo code for photon migration through complex heterogeneous media including the adult human head," *Optics Express*, Vol. 10, 159–170 (2002).
- [65] Q. Fang and D. A. Boas, "Monte Carlo simulation of photon migration in 3D turbid media accelerated by graphics processing units," *Optics Express*, Vol. 17, 20178–20190 (2009).
- [66] Q. Fang, "Mesh-based Monte Carlo method using fast ray-tracing in Plücker coordinates," *Biomedical Optics Express*, Vol. 1, 165–75 (2010).
- [67] Q. Fang, "Mesh-based Monte Carlo (MMC)," <http://mcx.sourceforge.net/cgi-bin/index.cgi?MMC> (accessed on December 10, 2012).
- [68] I. G. Henyey and J. L. Greenstein, "Diffuse radiation in the galaxy," *The Astrophysical Journal*, Vol. 93, 70–93 (1941).
- [69] ROHM Co., Ltd., Data sheet of SMLVN6RGB1 series,  
<http://www.rohm.co.jp/web/japan/datasheet/SMLVN6RGB1W> (accessed on October 7, 2016).
- [70] L. Reynolds, C. Johnson, and A. Ishimaru, "Diffuse reflectance from a finite blood medium: applications to the modeling of fiber optic catheters.," *Applied Optics*, Vol. 15, 9, 2059–2067 (1976).
- [71] Q. Fang and D. A. Boas, "Tetrahedral mesh generation from volumetric binary and grayscale images," in *Biomedical Imaging: From Nano to Macro, 2009. ISBI'09. IEEE International Symposium on Biomedical Imaging 2009*, (IEEE, 2009), pp. 1142–1145.
- [72] Q. Fang, iso2mesh,  
<http://iso2mesh.sourceforge.net/cgi-bin/index.cgi?Home> (accessed on December 11, 2012).
- [73] M. Friebel, K. Do, A. Hahn, G. Mu, D. Berlin, L. Medizin, and F. Universita, "Optical properties of circulating human blood in the wavelength range 400 - 2500 nm," *Journal of Biomedical Optics*, 4(1), 36–46 (1999).

- [74] N. Bashkatov, E. Genina, V. I. Kochubey, and V. V. Tuchin, "Optical properties of human skin, subcutaneous and mucous tissues in the wavelength range from 400 to 2000 nm," *Journal of Physics D: Applied Physics*, Vol. 38, 2543–2555 (2005).
- [75] D. Hidović-Rowe and E. Claridge, "Modelling and validation of spectral reflectance for the colon," *Physics in Medicine and Biology*, Vol. 50, 1071–1093 (2005).
- [76] H. J. Van Staveren, C. J. Moes, J. van Marie, S. A. Prahl, and M. J. Van Gemert, "Light scattering in Intralipid- 10% in the wavelength range of 400-1100 nm," *Applied Optics*, Vol. 30, 4507–4514 (1991).
- [77] M. H. Smith, K. R. Denninghoff, A. Lompado, and L. W. Hillman, "Effect of multiple light paths on retinal vessel oximetry," *Applied Optics*, Vol. 39, 7, 1183–1193 (2000).
- [78] I. Nishidate, T. Maeda, Y. Aizu, and K. Niizeki, "Visualizing depth and thickness of a local blood region in skin tissue using diffuse reflectance images," *Journal of Biomedical Optics*, 12(5), 054006 (2007).
- [79] A. F. Frangi, W. J. Niessen, K. L. Vincken, and M. V. Viergever, "Multiscale vessel enhancement filtering," *International Conference on Medical Image Computing and Computer-Assisted intervention*, Vol. 1496, 130–137 (1998).
- [80] B. Barber, Qhull (2015. 2 for Windows 10, 8, 7, XP, and NT), <http://www.qhull.org/> (accessed on June 30, 2016).
- [81] A. L. Vazquez, M. Fukuda, M. L. Tasker, K. Masamoto and S-G Kim, "Changes in cerebral arterial, tissue and venous oxygenation with evoked neural stimulation: implications for hemoglobin-based functional neuroimaging," *Journal of cerebral blood flow and metabolism*, 30, 2, 428–439 (2010).
- [82] H. C. Hendargo, Y. Zhao, T. Allenby, and G. M. Palmer, "Snap-shot multispectral imaging of vascular dynamics in a mouse window chamber model," *Optical Letter*, Vol. 40, 14, 3292–3295 (2015).
- [83] A. Krogh, "The number and distribution of capillaries in muscles with calculations of the oxygen pressure head necessary for supplying the tissue," *Journal of Physiology*, Vol. 52, 6, 409–415 (1919).
- [84] S. A. Prahl, "The adding-doubling method," *Optical-thermal response of laser-irradiated tissue* (Edited by A. J. Welch and M. J. C. van Gemert), 101–129, Plenum Press, New York (1995).
- [85] R. Graaff, A. C. M. Dassel, M. H. Koelink, F. F. M. de Mul, J. G. Aarnoudse, and W. G. Zijlstra, "Optical properties of human dermis in vitro and in vivo," *Appli. Opt.*, Vol. 32, 4, 435–447 (1993).
- [86] S. A. Prahl, M. J. C. van Gemert, and A. J. Welch, "Determining the optical properties of turbid media by using the Adding Doubling method," *Applied Optics*, Vol. 32, 4, 559–568 (1993).
- [87] A. N. Bashkatov, E. A. Genina, V. I. Kochubey, V. V. Tuchin, E. E. Chikina, A. B. Knyazev, and O. V. Mareev, "Optical Properties of mucous membrane in the spectral range 350-2000 nm," *Optics and Spectroscopy*, Vol. 97, No. 6, 978–983 (2004).
- [88] A. N. Bashkatov, E. A. Genina, V. I. Kochubey, A. A. Gavrilova, S. V. Kapralov, V. A. Grishaev, V. V. Tuchin, "Optical properties of human stomach mucosa in the spectral range from 400 to 2000nm: Prognosis for gastroenterology," *Medical Laser Application*, 22, 95–104 (2007).
- [89] A. N. Bashkatov, E. A. Genina, V. I. Kochubey, and V. V. Tuchin, "Optical properties of human sclera in spectral range 370–2500 nm," *Optics and Spectroscopy*, Vol. 109, 2, 197–204 (2010).

- [90] M. Meinke, G. Müller, J. Helfmann, and M. Friebe, “Optical properties of platelets and blood plasma and their influence on the optical behavior of whole blood in the visible to near infrared wavelength range,” *Journal of Biomedical Optics*, 12(1), 014024 (2007).
- [91] A. Zwart, A. Buurma, E. J. van Kampen, B. Oeseburg, P. H. W. van der Ploeg, and W. G. Zijlstra “A Multi-Wavelength spectrophotometric method for the simultaneous determination of five haemoglobin derivatives,” *Journal of clinical chemistry and clinical biochemistry*, Vol. 19, 457–463 (1981).
- [92] W. G. Zijlstra and A. Buursma, “Spectrophotometry of hemoglobin: absorption spectra of bovine oxy-hemoglobin, deoxyhemoglobin, carboxyhemoglobin, and methemoglobin,” *Comparative Biochemistry and Physiology Part B*, Vol. 118, 4, 743–749 (1997).

# Acknowledgements

本論文は筆者が千葉大学大学院人工システム科学専攻メディカルシステムコース博士後期課程に在籍中の研究成果をまとめたものである。

本研究を行うにあたり終始ご指導戴いた、同大学フロンティア医工学センター教授 羽石 秀昭 先生には深謝の意を表す。また、本論文の学位論文審査を担当して戴いた同大学フロンティア医工学センター 教授 山口 匡 先生，同大学大学院人工システム科学専攻機械系コース 教授 坪田 健一 先生，同大学フロンティア医工学センター 教授 中口 俊哉 先生に感謝の意を表す。

医学的見地から貴重なご意見を戴いた同大学大学院医学研究院救急集中治療医学 教授 織田 成人 先生，同大学フロンティア医工学センター 准教授 川平 洋 先生 に感謝の意を表す。

研究を遂行するにあたり，SDF プローブの作製をして戴いた株式会社マイクロテック・ニチオンの営業部 大西 信弘 氏，技術部 松本 敦士 氏，照明コントロールユニットを作製して戴いたタカノ株式会社事業化室 春日 久男 氏，ファントムの容器を作製して戴いた同部署 伊藤 恒太郎 氏に感謝を申し上げる。

本研究の共同研究者である 李 震光 氏，動物実験を遂行するにあたり助言して戴いた羽石研究室の 高橋 穂 氏に感謝を申し上げる。

千葉大学での研究の機会を与えて戴いたタカノ株式会社 相談役 堀井 朝運 氏，同社 代表取締役 鷹野 準 氏，同社 常務取締役 大原 明夫 氏に感謝の意を表す。また，同社事業化室の皆様にも日頃より励ましや助言を戴き，感謝を申し上げる。

研究遂行にあたり日頃より有益な討論，助言を戴いた同大学フロンティア医工学センター 助教 大西 峻 先生および羽石研究室の皆様に感謝を申し上げる。

最後に，陰ながら支えてくれた 妻 亜紀 に心から感謝の意を表す。

2017年1月 倉田 智宏

# Publication list

## Published papers

T. Kurata, Z. Li, S. Oda, H. Kawahira, and H. Haneishi: “Impact of vessel diameter and bandwidth of illumination in sidestream dark-field oximetry,” Biomedical Optics Express, Vol. 6, No. 5, 1616-1631, April 6, 2015. DOI:10.1364/BOE.6.001616

T. Kurata, S. Oda, H. Kawahira, and H. Hanesihi: “Correction method for influence of tissue scattering for sidestream dark-field oximetry using multicolor LEDs,” Optical Review, Vol. 23, No. 6, 955-967, October 7, 2016. DOI: 10.1007/s10043-016-0278-7

## Conference papers

倉田智宏, 李 震光, 川平 洋, 羽石秀昭: “狭帯域照明を用いた SDF 撮影法による毛細血管の血中酸素飽和度の推定”, 日本光学会年次学術講演会 (Optics & Photonics Japan 2014), 7pA6, 東京 (2014 年 11 月 5–7 日)

李震光, 倉田智宏, 織田成人, 川平洋, 大西峻, 羽石秀昭: “SDF 撮影装置を用いた微小循環酸素飽和度の推定”, 日本医工学治療学会 第 31 回学術大会, R6-3, 広島 (2015 年 3 月 27–29 日)

T. Kurata, Z. Li, S. Oda, H. Kawahira, T. Ohnishi, and H. Haneishi: “Sidestream dark-field oximetry with multicolor LEDs,” IUPESM 2015 World Congress On Medical Physics and Biomedical Engineering, SP139.4, Toronto, Canada (June 7–12, 2015)



T. Kurata, S. Oda, H. Kawahara, T. Ohnishi, and H. Haneishi: “Microcirculation oximetry using sidestream dark-field imaging,” International Symposium on InfoComm and Media Technology in Bio-Medical and Healthcare Application (2015 IS-3T-in-3A), P32, Chiba, Japan (November 15–18, 2015)

T. Kurata, M. Takahashi, T. Ohnishi, and H. Haneishi: “Visualization of oxygen transportation in microcirculation by sidestream dark-field oximetry”, SPIE Photonics West BIOS, 10068-37, San Francisco, California, USA (January 28 – February 2, 2017)